INFORMATION TO USERS

This manuscript has been reproduced from the microfilm master. UMI films the text directly from the original or copy submitted. Thus, some thesis and dissertation copies are in typewriter face, while others may be from any type of computer printer.

The quality of this reproduction is dependent upon the quality of the copy submitted. Broken or indistinct print, colored or poor quality illustrations and photographs, print bleedthrough, substandard margins, and improper alignment can adversely affect reproduction.

In the unlikely event that the author did not send UMI a complete manuscript and there are missing pages, these will be noted. Also, if unauthorized copyright material had to be removed, a note will indicate the deletion.

Oversize materials (e.g., maps, drawings, charts) are reproduced by sectioning the original, beginning at the upper left-hand corner and continuing from left to right in equal sections with small overlaps. Each original is also photographed in one exposure and is included in reduced form at the back of the book.

Photographs included in the original manuscript have been reproduced xerographically in this copy. Higher quality 6" x 9" black and white photographic prints are available for any photographs or illustrations appearing in this copy for an additional charge. Contact UMI directly to order.

UMI

A Bell & Howell Information Company
300 North Zeeb Road. Ann Arbor. MI 48106-1346 USA
313/761-4700 800/521-0600

A

FILM SYNTHESIS AND MAGNETIC PROPERTIES OF IRON RICH $ThMn_{12}$ TYPE PSEUDOBINARY $RFe_{12-x}T_x$ COMPOUNDS AND THEIR NITRIDES.(T=TRANSITION METAL AND R=RARE EARTH)

by

U. A. NAVARATHNA

A dissertation submitted to the Graduate Faculty in Physics in partial fulfillment of the requirements for the degree of Doctor of Philosophy, The City University of New York.

1995

This Manuscript has been read and accepted for the Graduate Faculty in Physics in satisfaction of the dissertation requirement for the degree of Doctor of Philosophy.

4/24/95
Date

Fred J. Cadieu
Chair of Examining Committee

4/24/95
Date

Joseph B. Krieger
Executive Officer

Prof. Fred J. Cadieu

Prof. R. Fischer

Prof. M. Tomkiewicz

Dr. Herb Leupold

Dr. Suri Hegde

Supervisory Committee

THE CITY UNIVERSITY OF NEW YORK

ABSTRACT

FILM SYNTHESIS AND MAGNETIC PROPERTIES OF IRON RICH $ThMn_{12}$ TYPE PSEUDOBINARY $RFe_{12-x}T_x$ COMPOUNDS AND THEIR NITRIDES.

by

U.A. Navarathna

Adviser: Professor F.J. Cadieu

For the first time, $ThMn_{12}$ type pseudobinary $R(Fe,T)_{12}$ compounds, where R=Sm or Nd and T= Ti, V or Mo, have been sputter synthesized in film form with record high energy product values. Films were synthesized in highly (002) texture mode on polycrystalline Al_2O_3 substrates, where the easy c-axis is highly aligned normal to the film plane, by control of sputtering parameters. Perpendicular to the film plane energy product for a highly (002) textured $Sm(Fe,Ti,V)_{12}$ sample was 21 MGOe at room temperature. For a nitrided highly (002) textured $Nd(Fe,Mo)_{12}N_x$ sample, the room temperature coercivity, saturation magnetization, and energy product values were 7.2 kOe, 12.8 kG and 30.2 MGOe respectively, in a direction perpendicular to the film plane. The room temperature anisotropy field value was estimated to be 130 kOe for the same film. In $Nd(Fe,Mo)_{12}N_x$ samples some of the Mo were replaced with Co to enhance the flux density. The room temperature, perpendicular to the film plane energy product was 46.3 MGOe for a sample containing 50% of the Mo replaced with Co. This is the highest room temperature energy product value reported for a nitrided 1-12 sample. Normal to the film plane saturation magnetization and coercivity values were 15.5 kG and 8.7 kOe respectively, for the Co substituted sample. At 10 K, saturation magnetization, coercivity, and energy product increased to 17 kG, 24 kOe and 59.6 MGOe respectively. All these high energy product films were very dense and SEM photographs of fractured sample edges indicated no discernible columnar or void structures. Films were free of α-Fe as revealed by the x-ray diffraction patterns. High energy product thin film magnets are useful in many applications, such as small scale electromechanical devices, microwave devices, integrated circuits and small scale permanent magnet geometries.

ACKNOWLEDGMENTS

I am especially grateful to my supervisor, Professor Fred J. Cadieu, for his continuous support and encouragement throughout this work. Without his generous support and assistance this thesis work would have been impossible. Also special thanks are due to Research Associate Dr. Hari Hegde. I also thank my colleagues at the laboratory Ms. Raj Rani, Mr. P. Samarasekara and Dr. Qian. Thanks are due to former colleagues Dr. K. Chen and Dr. N. Kamprath.

I would like to thank Professor C.R. Fischer, Professor M. Tomkiewicz, Dr. H.A. Leupold, Dr. Suri Hegde, and Dr. M.A. Russak for having served in my thesis Supervisory Committee.

It is my pleasure to thank son Kasun, daughter Malithi and wife Marie for her patience and support during this project.

I take this opportunity to express my appreciation to all members of the faculty and staff, colleagues and friends at the Department of Physics, Queens College. In particular I thank Dr. D. Sunil, a former colleague at the Department of Physics.

My thesis is part of the research program, studying the magnetic properties of rare earth transition metal permanent magnet system supported by grants to Professor Cadieu from the Department of Energy.

TABLE OF CONTENTS

List of Tables

List of Figures

CHAPTER 1 INTRODUCTION

Thin film magnets are useful in many applications, such as small scale electromechanical devices, microwave devices, small scale integrated circuits and small scale permanent magnet geometries(1)(2)(3). These are in addition to the well known application of thin film magnets in storage media. All of these applications are possible only when these magnetic films can be made in anisotropic form, with the easy magnetization direction aligned either parallel or perpendicular to the film plane. In addition to the small scale device applications, fabrication of highly anisotropic film magnets are useful to investigate their intrinsic magnetic properties, which may not be possible by use of isotropic film magnets where the availability of high fields are limited. Determination of the intrinsic magnetic properties is the first step to explore the magnetic material as a novel candidate for permanent magnet applications compared with the presently available permanent magnet materials.

Early on Cadieu et al. had shown that good intrinsic magnetic properties could be achieved in Sm-Fe-Ti samples(4). This discovery that Fe-rich rare earth intermetallic compounds posses good permanent magnetic properties has led the intense investigation of these intermetallic compounds by many researchers and later on several phases were identified including the $ThMn_{12}$ type tetragonal structure in Sm-Fe-Ti compounds(29).

Intermetallic compounds with $ThMn_{12}$ type structure can be formed when iron and rare earth elements are combined with a small amount of a non magnetic transition element such as Ti, V,Mo, Si, Cr or W. It is a well known fact that in R-T intermetallic compounds, R=rare earth and T=transition metal, when both R elements and M elements are magnetic, the effective coupling between R and M elements is ferromagnetic for light rare earth elements and ferrimagnetic for heavy rare earth elements. The composition of the iron rich rare earth intermetallic compounds, that crystallize in the tetragonal $ThMn_{12}$ type crystal structure, is $RFe_{12-x}T_x$, R=rare earth and T=Ti, V, Mo, Si, Cr or W, where the observed range of x for solid solutions is $1 \leq x \leq 2$(5) and there are exceptions too. The lowest value of x observed for bulk samples is x=0.8 in the case of $SmFe_{11.2}Ti_{0.8}$(6).

We have been able to synthesize these Fe rich $ThMn_{12}$ type rare earth intermetallic compounds, $R(Fe,T)_{12}$ where R=Sm or Nd and T=Ti, V or Mo, in film form by directly crystallizing the compound on polycrystalline Al_2O_3 substrates using RF sputtering(7). All the films synthesized by direct crystallization show a high degree of crystallographic texture with the c-axis of the individual crystallites highly aligned perpendicular to the film plane. Highly (002) textured films are very useful in determining the intrinsic magnetic properties such as saturation moment and magnetocrystalline anisotropy field since the c-axis is the easy axis for most of the members in R-Fe-T family. In the $SmFe_{12-x}Ti_x$ compounds films have been synthesized, which are free of α-Fe, for the x values as low as 0.1 and with a high degree of different crystallographic texture modes(8). Stabilizing of the 1-12 phase for low non-magnetic third element concentrations without the precipitation of α-Fe increases the saturation moment and it also contradicts the wide belief that large amount of non magnetic third element, x>1, is needed to stabilize the 1-12 phase. Binary $SmFe_{12}$ compounds, without the substitution of any non magnetic transition metal elements, have also been synthesized for the first time in Prof Cadieu's laboratory(7).

A magnetic material, to be qualified as a high performance permanent magnet, should have a high saturation moment (M_s), a large uniaxial anisotropy field (H_A), a remanent moment value (M_r) close to Ms, a large intrinsic coercivity value ($_iH_c$) showing the ability to stay in the metastable state of saturated magnetization in a reverse field and a high Curie temperature (T_c). The requirements of M_s, H_A and $_iH_c$ should be valid for a wide temperature range specially the room temperature and above.

It has been possible to achieve remnant flux density values very close to saturation values in perpendicular to the film plane direction for the extremely (002) textured films. Together with a high intrinsic coercivity these highly (002) textured film magnets can produce high static energy product magnets. Perpendicular to the film plane static energy product of 21 MGOe has been measured, at 293 K, for a $ThMn_{12}$ type $Sm_{8.04}Fe_{79.16}Ti_{9.11}V_{3.69}$ film sample(7). The anisotropy field H_A has been estimated to be 130 kOe, at 293 K, by extrapolating the perpendicular to the film plane (easy direction) and in the film plane (hard direction) hysteresis loops. It should be noted that the two loops measured in the film plane and perpendicular to the film plane directions intersect at a field value approximately equal to the anisotropy field H_A

since in these extremely (002) textured films the c-axis, easy axis, of the individual crystallites is highly aligned perpendicular to the film plane.

Although high coercivity values have been reported for isotropic bulk samples in Sm-Fe-T family, so far, there are no reports of prefered crystallographic orientation in bulk samples which is necessary to achieve high remenant values M_r.

In contrast to the bulk samples films have been made with different crystallographic texture modes by RF sputtering . Since the substrate material, on which the films grow with different crystallographic orientation, is pollycrystalline Al_2O_3, matching of the d-spacing of the substrate material and the film compound that could be responsible for the different growth modes, or the epitaxial growth of the film, can be ruled out. The sputtering parameters, such as sputtering gas pressure, bias voltage which is related to input RF power and substrate temperature during the film deposition, can be varied to change the texture mode from highly (002) textured to highly (222) textured where the c-axis makes an angle of 39° with perpendicular to the film plane direction(8). The degree of texturing is a function of controlling the film growth dynamics so that crystallites with a specific crystallite orientation grow preferentially and become the sole growth mode. As the film grows from randomly oriented discrete initial nuclei, growth rate is very high in certain crystallographic directions and will eventually dominate. The directions in which the growth rate is very high depends on the adatom surface mobility which in turn depends on the substrate temperature, sputtering gas pressure, and deposition rate.

Magneto-optical properties of the $ThMn_{12}$ type $Sm(Fe,Ti)_{12}$ films have also been studied to explore these compounds further(9). The $ThMn_{12}$ type $Sm(Fe,Ti)_{12}$ films that has been used in this study are either highly (002) textured, where the c-axes of the crystallites are normal to the film plane, or highly (222) textured, where the c-axes of the crystallites makes a well defined angle away from the film normal, 39°.

The polar Kerr rotation (Θ_K) and optical coercivities were studied for the photon energy range 1-2.5 ev. These measurements sample only the top few hundreds of angstroms of the film since the penetrating depth of light is a few hundreds of angstroms. By comparing the crystalline, magnetic and magneto-optical properties of these differently textured, (002) and (222) textured, films one can draw important conclusions that could not be possible otherwise, such as the surface deterioration of the film over time, change in grain size with thickness and the dependence of rate of change in grain size with thickness on texture mode. The polar Kerr rotation of these highly textured films, which contain more than 85% of Fe, exhibited similar behavior as pure Fe films for the 1-2.5 ev photon energy range, but with much higher and variable coercivity.

The percentage of Fe in $R(Fe,T)_{12}$ film samples range from 85%-91% Fe and therefore ^{57}Fe Mössbauer spectroscopy can be used to investigate the magnetic properties at the level of individual atoms. In this study we have collected Mössbauer spectrums of highly (002) textured $Sm(Fe,Ti)_{12}$ films (absorbers) mounted in such a way that the plane of the film is perpendicular to the γ-ray propagation direction. These spectrums can be used to determine the spin directions of Fe atoms and for that purpose one makes use of the angular dependence of absorption line intensities corresponding to the allowed hyperfine transitions of ^{57}Fe. These transitions are governed by the selection rules $\delta m_I=0,\pm 1$, which gives rise to a equally spaced six absorption line pattern in the absence of electric quadrupole interaction. In the observed Mössbauer spectrums of $Sm(Fe,T)_{12}$, 2nd and 5th absorption lines which have a $\sin^2\Theta$ angular dependence, where Θ is the angle between γ-ray propagation direction and the spin direction, are missing.

In $ThMn_{12}$ type R-Fe-T family the only promising candidate for permanent magnet applications is $SmFe_{11-x}T_x$, where $0.3<x<1$ and T=Ti,V or Ti+V. Although Curie temperature and anisotropy field of $SmFe_{11}Ti$ is comparable to those of $Nd_2Fe_{14}B$ its saturation magnetization, 12 kG, is low compared with 16 kG of $Nd_2Fe_{14}B$. As a result of the low saturation moment, the theoretical maximum energy product of $SmFe_{11}Ti$ is 25 MGOe which is approximately half of that of $Nd_2Fe_{14}B$.

Until the recent discovery of rare-earth intermetallic nitrides, $Sm_2Fe_{17}N_3$, with interesting magnetic properties by J. M. D. Coey at. el.(10), there were no other iron rich intermetallic compounds with intrinsic magnetic properties which are comparable or surpass those of $Nd_2Fe_{14}B$.

This discovery opened a new chapter in rare-earth intermetallic nitrides. In $RFe_{11}Ti$ family with tetragonal 1-12 structure, $SmFe_{11}Ti$ which is uniaxial becomes an easy plane material after nitriding but $NdFe_{11}Ti$ which is uniaxial at room temperature and conical at low temperatures remains uniaxial for the whole temperature range after nitriding(8)(11)(12). The change in magnetocrystalline anisotropy in the $RFe_{11}T$ series, after nitriding, can be understood by the modification of crystal-field interactions at the rare-earth sites due to surrounding nitrogen atoms.

Absorption of nitrogen interstitially in $ThMn_{12}$ type $NdFe_{11}T$, T=Ti or Mo, increases the cell volume but the nitrides retain the parent $ThMn_{12}$ type tetragonal crystal structure. The drastic change in anisotropy field in addition to a large increase in saturation magnetization and Curie temperature after nitriding qualifies the nitrides as a potential candidate for permanent magnet applications(12)(13). We have been able to synthesize highly (002) textured $NdFe_{11}T$ films for T=Ti and Mo and nitride them by heating the films at 500 °C for approximately two hours in a 500 torr nitrogen atmosphere.

The room temperature magnetocrystalline anisotropy fields of the $NdFe_{11}Ti$ and $NdFe_{11}Mo$ films, which are uniaxial, are 10 kOe, and 5 kOe respectively. After nitriding the $NdFe_{11}TN_x$ remained uniaxial, but the anisotropy fields increased to 108 kOe and 130 kOe for Ti and Mo respectively. The $_iH_c$ perpendicular to the film plane of $NdFe_{11}TN_x$ increased to 5.3 kOe, T=Ti, and to 7.2 kOe, T=Mo, after nitriding. At 293 K the highest energy product of 30.2 MGOe was obtained for a T=Mo nitrided sample(12). The increase in Curie temperature ($\delta T_c/T_c$) for $NdFe_{11}Ti$ and $NdFe_{11}Mo$ compounds is ≈30% as reported by Hadjipanayis et al.(13).

The $ThMn_{12}$ type tetragonal RT_{12} structure, which is a superstructure of the $CaCu_5$ type hexagonal RT_5 structure, can be derived by a certain regular substitution of rare-earth (R) atoms by a dumb-bell of two transition metal (T) atoms in the $CaCu_5$ type RT_5 structure. If this substitution is random, it will lead to the disordered $TbCu_7$ type hexagonal RT_7 structure. Thin films of disordered $TbCu_7$ type structure, $R(Fe,Ti)_7$, have been synthesized for R = Sm and Nd(12). The directly crystallized disordered $Sm(Fe,Ti)_7$ films are highly (200) textured while the disordered $Nd(Fe,Ti)_7$ films are highly (110) textured, which results for different sputtering parameters used in synthesizing the films. Although these disordered $R(Fe,Ti)_7$ films are not useful as permanent magnets due to the conical nature of easy direction, their magnetic properties before and after nitriding are interesting and will be discussed in chapter 7.

We have been able to replace at least half of the Mo in $NdFe_{11}Mo$, which seems to be the best candidate for permanent magnet applications in nitrided $R(Fe,T)_{12}$ series, by Co and increase the saturation flux density as well as the anisotropy field of the nitrides. For a $NdFe_{11}Co_{0.5}Mo_{0.5}N_x$ sample the room temperature anisotropy field, H_A, is estimated to be 150 kOe. At 293 K for this Co containing sample the saturation flux, $4\pi M_s$, is 15.5 kG and energy product is 46.3 MGOe(14). This is the highest energy product ever reported for a $ThMn_{12}$ sample. For this same Co containing sample, at 10 K, the $4\pi M_s$ is 17.0 kG, the ${}_iH_c$ is 24.0 kOe, and the energy product is 59.6 MGOe

Films which have a gradient along the substrate length in the Fe to Co ratio have been synthesized to determine the maximum coercivity and anisotropy values that can be obtained for the $Nd(Fe,Co,Mo)_{12}N_x$ compounds. Maximum room temperature coercivities and anisotropies of 11.3 and 190 kOe were obtained for a $ThMn_{12}$ type $Nd_{8.9}Fe_{80.3}Co_{6.0}Mo_{4.8}N_x$, (002) textured, film sample$^{(15)}$. At lower temperatures the coercivity and anisotropy rose smoothly to 29.5 and ≈245 kOe respectively by 10 K. Although this sample shows the highest coercivity ever reported for a nitrided $ThMn_{12}$ sample, the perpendicular to the film plane energy product, BH_{max}=30 MGOe, is low due to the presence of α-Fe. Usually α-Fe appears in films made from gradient targets and it causes a shoulder in the second quadrant decreasing the flux density for small demagnetizing fields.

In 1986, F.J. Cadieu et al. reported a new high $_iH_c$ Sm-Fe-Ti phase in sputter synthesized film samples and the room temperature coercivities of up to 24 kOe had been reported for the preliminary samples$^{(16)}$. The same group has been able to achieve room temperature coercivity values of up to 38 kOe in high $_iH_c$ Sm-Fe-Ti films and to synthesize other Sm-Fe-Ti samples with small additions of Al and Zr with similar coercivities$^{(17)(18)}$. Unlike the directly crystallized films these $_iH_c$ high films have been synthesized in a two step process which involves the deposition of the material in an amorphous state and then crystallization in situ. The structure of the high coercivity phase has recently been found to be that of $Nd_5Fe_{17}$$^{(19)}$.

By investigating these high $_iH_c$ 5-17 compounds further, We have been able to synthesize the high coercivity 5-17 phase in film form for compositions Sm-Fe-V, Sm-Fe-(Ti-V) for a range of (Ti,V), and Sm-Fe-Ti for Ti<1 At.%(20)(21). Binary Sm_5Fe_{17} has also been reported by our group in sputter synthesized films, adding a new stable phase to the binary Sm-Fe system(22)(23).

The best coercivities obtained for Sm-Fe-V and Sm-Fe-Ti-V compositions are 15.7 kOe and 45.6 kOe respectively. A characteristic of these high $_iH_c$ film samples is the drop in magnetization upon entry into the second quadrant. This characteristic drop, which lowers the coercivity, is found to be associated with a second phase. Despite the fact that Occurrence of soft second phases is hard to detect in the x-ray diffraction pattern because line density of powder 5-17 pattern itself is very high, we were able to find the second phases in different 5-17 compounds that causes the drop.

CHAPTER 2 REVIEW OF THEORETICAL ASPECTS

2.1. Hysteresis Behavior

2.2. Crystal Structure of $R(Fe,T)_{12}$ compounds

2.3. Magnetism in RE–TM Intermetallics

2.4. Magnetocrystalline Anisotropy in RE–TM Intermetallics

2.1. Hysteresis Behavior

An external field will usually change the state of magnetization of a ferromagnetic material in a way that is nonlinear and irreversible. The symmetric major hysteresis loop is traced reproducibly provided the applied field (corrected for the demagnetizing effect) is sufficient to achieve saturation in each direction, i.e. $M=\pm M_s$. If the field is reversed short of saturation, then a minor loop wholly within the major loop is obtained. Saturation magnetization (M_s) is an intrinsic property of the ferromagnetic phase, but the remanence M_r and coercivity ${}_iH_c$, defined as the points where the major loop cuts the axes, are not. Hysteresis is an extremely structure sensitive property. Hence M_r and H_c depend in a complex way on the particle size, shape and metallurgical microstructure of the magnet.

The measure of quality for permanent magnets is the energy product $(BH)_{max}$ which is the maximum product of magnetic induction B and internal magnetic field H in the second quadrant of the B–H hysteresis loop. $(BH)_{max}$ provides a measure of the field that can be produced outside a unit volume of magnet materials. The theoretically achievable value of the energy product for a particular material is $(4\pi M_s)^2/4$. For the case where the induction plot is characterized by a straight line in the second quadrant and the coercivity is large enough, the energy product is approximately $(4\pi M_r)^2/4$. In practice, the $4\pi M_r$ value is lower than $4\pi M_s$ because of poor particle alignment, less than theoretical density of the magnet, and second phases in the microstructure. But for the extremely textured, nearly single phase, film samples we used in this study, the perpendicular to the film plane $4\pi M_r$ value is close to $4\pi M_s$ value, because easy c-axes are highly aligned perpendicular to the film plane and the films are very dense as revealed by the SEM photographs.

The internal or effective field at the interior of a magnetic material due to an external applied field is given by $H_{int}=H_{appl}-N_dM$, where N_dM is the demagnetizing field, and N_d is the self-demagnetizing factor. The factor N_d depends solely on the relative geometry of the magnet with respect to the orientation of the external field. Demagnetization factors can be calculated exactly only for an ellipsoid of revolution. A thin film can be treated as a special case of ellipsoid, oblate spheroid or disc.

The normal sample size for magnetometer measurements, that we used in this study, is 4mm by 4mm and the thickness of these films is in the 3-5 μm range. Then the demagnetization factor for a film with thickness t is $N_{d-in}\approx 4\pi(t/4mm)$ for measurements in the film plane, and $N_{d-out}\approx 4\pi(1-t/2mm)$ for measurements perpendicular to the film plane(1). These relations are consistent with $N_{d-out}+2N_{d-in}=4\pi$. For a 3 μm thick film we have $N_{d-out} \approx 4\pi(0.999)$ and $N_{d-in} \approx 9x10^{-3}$, and therefore it is a good approximation that for measurements made parallel to the film plane, $N_d = 0$ and for measurements made perpendicular to the film plane, $N_d = 4\pi$. The possible range for factor N_d is 0 to 4π, with the 4π value corresponding to maximum shielding and thus perpendicular to the film plane demagnetizing field is very large.

Large uniaxial anisotropy is necessary but not sufficient to achieve high coercivity ${}_iH_c$. Spontaneous magnetization vector I_s in a ferromagnetic crystal is always bound to a definite symmetry axis, which is called the axis of easy magnetization (or preferred direction). To deflect vector I_s from this axis by applying an external field, a certain amount of energy must be spent. This energy is called the magnetocrystalline anisotropy energy or magnetic anisotropy energy. The vector I_s "senses" the crystal lattice is due to the magnetic interaction of the magnetic moments of the atoms. Direction perpendicular to the easy axis is known as the hard direction (or hard axis).

The anisotropy energy can be expressed as a series of terms involving the orientation of the total or sublattice magnetization with respect to the crystal axes. In a tetragonal crystal, neglecting the terms corresponding to the basal plane anisotropy, the expression is $E_a = K_1 Sin^2\Theta + K_2 Sin^4\Theta + K_3 Sin^6\Theta$, where Θ is the angle between c axis and the magnetization vector and K_1, K_2, and K_3 are anisotropy constants. The dominant term for the 3d (transition metal) anisotropy is $K_{1T} Sin^2\Theta$, which leads to an easy c-axis when K_{1T} is positive and a hard axis when K_{1T} is negative. Some of the other terms may be important for the rare earths, particularly at low temperatures. The anisotropy energy can be obtained through torque curves, magnetization curves, or magnetic resonance.

Related to the anisotropy energy is the concept of anisotropy field and is defined as that needed to saturate the magnetization in a direction perpendicular to the easy axis.

Various anisotropies are classified as following(24):

(1) Magnetocrystalline anisotropy which is due mainly to spin orbit coupling.

(2) Shape anisotropy which comes from the demagnetization fields.

(3) Stress anisotropy which is produced by a combination of strain and magnetostriction in the crystal.

(4) Induced anisotropy which is due to an asymmetrical distribution of like or unlike atom pairs in the compound.

2.2. Crystal Structure of $R(Fe,T)_{12}$ Compounds

Iron rich $R(Fe,T)_{12}$ compounds crystallize with a stable $ThMn_{12}$-type tetragonal structure which belongs to the space group I4/mmm. $ThMn_{12}$ type tetragonal 1-12 structure, Th_2Ni_{17} type hexagonal 2-17 structure, and $TbCu_7$ type hexagonal 1-7 structure are related to $CaCu_5$ type hexagonal 1-5 structure. Figure 2.1(a) shows the crystal structure of famous $SmCo_5$ permanent magnet compound which has $CaCu_5$ type hexagonal 1-5 structure with space group p6/mmm.

Both RT_{12} and R_2T_{17} are obtained by periodic replacement of rare earth atoms(R) in RT_5 by pairs of transition metal atoms(2T) referred to as dumb-bell atoms and the dumb-bell axis is parallel to the c-axis of the 1-5 unit cell.

$$2RT_5-R+2T=RT_{12}$$

$$3RT_5-R+2T=R_2T_{17}$$

If this substitution is random, it will lead to the disordered hexagonal 1-7 type structure. The R content of disordered 1-7 is lower than that of 1-5 (16.7%) and higher than that of 1-12 (7.7%) or 2-17 (10.5%), because of the presence of some statistically distributed dumbbell pairs of transition metal atoms in the 1-7.

$R(Fe,T)_{12}$, (R=Nd or Sm) compound has the tetragonal $ThMn_{12}$ structure, illustrated in figure 2.1(b). One unit cell consists of 24 atoms (two formula units of $ThMn_{12}$). The single Th (or rare earth) site (2a) is in a highly symmetrical special position (point symmetry 4/mmm). There are three crystallographically distinct Mn(or transition metal) sites (8i,8f and 8j) and in the case of T=Ti, it has a strong 8i site preference. In the structure of RT_{12} the shortest R-T distance occurs between the R atoms and the T atoms at the 8i sites (R-8i=3.01 A) and the shortest interatomic distance occur for T on f and i sites (8i-8i=2.36 A, 8f-8f=2.39 A).

2.3. Magnetism in RE-TM Intermetallics

The magnetism of hard magnetic materials is governed by three basic interactions.

1) Exchange interaction
2) Crystalline Electric-field interactions
3) Spin-orbit coupling

Electrons in a material which may give rise to magnetic behaviors of interest through the above mentioned basic interactions are unpaired electrons, i.e. of partially filled electronic shells when they are localized or partially filled electronic bands when they are free (conduction electrons), otherwise they are in collective non degenerate states of zero spin as well as zero angular momentum which lead solely to diamagnetism. In the rare-earth (R) -transition metal (T) intermetallic compounds, the unpaired electrons are the 4f,5d and 6s electrons associated with the R element and the 3d and 4s electrons associated with the T element.

The number of 4f electrons is normally an integer, n, for most of the rare-earths, $n=Z-57$, where Z is the atomic number. The 4f shell of R element is not the outermost shell and there is little overlap with the 4f shells of neighboring atoms. Thus, the electrons in the 4f shell are strongly localized and R element in a R-T compound has the character of an isolated tripositive ion. The rare-earth ions are characterized by strong intra-atomic exchange interactions and strong spin-orbit coupling interactions leading to ionic moments $\mu = g\mu_B J$ determined by the Hund's rules.

Where, J=Total angular momentum quantum number of the rare-earth ion

$J=L-S$ for $n<7$

$J=S$ for $n=7$

$J=L+S$ for $n>7$

Where, S=Spin angular momentum quantum number which is maximized

$S=n/2$ for $n<7$

$S=(14-n)/2$ for $n>7$

Where, L=Orbital angular momentum quantum number which is maximized consistent with the value of S.

Where g=Land'e g factor for the rare earth ion, defined as the ratio of the magnetic moment (in units of μ_B) to the angular momentum (in units of h)

$$g=1+\{J(J+1)+S(S+1)-L(L+1)\}/2J(J+1)$$

Atomic moments, especially of the heavy rare-earths are large, and crystalline electric-field interactions on these moments can produce strong single ion anisotropy which in uniaxial symmetry give rise to large magnetocrystalline anisotropy fields. Unfortunately the inter-atomic exchange interactions between these moments are too week to induce a magnetic order at sufficiently high temperatures. In pure R metals only Gd has the highest Curie point (290 K) that approaches room temperature.

Magnetic moments of the ferromagnetic 3d transition element are unlike those of the 4f series in that the magnetic electrons are localized. The

3d shell of the transition element is an outer shell, and, therefore participate in metallic bonding of pure transition elements by forming narrow bands. As the 3d transition series is traversed and the d levels fill up, there is a systematic narrowing of the d band. The width of the 3d band of ferromagnetic 3d transition elements iron, cobalt and nickel is of the order of 1 ev and such narrow bands can support an unpaired spin moment. The 3d bands overlap with a partly filled 4s band. The total number of 3d+4s electrons is an integer, but roughly 0.6 electrons of the late transition elements are in the 4s band, so the number of 3d electrons is nonintregal. In 3d transition metals the unshielded 3d electrons experiences the crystal-field produced by neighboring ions, and, therefore the orbital moment is quenched. In this condition, although the total orbital momentum of an ion may have a definite non zero magnitude, its projection on any axis is found to be zero.

The 5d,6s and 3d,4s electrons are involved in the chemical bindings and become valence in the R-T compounds, and, therefore the magnetic moments of the ferromagnetic 3d transition elements can change substantially unlike the 4f atoms, which retain their magnetic moments. The local chemical environment of the 3d element also have an important influence on the magnetic moment of the ferromagnetic 3d transition elemnt, and, hence different crystallographic sites may have quite different atomic moments.

The magnetic coupling between two ions with spin quantum number S and no orbital moment may be represented by the Heisenberg Hamiltonian

$$H_{ij}=-2J_{ij}S_iS_j$$

The exchange integral, J_{ij}, is positive for a ferromagnetic interaction and negative for an antiferromagnetic interaction between the two ions i and j.

The principal magnetic interaction in an R-T compound is that between transition metal atoms (T-T), due to direct overlap of the 3d shells on neighboring sites. That interaction is usually ferromagntic, but depends sensitively on the interatomic spacing r_{ij}. the typical Fe-Fe distance in an iron alloy is about 0.25 nm.

The expression for R-R interaction could be written

$$H_{ij}=-2J_{ij}J_iJ_j$$

since J is the good quantum number for R elements. But, direct exchange interactions between R-R can be ruled out, because 4f electrons are strongly localized, and due to this fact, direct overlapping of the 4f shells of adjacent rare earth atoms is negligible. Indirect exchange interactions between the ionic R elements occur via the spin polarization of the conduction band which is reffered to as the RKKY interaction.

The R-T interaction proceed via an indirect mechanism(25), allows to link the high Curie temperature associated with the 3d electrons and the large magnetocrystalline anisotropy associated with the 4f electrons. The mechanism of this indirect interaction is a rather complex one, and there is intra-atomic exchange coupling between 4f and 5d electrons (4f-5d contact interaction), and an interatomic interaction between 5d and 3d electrons (5d-3d band interaction). The 4f-5d interaction is ferromagnetic, but the 5d-3d interaction is antiferromagnetic when the 5d band is less than half full and the 3d band is more than half full, as they are for alloys of rare earths with the ferromagnetic transition metals. Therefore, an effective antiferromagnetic coupling results between the 3d and 4f spin moments. According to the third Hund's rule, for light rare-earths, J=L-S, and hence magnetization's of light rare earth and transition metal sublattices couple ferromagnetically, where as for Gd and heavy rare-earths, J=L+S, and hence the coupling is antiferromagnetic.

The R-R interactions in the rare-earth transition metal intermetallic compounds are generally quite small by comparison with R-T and T-T interactions, and are generally neglected.

2.4. Magnetocrystalline Anisotropy in RE–TM Intermetallics

Easy axis anisotropy is indispensable for maintaining the metastable domain configuration required of a permanent magnet. On an atomic scale, single–ion anisotropy arises through spin–orbit coupling of the orbital states that are stabilized by the electrostatic field created at the atomic site by the rest of the crystal lattice. The atomic moment has corresponding preferred orientations or local easy directions that reflect the point symmetry of the site. The macroscopic magnetocrystalline anisotropy obtained by summing all the single–ion contributions reflects the overall crystal symmetry.

Both rare–earth sublattice and 3d sublattice contribute to the magnetocrystalline anisotropy. In general, the former is dominant but the contribution of the latter is significant because 3d atoms are the major constituents of the R–T intermetallic compounds. The crystal field acting on the unshielded 3d electrons is stronger than spin–orbit interaction. Although the orbital moment is largely quenched, single–ion anisotropy can still arise when some residual orbital contributions remains. The effect is typically an order of magnitude smaller than for the rare–earth series. But in some instances the 3d sublattice contribution may become quite large as in YCo_5 where it contributes alone and lead to an anisotropy field of 18 T(26).

The observed anisotropy of the rare–earths, which have a localized moment and a well defined magnetic quantum number J, is best described by single-ion model. in this model the magnetocrystalline anisotropy of the rare-earth ion is explained by a hamiltonian that includes the crystalline electric field Hamiltonian (H_{cf}) and the Hamiltonian of other interactions involved ($H_{mag.}$) i.e. the exchange interactions and the Zeeman interactions associated with applied external magnetic field H. In general the exchange interactions are considered within the molecular field approximation so that the corresponding Hamiltonian simplifies into that of a Zeeman interaction $-g\mu_B JH_{ex}$, where H_{ex} is the exchange field. The Hamiltonian for a single ion is

$$H_R = H_{cf} + H_{mag.}$$
$$= H_{cf} + g\mu_B JH_{ex}$$

The first term, crystal field Hamiltonian, has the general form

$$H_{cf} = \sum_{n=0}^{6} \sum_{m=0}^{n} B_n^m O_n^m$$

Where n can take the values 2,4 and 6 for the rare-earth series and O_n^m are the Steven's angular momentum operator equivalents. The parameters B_n^m combine information on the potential created by the distribution of charge in the solid and the form of the charge distribution of the 4f shell.

B_n^m are given by

$$B_n^m = \langle J||\theta_n||J\rangle\langle r^n\rangle(1-\sigma_n)K_n^m A_n^m$$

Where Θ_n is a reduced matrix element known as the Steven's coefficient for the rare-earth ion in question (denoted as α_J, β_J, g_J for n=2,4,6 respectively), $\langle r_n \rangle$ is the average over the 4f wave functions, σ_n is a shielding factor and K_n^m is a numerical constant. The coefficients A_n^m describe the crystal field produced by the surroundings of the rare-earth ion, and should change little in an isostructural series of compounds with different rare earths.

One way of evaluating A_n^m is from the point charge model. Charge q_i are associated with the atomic sites (R_i, Θ_i, ϕ_i), and

$$A_n^m = \{4\pi e/(2n+1)\}\sum_i q_i\, Y_n^m(\vartheta_i \phi_i)/R_i^{n+1}$$

for example

$$A_2^0 = \{4\pi e/5\}\sum_i q_i\, Y_n^m(3\mathrm{Cos}^2\theta - 1)/R_i^3$$

The number of terms in the expansion of the crystal field Hamiltonian H_{cf} is limited by the point symmetry of the rare-earth site. As a example for $ThMn_{12}$ type $RFe_{12-x}T_x$ compounds, the crystal field Hamiltonian at the rare-earth site (2a) with tetragonal point symmetry (4/mmm) takes the form

$$H_{cf} = B_2^0 O_2^0 + B_4^0 O_4^0 + B_4^4 O_4^4 + B_6^0 O_6^0 + B_6^4 O_6^4$$

The leading term $B_2^0 O_2^0$ in the expansion of the crystal field interaction in uniaxial materials is particularly important, because it is the sign of this term, the product of the signs of α_J and A_2^0 that determines whether the rare-earth has hard- or easy-axis anisotropy. The sign of A_2^0 is decided by the crystal structure, but that of α_J depends on whether the shape of the 4f charge distribution is prolate or oblate. For Sm the sign of α_J is positive which is opposite to that for Pr or Nd, a crystal with positive A_2^0 will exhibit easy-axis anisotropy when R=Pr or Nd, but easy-plane anisotropy when R=Sm.

At the lowest temperatures, the second-, fourth- and sixth-order rare-earth anisotropy can all be important, and complex noncolinear magnetic structures may be the result. On raising the temperature, the influence of the fourth- and sixth-order terms will rapidly decline, leaving the second-order rare-earth terms as the principal source of magnetocrystalline anisotropy and this is often the situation at room temperature. Finally, at higher temperatures the more rapid decline of the rare-earth magnetization compared with that of the transition metal can lead to a situation where the iron or cobalt anisotropy is the dominant term up to T_C.

CHAPTER 3 EXPERIMENT

3.1. Synthesis of Films
3.2. Characterization of Films

3.1. Synthesis of Films

The magnetic films that we used in this study were synthesized by RF glow discharge sputter deposition. RF sputter deposition process is the most widely used method to synthesize thin films for research, development and in the industry. Sputter synthesization allows to control the deposition process by changing sputtering parameters such as sputtering gas pressure, target to substrate distance, substrate temperature, bias voltage etc.. Discussions about the sputter process can be found in a large number of journal articles and they are well documented in books(27)(28).

The vacuum chambers used for synthesizing the films consists of a stainless steel chamber and a cryopump aided by an ion pump. The base pressure could be brought to the 10^{-8} torr range and normally operated in the low 10^{-7} torr base pressure. The chamber was normally baked for at least 24 hours before starting sputter deposition.

The targets used in this study had a button shape and were made by arc melting the pure constituents (at least 99.9% pure) in an inert atmosphere into a homogeneous button. To ensure homogeneity the buttons were remelted three or four times while flipping the button after each melting.

Sm with its high vapour pressure and low melting temperature (1072 °C) is highly volatile and hence excess Sm was added to the Sm containing target buttons in order to compensate for Sm losses during arc melting and sputtering, where evaporation from growing film surface occurs due to high substrate temperature.

To get a composition gradient along the length of the substrate, a colinear arrangement of three button targets with varying amount of constituent elements, in the desired ratio, were used. Uniform composition films were made by a colinear arrangement of three uniform composition buttons. Compositions of the films deposited from the same set of targets can be varied through controlling sputtering parameters but not to a large degree.

The films were deposited onto polycrystalline Al_2O_3 substrates. Substrates were heated by a quartz lamp. The preheating temperature of the substrate prior to the sputter deposition depended on the power supplied to the lamp and ranged from room temperature to 900 K. The actual surface temperature of the substrates during sputter deposition were 50 to 80 degree higher than the preheating temperature due to plasma heating. The same quartz lamp was also used for post deposition heating or annealing.

An in plane magnetic field that we call H_S, was applied using permanent bar magnets in a yoke arrangement. The applied field was highly parallel to the substrate plane. Although a range of values from 12 Oe to 5 kOe were available, in this study the value of H_S was held constant at 800 Oe.

The sputtering gas used was Ar and the gas was cycled through the vacuum chamber for the duration of deposition in order to maintain system purity. The sputtering gas pressure ranged from 40 mTorr to 150 mTorr.

The sputtering rate was controlled by input RF power and gas pressure providing that the substrate target geometry arrangement was fixed. One of the advantages of the sputtering technique is that the rate of deposition remains constant with time if the RF power and gas pressure do not vary. These conditions were attained in the sputtering system by using and automatic pressure controller and regulated power supply. The deposition rate in this study ranged from 3 A per second to 9 A per second. The thickness of the films ranged from 0.5 μm to 5 μm.

The special magnetic properties as well as texture of the film magnets were achieved through process control, which include substrate temperature, sputtering gas pressure and deposition rate. There are two methods of sputter deposition differing in the way of crystalliizing the film magnets. First method is subsequent crystallization: the film magnets are first sputter deposited in amorphous form and subsequently crystallized through heat treatment. The second method is direct crystallization: the film magnets are directly crystallized by sputter deposition onto substrates maintained at proper high temperatures.

Nitriding of the directly crystallized films were achieved by thermally heating the samples in 500 Torr N_2 at 550 °C for 2 hours in situ.

3.2. Characterization of Films

The magnetic measurements were made using a Vibrating Sample Magnetometer (VSM). Magnetic fields upto 18 kOe were provided by an iron core magnet and upto 90 kOe by a Nb–Ti superconducting magnet. Since applied fields of the order of three to five times the coercivity are required to magnetize a sample to at least 90% of the saturation value, superconducting magnetic measurements were done for most of the samples. In general coercivity increases with decreasing temperature, and therefore low temperature magnetic measurements, from room temperature down to 5K, were done by using the superconducting magnet. High temperature magnetic measurements, from room temperature upto T_c, were done by using the iron core magnet.

Hysteresis loop measurements were controlled by a personal computer and all the scanning and data acquisition procedures were automated. The size of the sample for measurements was around 0.16 cm^2 and gave magnetic moments in the order of 10^{-1} to 10^{-3}emu. The substrate had a diamagnetic contribution in the order of 10^{-6}emu/gm and was corrected for. The row data were also corrected for diamagnetic contrbutions from the sample holder. The holder contributions were measured at a range of temperature so that the appropriate corrections to the raw data could be made for different measurement temperatures. Contributions from some holders were paramagnetic and the raw data were corrected accordingly. The typlical signal to noise ratio was less than 3%.

Composition of the film was measured through a scanning electron microscope (SEM) coupled with an Energy Dispersive X-ray spectrometer. Details of this technique are well documented in the literature. The analyzer included a liquid nitrogen cooled Si(Li) detector, a multi-channel analyzer, and a dedicated computer for data acquisition and analysis. Elements of the film samples were Sm,Nd,Fe,Co,Ti,V,Mo, and Zr. The electron excited x-ray K_α lines of Co and Fe and the L_α line of the Sm and Nd were used to determine the composition.

The crystal structure, lattice parameters a and c and film x-ray density were determined using an x-ray diffractometer coupled with a Si(Li) detector. An MCA and a computer were coupled with the system for data acquisition and angle scaning control. $Cu_{K\alpha 1}$ radiation were used for diffraction analysis. Precise lattice parameters were determined by using a fitting procedure developed in this lab(1).

To determine the $4\pi M$ accurately, an accurate value for the film thickness (t) was a must. The largest single source of error in determining the $4\pi M$ value came from the film thickness. The thickness of the film was usually determined by the film's mass, area, and density, and the value was checked by viewing the cross-section of a fractured film and substrate in the scanning electron microscope. The scanning electron microscopy was also used to study the film morphology. The resolution of the SEM was 50 A which was normally enough to observe the grains in our films.

Mössbauer spectra were taken at room temperature using a conventional constant-acceleration spectrometer. The γ-ray source was ^{57}Co in a Rh matrix and the calibration was made by using the spectrum of α-Fe at room temperature.

Magneto optical measurements were done at IBM, T. J. Watson Research Center.

CHAPTER 4 SYNTHESIS OF $ThMn_{12}$ TYPE Sm-Fe-T FILMS, T=Ti,V or Ti+V

4.1. Introduction

The Fe rich Sm-Fe phases stabilized into the $ThMn_{12}$ structure by the addition of certain transition metals such as Ti and V have offered the possibility of being able to produce high energy product magnets since their initial discovery(4)(29). These phases exhibit large values of saturation flux densities, $4\pi Ms$, ≥10 kG, anisotropy fields of >100 kOe, and a sufficiently high Curie point of 350 to 400 °C(5). In principle then static energy products of $(4\pi M_r)^2/4=25$ MGOe should be possible provided a value of $4\pi M_r=10$ kG for a remanent flux density and an intrinsic coercivity of at least 5 kOe can be realized. Although it has been possible to synthesize samples with intrinsic coercive force, ${}_iH_c$, in the 6 to 12 kOe range(30)(31)(32)(33), it has been difficult to attain the high remanent flux density and high intrinsic coercivity simultaneously in the same sample which is necessary to realize a high static energy product or magnetic energy density. The reasons for above mentioned difficulty are two fold. First reason is that generally it is thought that a relatively large third element addition is necessary to stabilize this structure which significantly reduces the saturation flux density and in turn remanent flux density. The usual composition thought to be required is approximately $SmFe_{11}Ti_1$ or $SmFe_{10}V_2$. Second reason is that so far, sample preparation techniques yielded only in magnetically isotropic samples with no preferred orientation of crystallites which is necessary to achieve high remanent flux density values. The maximum possible remanent flux density of a magnetically isotropic sample is half the saturation flux density. For example, remanent flux density of mechanically alloyed and subsequently heat treated $Sm_{12}Fe_{73}V_{15}$ sample (magnetically isotropic resin-bonded) is 4.9 kG although it has a coercivity of 10.6 kOe. Its energy product in this case is limited to 5.2 MGOe due to low remanent flux density(33).

The directly crystallized highly oriented sputtered films that we have been able to synthesize overcome both of the normal reasons that limit the available remnant flux densities of the $Sm(Fe,T)_{12}$ systems. These films exhibit an extreme degree of crystallographic texturing such that the c-axes of the grains are aligned perpendicular to the film plane. For this orientation of the crystallites, $4\pi M_r$ can approach $4\pi M_s$. Consequently high values of the static energy product up to 21 MGOe, at 293 K, have been measured perpendicular to the film plane(7). Iron concentration for the highly textured $Sm(Fe,Ti)_{12}$ films that we have been able to synthesize ranges from 85 to 91 at. % Fe and for binary $SmFe_{12}$ that has been synthesized for the first time in Dr. Cadieu's laboratory, it stands at 92 at. % Fe(7). The saturation flux densities, and possible remnant flux densities, are then high and for binary $SmFe_{12}$ it is as high as 14.5 kG.

4.2. Experimental Details

The 2-5 µm thick film samples were synthesized by RF sputtering. The button targets used in these studies were made by arc melting the pure constituents (at least 99.9 % pure) in an inert atmosphere into a homogeneous button. To ensure homogeneity the buttons were remelted three or four times while flipping the button after each melting. The Sm with its high vapor pressure and low melting temperature (1072 °C) is highly volatile and hence excess Sm was added to the buttons in order to compensate for Sm losses during arc melting and sputtering where evaporation from growing film surface occurs due to high substrate temperature. To get a composition gradient with fairly constant Sm but Fe to Ti ratio increased along the length of the substrate, a collinear arrangement of three button targets with constant amount of Sm, while increasing Fe to Ti, ratio were used. The sputter deposition chambers had base pressures below 10^{-7} Torr. The films were deposited at pressures of ≈100 mTorr Ar onto polycrystalline Al_2O_3 substrates preheated to temperatures of 400-550 °C.

4.3. Results and Discussion

4.3.a. Structure

Figure 4.1(b) shows the X-ray diffraction trace of a $Sm_{8.98}Fe_{84.92}Ti_{4.27}V_{1.84}$ film made in order to exhibit moderate, but not extreme texturing and ten diffraction lines can be detected for this directly crystallized film that still exhibit strongly perpendicular anisotropy magnetic properties. The 2Θ values of the observed lines are tabulated in the first column of table 4.1. The second column of table 4.1 and figure 4.1(b) shows the indexing based on a $ThMn_{12}$ cell. This indexing and any other indexing which will be discussed later in this section has been arrived at by fitting the lines to the respective structure types by a program which scans all possible fits within in this case, and most other cases, a specified tolerance of 0.1° 2Θ. The fitting program also calculates the weighted root mean square deviations on the fitting tolerances and in this case $F_{min}=0.01°$ for the ten observed and fitted lines for the 1-12 structure. The unit cell dimensions were a=8.482 A and c=4.798 A. Figure 4.1(a) shows the x-ray diffraction trace of a similar composition Sm-Fe-Ti-V film made in order to exhibit extreme (002) texture. Table 4.2 shows the powder diffraction data for $ThMn_{12}$ type $SmFe_{11}Ti$ compound (a=8.570 A, c=4.796 A)$^{(29)}$.

The x-ray diffraction trace of a moderately (202) textured two element Sm-Fe film, containing 8.5 at% Sm with the remainder being Fe, is shown in figure 4.2$^{(7)}$. A trace of α-Fe is detected for the binary Sm-Fe samples. Ten diffraction lines can be detected for this binary $SmFe_{12}$ film and 2θ values are tabulated in the first column of table 4.3. The binary $SmFe_{12}$ films were generally made to a thickness of approximately 2 µm which allowed the most intense Al_2O_3 lines of the polycrystalline substrate to act as absolute angle checks. Figure 4.2 and last column of table 4.3 shows the indexing based on a $ThMn_{12}$ cell.

As stated in chapter two, $ThMn_{12}$ type tetragonal 1-12 structure, Th_2Zn_{17} type rhombohedral 2-17 structure and $TbCu_7$ type hexagonal 1-7 structure are related to $CaCu_5$ type hexagonal 1-5 structure. The relationships between the lattice parameters are as following.

$a_{2-17}=\sqrt{3}\cdot a_{1-5}$ and $c_{2-17}=2\cdot c_{1-5}$

$a_{1-12}=\sqrt{3}\cdot a_{1-5}=2\cdot c_{1-5}$ and $c_{1-12}=a_{1-5}=a_{1-12}/\sqrt{3}$

Certain lattice planes are connected by the following transformation matrices.

$$\begin{bmatrix} h \\ k \\ l \end{bmatrix}_{2-17} = \begin{bmatrix} 1 & -1 & 0 \\ 1 & 2 & 0 \\ 0 & 0 & 3 \end{bmatrix} \begin{bmatrix} h \\ k \\ l \end{bmatrix}_{1-5}$$

$$\begin{bmatrix} h \\ k \\ l \end{bmatrix}_{1-12} = \begin{bmatrix} -1 & 1 & 0 \\ 0 & 0 & 2 \\ 1 & 1 & 0 \end{bmatrix} \begin{bmatrix} h \\ k \\ l \end{bmatrix}_{1-5}$$

As a result, close reassembles of their X-ray diffraction patterns is expected and certain diffraction lines should be common to the $CaCu_5$, $TbCu_7$, 2-17 rhombohedral, and tetragonal $ThMn_{12}$ structures. In addition to these transformation connected lines the 1-12 structure exhibits a higher density of lines because the structure is not in agreement with the ideal structure transformation size which would have $a_{1-12}=2 \cdot c_{1-5}$ and $c_{1-12}=a_{1-5}$. The deviations from this ideal case are driven by the ordering at the dumbbell sites and leads to the much higher density of lines of the 1-12 superstructure, as opposed to that possible for the fundamental 1-5 structure. These additional superstructure lines can be used to identify the different structures. We limit our analysis only to the binary case where the ten observed x-ray diffraction lines are sharper than that of Sm-Fe-Ti-V films.

Hence the observed lines for which it is possible to index by a disordered 1-5, $TbCu_7$ cell, and rhombohedral 2-17 cell are also shown as column sets one and two of table 4.3. This indexing has been arrived at by the for mentioned fitting program with a specified tolerance of 0.1° 2θ. The weighted root mean square deviations on the fitting tolerance were $F_{min}=0.1°$ for the seven fitted lines for the 1-5 and 2-17 structures and $F_{min}=0.1°$ for the ten observed and fitted lines for the 1-12 structure.

The 1-12 structure is the only one that accounts for all the observed lines. In addition to the fact that all the observed x-ray lines can only be fit by the 1-12 phase, the magnetic properties and Mössbauer data very strongly support that indexing and provide conclusive evidence against the 1-5, 1-7, and 2-17 phases as possible structures which will be discussed in this chapter 6.

4.3.b Magnetic Properties

Most of the Sm-Fe-T films were made so as to exhibit highly (002) texture where the c-axis (easy axis) of the individual crystallites are highly aligned perpendicular to the film plane. The perpendicular to the film plane and in the film plane hysteresis loops as measured at room temperature ,$4\pi M$ versus H internal, are shown in figure 4.3, solid curves. This film sample had a composition of $Sm_{8.04}Fe_{79.16}Ti_{9.11}V_{3.69}$. The original perpendicular to the film plane loop as measured versus H applied is shown in the dashed line. The maximum field applied was ±90 kOe. The demagnetization factors for these film pieces as measured perpendicular to the film plane are $N_d=4\pi(1-t/2mm)$ where t, the film thickness, is measured in mm. The thickness for most of the Sm-Fe-T films have been in the 4 to 5 µm range. For these several micron thick films $N_d=0.998(4\pi)$ which has been taken as 4π within experimental uncertainties. Hence the selfdemagnetization correction for these films is $H_{Int}=H_{appl}-4\pi M$.

Film thickness values as measured by weighing the film and computing the thickness from a known density can often underestimate the film thickness for extreme perpendicular anisotropy films. This is because the actual film density can be less than expected due to the presence of some void structure in the films. This can cause the magnetization to be overestimated which shows up as a negative slope for part of the hysteresis loop of $4\pi M$ versus H_{Int} in the demagnetizing quadrant. A natural limit on the film flux density is set by the requirement that the loop shall not assume a negative slope when corrected for demagnetization effects. A more accurate value of the film thickness can be determined by the use of scanning electron microscope, SEM, for measurement of the film thickness. SEM photographs of fractured sample edges indicate no discernible columnar or void structure for these highly textured films and therefore the structure is very dense. SEM photographs as well as the high flux densities measured perpendicular to the film plane justify the use of $N_d \approx 4\pi$ which would be the case for a dense plate for measurements made perpendicular to the plane.

The room temperature ${}_iH_c$ and static energy product perpendicular to the film plane is 5 kOe and 20.7±0.5 MGOe respectively. The intrinsic coercivity, ${}_iH_c$, in this case is just sufficiently high at 5 kOe so that the static energy product value is not coercivity limited. The ±90 kOe applied field when applied perpendicular to the film plane is nearly sufficient to saturate the film sample as shown in figure 4.3 and the $4\pi M_s$ value is 12.1 kG. The field that would be required to saturate this film to the same value if applied in the film plane is estimated to be 130±10 kOe. For measurements made in the film plane the demagnetization value is nearly 0 so that the applied field is equal to the effective internal field. For these highly aligned films which have the crystallographic c-axis oriented perpendicular to the film plane this anisotropy field is then the magnetocrystalline anisotropy field.

The grain sizes of these films falls in the single domain range so that in the absence of strong pinning effects the ratio of the remanent to saturation flux densities are expected to be governed to a large degree by relaxation by rotation of the magnetization within the grains following an initial magnetization. This ratio is expected to have a value of 0.5, for a

3-d random collection of grains, a value of 0.5*cos(ø) for a 3-d random collection of grains for an easy cone system of cone angle ø. And a value of $2/\pi$ for a system of grains with the easy axes randomly oriented onto the film plane. The high ratio of remanent to saturation, $4\pi M_r/4\pi M_s$, observed perpendicular to the film plane for figure 4.3 is only consistent for a uniaxial system with the easy axes of the crystallites oriented nearly perpendicular to the film plane ($4\pi M_r/4\pi M_s$=0.913). The magnetic properties thus provide very specific expectations to aid in assigning a crystal structure and indexing of observed x-ray diffraction lines.

For these highly textured films as illustrated in figure 4.1(a), the texturing becomes only (002) for the 1-12 tetragonal indexing making c-axis of the individual crystallites perpendicular to the film plane. This indexing is consistent with the observed extreme perpendicular anisotropy and corresponds to magnetic properties observed in figure 4.3. In contrast to this, the transformations and indexing illustrates that the a-axis of the 1-7 structure corresponds to the c-axis of the 1-12 structure. As shown in table 4.3, the (002) c-axis reflection of the 1-12 structure would correspond to the c-axis in plane (110) line of the 1-7 phase, and the c-axis in plane (300) line of the rhombohedral 2-17 phase, and therefore observed magnetic properties rules out 1-7 and 2-17 structures as possible candidates. The magnetic properties of these easy axis in the film plane systems has been documented in a large number of publications dealing with these phases(34)(35).

Thermomagnetic data of a $ThMn_{12}$ type $Sm_{8.85}Fe_{85.32}Ti_{4.25}V_{1.58}$ sample for which the x-ray diffraction pattern is given in figure 4.1(a) is shown in figure 4.4. The Curie temperature of this sample is about 350 °C. All these $ThMn_{12}$ type Sm-Fe-T films have a nearly single phase microstructure which results in a smooth variation of the magnetization with temperature as can be seen in figure 4.4 for this Sm-Fe-Ti-V sample.

The first and second quadrant of hysteresis loops of $ThMn_{12}$ type $Sm_{8.86}Fe_{90.14}Ti_1$ sample, as measured at 293 K, solid curves, and at 15 K, dashed curves, are shown in figure 4.5. X-ray diffraction pattern of the same sample is given in figure 4.5 inset. These films for which the Ti concentration is as low as 1 At. % have a nearly single phase microstructure and gave the first clues against the common belief among the researchers that Ti concentration should be at least 6 At % to stabilize the $ThMn_{12}$ structure in Sm-Fe-Ti films. Low concentration of non magnetic Ti makes the contribution of Fe to the saturation moment in $SmFe_{12-x}Ti_x$ high and perpendicular to the film plane direction $4\pi M_s$ values at 293 K and 15 K are 15.1±0.2 kG and 14±0.2 kG respectively for the film sample shown in figure 4.5.

The in plane (hard direction) hysteresis loops shown in figure 4.5 reveals an interesting feature of Sm-Fe-Ti compounds at low temperature. The in plane loop as measured at 15 K curves upward near 90 kOe, in contrast the in plane loop as measured at 293 K curves downward, indicating an onset of a sharp upturn in magnetization as a function of applied field at low temperatures. This is called a first-order magnetization process

(FOMP) which has been observed in a large variety of magnetic compounds(36)(37). A FOMP is an irreversible rotation of the magnetization vector M between two inequivalent magnetization states M_1 and M_2 under the action of an applied magnetic field, which results in a discontinuity of the magnetization curve along the hard magnetization direction of a ferromagnet. The transition is located at the point where the free energy of the two magnetic phases is equal. The critical field and magnetization, H_{cr} and M_1, the type of transition and the amplitude of the jump $\delta M=M_1-M_2$ are functions of the anisotropy constants and the direction of the applied magnetic field. The maximum applied field of 90 kOe was not enough to see this transition of Sm-Fe-Ti which occurs above 90 kOe as can be seen in figure 4.5.

Figure 4.6 shows the dependence of anisotropy field on T (T=Ti or Ti+V) concentration for $SmFe_{12-x}T_x$ compounds at room temperature. The anisotropy field remains approximately constant for $0.13<x<1.7$ range.

The x-ray diffraction pattern of a $ThMn_{12}$ type $Sm_{8.79}Fe_{81.0}V_{10.22}$ sample (a=8.496 °A, c=4.786 °A) is shown in Figure 4.7. The first and second quadrant hysteresis loops of the same sample are shown in figure 4.8. Since this sample is moderately (002) textured $4\pi M$ value of 8.8 kG at 90 kOe is the $4\pi M_s$ value. The perpendicular to the film plane $_iH_c$ value is 4.3 kOe and anisotropy field H_A is 90±10 kOe.

CHAPTER 5 SYNTHESIS OF $Sm(Fe,Ti)_{12}$ FILMS WITH DIFFERENT TEXTURES

5.1. Introduction

Films of high anisotropy uniaxial materials, with randomly oriented crystallites, do not exhibit a remanent magnetization of more than about half the saturation value. The maximum energy product is then only one-fourth of that possible for an aligned material. This is always the case for films crystallized from amorphous deposits. We have been able to synthesize $Sm(Fe_{1-x},Ti_x)_{12}$ films with the c-axis of the individual crystallites highly aligned perpendicular to the film plane by direct crystallization, and, these films exhibit remnant flux density values close to saturation values for hysteresis loops measured perpendicular to the film plane. We have also studied the change in texture of 1-12 films with sputter deposition parameters such as sputtering gas pressure, P, substrate temperature, ST, and deposition rate, R, for $x \leq 0.1$. It has been possible to modify the sputter deposition parameters systematically so that the film texture mode can be switched from (002) to (222) for this tetragonal system(8). For an optimum set of sputtering parameters the adatom surface mobility on the surface of the growing film is high, and, which results in the extreme alignment of the c-axis perpendicular to the film plane. The observed preferred (ideal) orientations of crystallites can be explained in terms of van der Drift's model of the evolutionary growth of vapor deposited films(38). This model predicts that randomly oriented crystallites which happen to have high-growth-rate directions normal to the substrate will eventually dominate, provided the surface mobility is high.

The role of demagnetization energy , although the magnetic energies are very small compared to crystal lattice energies, is also important in determining different growth modes. The Curie point of the $R(Fe,T)_{12}$ system is ≈310°C and the deposition temperature is in the range from 350°C to 500°C, which is above the Curie point and hence the demagnetization and anisotropy energies are inconsequential in determining the different growth modes.

The c/a aspect ratio can also play a dominant role in determining the texture(1). The texturing of systems that have a c/a ratio that deviates to a large extent from 1 can be controlled by adjustment of the sputtering conditions. The c/a ratio can be much greater than 1, as for $SmCo_3$, or much less than 1, as for $Sm(Fe,T)_{12}$ systems. A material such as $SmCo_3$ has a hexagonal structure with an a lattice parameter of ≈5 A, and c≈24 A. If this material were to be crystallized such that the crystallite c-axes were preferentially aligned onto the film plane, then a high aspect ratio growth would be required. The long c-axes repeat distance in the film plane can be easily disrupted by the impact of the sputtered atom flux on the substrate. The preferential growth mode then has the c-axes skewed out of the film plane. The c/a ratio for $R(Fe,T)_{12}$ systems is ≈0.57 and thus films can be grown with different texture modes by changing sputtering parameters(1).

5.2 Experimental Details

The ≈4 μm thick films have been sputter deposited in a RF diode system onto heated polycrystalline Al_2O_3 substrates. The substrates were sufficiently heated so that the deposits were directly crystallized upon deposition. In order to study the effect of substrate temperature on growth mode, films were made at substrate temperatures(ST) of 645, 660, 675, 690, and 720 K while the sputtering gas pressure(P) was held constant at 150 mTorr of Ar and deposition rate(R) ≈3 Å/s. Films were also made at sputtering gas pressures(P) of 60, 100, and 150 mTorr of Ar and the substrate temperatures(ST) were the same at 645 K and deposition rate(R) for these films was ≈3 Å/s. The relatively high sputtering gas pressures allowed sufficient thermalization of incoming sputtered atoms. To study the film growth dynamics with the growth rate films were made at a relatively high deposition rate(R) of 9 Å/s. The sputtering gas pressure(P) for these films were the same at 150 mTorr of Ar but two different substrate temperatures(ST) 720 K and 800 K were used.

5.3 Experimental Results and Discussion

5.3.a Adatom Surface Mobility and Texture

X-Ray diffraction traces ,$Cu_{K\alpha}$, of $Sm(Fe_{0.99}Ti_{0.01})_{12}$ films synthesized at various substrate temperatures are shown in figure 5.1. The sputtering gas pressure was held constant at 150 mTorr Ar. At low substrate temperatures adatom surface mobility is low and films are highly (222) textured. When the substrate temperature increases, temperature of the growing film surface increases and so is the adatom surface mobility. High adatom surface mobilities are responsible for highly (002) textured films and when the temperature increases from 645 K to 720 K the texture mode changes from highly (222) texture to highly (002) texture.

Figure 5.2 shows the x-ray diffraction traces of films made at various sputtering gas pressures, the substrate temperatures were held constant at 645 K. Films made at sputtering gas pressures of 60 mTorr Ar are highly (002) textured and they are highly (222) textured at 150 mTorr of Ar. Low sputtering gas pressures tend to increase the adatom surface mobility because incoming sputtered atoms carry more energy than at high sputtering gas pressures, where they are thermalized. In addition ion, neutral and electron bombardment is also high at low sputtering gas pressures which result in higher adatom surface mobility. At high pressures adsorbed Ar also limit the adatom surface mobility(39). Therefore at SP of 60 mtorr Ar adatom surface mobility is high and films are highly (002) textured even though the ST is low at 645 K. At high

SP of 150 mTorr Ar adatom surface mobility is low and films are highly (222) textured. Higher substrate temperatures can reduce the effect of pressure and increase the overall adatom surface mobility as can be seen on figure 5.1, where the films made at SP of 150 mTorr Ar, but at ST of 720 K are highly (002) textured.

All the above mentioned films were made at deposition rates in the range of 3 to 4 Å/s. Figure 5.3 shows the x-ray diffraction traces of films synthesized at different deposition rates. The substrate temperatures were the same at 720 K, and the sputtering gas pressure were the same at 100 mTorr Ar. The films, made at high deposition rates of 9 Å/s, are highly (222) textured probably because high deposition rates, like argon pressures, tend to limit the adatom surface mobility. By increasing the substrate temperature from 720 K to 800K at this same high deposition rate, 9° Å/s, texture mode can be switched from highly (222) texture to highly (002) texture as shown in Figure 5.4 because the high substrate temperatures can reduce the effect of deposition rate and increase the overall adatom surface mobility.

X-ray diffraction traces of films synthesized under different sputtering parameters, as explained above, suggest a strong link between the evolution of a preferred orientation and adatom surface mobility.

5.3.b van der Drift's model

van der Drift has suggested that particular crystallographic directions will dominate in vapor-deposited films. To determine these directions, we can consider a freely growing crystal with isotropic coating flux and find the direction from the center to the most distant point on the crystal. This will be the direction of fastest growth and the orientation which dominate the thin film under the extreme assumption of infinite surface diffusion. When the surface diffusion is infinite, crystals in a deposited layer and free-growing crystals expand in the very same way. Lattice planes perpendicular to the fastest growth direction are those with the largest number of atoms per unit area. A preference for orientations, that place the most densely populated atomic planes parallel to the substrate, are commonly seen in evaporated thin films and have been reported for thick sputtered coatings(40).

In figure 5.5 the direction of fastest growth is shown for a number of arbitrarily chosen free-growing tetragonal single crystals. The shape or shapes of the crystals as oriented under the deposition conditions at the nucleating layers could result in different texture modes, although it is often impossible to recognize any crystal shape in the layers. During direct crystallization of films on heated amorphous Al_2O_3 substrates the seed crystallites formed in the nucleating layers are generally randomly oriented. As the film grows in thickness, under the assumption of infinite surface diffusion, all crystals grow equally quickly, therefore the crystals with the direction of fastest growth nearly perpendicular to the substrate are in a favored position in relation to other crystals and will survive.

Figure 5.6 is a two-dimensional representation of this process for (10) bounded cubic crystals, randomly oriented at the nucleating layers, in a two-dimensional space(38). It can be shown that by successively adding equal thickness of material to each face (which assumes infinite surface mobility even along the substrate), eventually the crystallites with the fastest growth direction away from the substrate normal are buried by those which are oriented with the fastest growth direction normal to the substrate. It is possible to observe excellent texture, in other words crystals with the fastest growth direction almost perpendicular to the substrate surface, even at the nucleation stage under an optimized set of sputtering conditions and all these crystals will survive as the film grows in thickness.

Under the other extreme assumption of no surface diffusion at all, a similar construction can be done by adding an amount of material to each face, which is proportional to the cosine of the angle between the face normal and substrate normal. It reveals that there is no selection of orientations and that all orientations grow at approximately the same rate. This would be the case for a normally incident coating flux and zero mobility.

We find that van der Drift's model correctly describes the observed growth of $ThMn_{12}$ type $Sm(Fe,Ti)_{12}$ films and explains not only the evolutionary selection of randomly oriented crystals in the nucleating layers but also how the texture depends on the shape of the crystals at the nucleation stage, in the relatively high mobility limit.

CHAPTER 6 MAGNETO-OPTICAL AND MöSSBAUER STUDIES OF Sm(Fe,T)$_{12}$, T=Ti or Ti+V, PERPENDICULAR TEXTURED FILMS.

6.1. Introduction

6.1.a. Magneto-Optics

Plane polarized light, when reflected from a magneto-optically active surface, will become elliptically polarized, with its major axis slightly rotated with respect to the original direction. The rotation of the polarization direction of plane polarized light upon reflection is called the magneto-optic Kerr effect and is proportional to the component of magnetization lying along the propagation wave vector of the light. At normal incidence Kerr rotation is only sensitive to the magnetization component normal to the film surface and the sign of the Kerr rotation angle depends on whether the magnetization is directed up or down (up - Counter clockwise:$-\Theta_K$, down - Clockwise:$+\Theta_K$).

Magneto-optic effects in magnetic materials are usually discussed in terms of the dielectric permittivity (or conductivity) tensor ε, which for uniaxial symmetry with the easy direction parallel to the z-axis can be written in the form

$$\varepsilon = \begin{bmatrix} \varepsilon_{xx} & \varepsilon_{xy} & 0 \\ -\varepsilon_{xy} & \varepsilon_{xx} & 0 \\ 0 & 0 & \varepsilon_{zz} \end{bmatrix}$$

and it can be shown that

$$\Theta_K - i\varepsilon_K = -i\varepsilon_{xy}/\surd\varepsilon_{xx}(1-\varepsilon_{xx})$$

Where ε_K is the Kerr-ellipticity defined as the ratio between major and minor axes. Both ε_{xy} and ε_{xx} are complex quantities.

The most important technological application of magneto-optics in it's wide field of applications is magneto-optic recording in storage media. Although amorphous films of ternary rare earth (RE) transiton metal (TM) alloys like GdTbFe and TbFeCo, with perpendicular anisotropy are the recording layers in magneto-optic disks(41), it is interesting to study the magneto-optical properties of $ThMn_{12}$ type crystalline sputtered films of $Sm(Fe,Ti)_{12}$(9). The $ThMn_{12}$ type $Sm(Fe,Ti)_{12}$ films that has been used in this study are either highly (002) textured, where the c-axes of the crystallites are normal to the film plane, or highly (222) textured, where the c-axes of the crystallites makes a well defined angle away from the film normal, 39°. In either case, at least 90% of the crystallites can be made with the specific desired texture. The (222) textured films minimize the crystallites grain size which then maximizes the coercivity.

The intrinsic magnetic properties of $Sm(Fe,Ti)_{12}$ films and the sputter process control that can be used to synthesize these films with different texture modes have been discussed in previous chapters.

The crystalline, magnetic and magneto-optical properties of these differently textured, (002) and (222) textured, films are compared. The polar Kerr rotation (Θ_K) and optical coercivities were both obtained from the plots of Θ_K versus applied field. The wavelength dependence of these two parameters were also studied for the photon energy range 1-2.5 ev. These measurements sample only the top few hundreds of angstroms of the film, because light probes the matter over its penetration depth which is typically 200-500 A for metals in the visible wavelength range. Due to this fact optical coercivities may differ from the bulk magnetic coercivities normally measured. The optical coercivities for the (222) textured $Sm(Fe,Ti)_{12}$ films was ≈3.0 kOe, and 1.2 kOe for similar (002) textured films, for photon energies from 1.25 to 2.45 ev(9).

6.1.b. Mössbauer Studies

The study of the magnetic properties of materials at the level of individual atoms, atomic scale magnetism, which is an essential ingredient for understanding magnetic phenomena, has been one of the most frequent applications of Mössbauer spectroscopy. For this purpose the isotope ^{57}Fe has been used far more often than all other Mössbauer isotopes. There are several reasons for the popularity of ^{57}Fe in magnetic material investigations. Certainly, one of the most important reasons is the common occurrence of iron as a constituent of many of the most interesting and technologically important magnetic materials and the percentage of Fe in $Sm(Fe,T)_{12}$ samples ranges from 85%-91% Fe.

Mössbauer spectroscopy can be used to determine the spin directions in magnetically ordered compounds when single crystals are available(42)(43). But when single crystals are not available, highly textured films could be used to obtain considerable information regarding spin orientations. In this study Mössbauer spectrums were collected for highly (002) textured $Sm(Fe,Ti)_{12}$ films (absorbers) mounted in such a way that the plane of the film is perpendicular to the γ-ray propagation direction.

The determination of spin directions makes use of the angular dependence of absorption line intensities corresponding to the allowed hyperfine transitions of ^{57}Fe, which are governed by the selection rules $\delta m_I=0,\pm1$ giving rise to a equally spaced six absorption line pattern in the absence of electric quadrapole interaction. In the observed Mössbauer spectrums of $Sm(Fe,T)_{12}$, 2nd and 5th absorption lines which have a $\sin^2\Theta$ angular dependence, where Θ is the angle between γ-ray propagation direction and the spin direction, are missing. For $Sm(Fe,T)_{12}$ compounds electric quadrapole interaction has no effect on line intensities, because it is much smaller than magnetic dipole interaction and acts as a perturbation. As a result of the electric quadrapole interaction perturbation, hyperfine absorption lines are no longer equally spaced.

To analyze the Mössbauer spectral data, one could fit three subspectra, each subspectra containing Lorentzian sextuplets, corresponding to the three Fe sites 8i,8j and 8f in $Sm(Fe,T)_{12}$, by a least-squares fitting procedure. The parameters that could be obtained are hyperfine field B_{hf}, the quadrapole splitting ε, The isomer shift δ, the line widths and intensities. Since the hyperfine field is proportional to the Fe moment, Fe moment at each site could be obtained. No attempt has been made to analyze the Mössbauer spectra in depth, because least-squares fitting procedure involves too many parameters, even though there are constraints on these parameters there is some flexibility, and most importantly lack of a very good computer program. Although no attempt has been made, the assigning of subspectra to different iron sites will be discussed using the nutron diffraction data analysis and Mössbauer spectra data analysis of similar compounds by other researchers because it sheds light on the intrinsic magnetic properties at the level of individual atoms.

6.2 Results and Discussion

6.2.a. Magneto optical Data

The room temperature saturation polar Kerr rotations for uncoated 2 µm thick, (002) and (222) textured, $Sm(Fe,Ti)_{12}$ films versus photon energy are shown in figure 6.1. These samples contained 84.7 at.% Fe, 9.4 at.% Sm, and 5.9 at.% Ti. Also shown in this figure is the room temperature saturation polar Kerr rotation for Fe films as reported in Refs. 44 and 45. The polar Kerr rotation for these 85 at. % Fe samples is similar to that of pure Fe. As shown in figure 6.1, however, the optical coercivities are appreciably higher than that for Fe alone.

Figure 6.2 shows x-ray diffraction traces, $Cu_{K\alpha}$ radiation, of the same films used for the magneto-optical measurements. The crystal structure is tetragonal with a=8.50 Å, and c=4.79 Å. The crystallite grain size for the (222) textured $Sm(Fe,Ti)_{12}$ films from scanning electron microscopy (SEM) measurements is estimated to be ≈0.20 µm. For the (222) textured films the c-axes of the crystallites makes an angle of 39° away from the film normal. The crystallites are randomly splayed about the substrate plane so that there is isotropy within the plane of the film. Since the $Sm(Fe,Ti)_{12}$ films are a high anisotropy uniaxial system, the magnetic properties measured are very dependent on the degree of crystallite texturing.

Figure 6.3 shows the optical coercivity as measured in air at 300 K versus photon energy for a set of (002) and (222) textured $Sm(Fe,Ti)_{12}$ films. The optical coercivity for the (222) textured films was ≈2.5 times that for the (002) textured films of a similar composition. The high optical coercivity of up to 3.1 kOe at the low end of photon energy of 1.25 ev indicated that the optical measurements were sampling the crystalline textured material. If a degraded surface region was present then a much lower coercivity would be expected specially at the low end of photon energy where the penetration depth is small. The near independence of the optical coercivity for photon energies from 1.25 to 2.45 eV also supports the contention that crystalline material is being sampled and not a degraded surface region.

Hysteresis loops are shown in figures 6.4(a) and 6.4(b) for vibrating sample magnetometer measurements made perpendicular to the plane and parallel to the film plane for (002) and (222) textured $Sm(Fe,Ti)_{12}$ films. The dense packing of the crystallites allow an internal field for the perpendicular measurements using a demagnetization factor of 4π to be computed. Perpendicular to the plane loops versus the applied field are skewed since $H_{int}=H_{appl}-4\pi M$ and in this case $4\pi M$ is large. The polar Kerr rotation for a photon energy of 1.25 eV as a function of the applied field is also shown in figure 6.5. The polar Kerr rotation loop is skewed because of the large film intrinsic flux density.

Optical measurements made on samples that has been stored in air for a year did show considerably lower optical coercivities with a decrease in coercivity for increasing photon energies. The magnetometer measurements for these aged samples were basically unchanged from magnetometer measurements made a year earlier. This indicates, as expected, that the optical measurements are sensitive to surface changes.

The perpendicular to the film plane magnetometer and optical coercivities for the (222) textured $Sm(Fe,Ti)_{12}$ films were 1.5 and 2.4 times, respectively, as large as for similar composition (002) textured films. For the (222) textured films the crystallite c axes make an angle 39° away from the film normal. Besides the angular dependence of the coercive field, the microstructure of the magnet is a important factor which control the coercivity. One well known feature of the microstructure that control the coercivity is the grain size. The coercivity increases as the grain size decreases. Differences in grain sizes incorporated during the direct synthesis of the films onto heated substrates, particularly at the surface, are needed to account for the large differences observed in the coercivities for the (222) versus (002) textured films. Recent models that predict a difference in coercivity for measurements made at an angle to the crystallite c axes only predict a $1/\cos\Theta$ dependence$^{(46)}$. If we assume grain size is independent of the texture, which is not, then for 0° 39° this only predicts a factor of 1.3. But the observed factor for magnetometer measurements, where it samples the whole material across the film thickness, is $\approx$1.5, which indicates the average grain size is smaller in (222) than (002) textured films. For optical measurements, where it samples only the top few hundred Angstroms of the film, the observed factor is $\approx$2.4, which indicates much more prominent difference in grain sizes at the surface layers than the whole film being considered. This could be explained by the fact that the grain size changes as the film grow in thickness and the rate of change of grain size is depend on the texture. It is thought that as the film grows, the grains become larger as they become embedded in the film. It is also thought that the probing sample length of the optical beam or the penetrating depth increases with decreasing wave length similar to pure metals.

The optical coercivity for the (222) textured Sm(Fe,Ti)$_{12}$ films varied from 3.10 kOe at 1.25 eV to 2.92 kOe at 2.45 eV. Since the penetrating depth depends on the photon energy, lower coercivity at higher photon energy indicates a variation of grain sizes even across the surface layers for (222) textured films. The optical coercivity for similar composition (002) textured films was fairly constant at 1.24 kOe for the same photon energy range, and hence the variation of grain sizes across the surface layers is very small for (002) textured films. Therefore the rate of change of grain size as the film grow in thickness is very high for (222) textured films when compared with (002) textured films. For the same composition films as reported here, it was possible to synthesize (002) textured films with perpendicular magnetometer coercivities ranging from 0.8 to 1.6 kOe. The corresponding magnetometer coercivity range for (222) textured films was from 1.6 to 2.5 kOe.

6.2.b. Mössbauer Data

Figures 6.6(a) and 6.6(b) show the Mössbauer spectra of highly (002) textured $Sm_{8.87}Fe_{85.08}Ti_{6.05}$ and $Sm_{9.16}Fe_{89.81}Ti_{1.03}$ films respectively. X-ray diffraction patterns of the same films are shown in figures 6.7(a) and 6.7(b) respectively. These ^{57}Fe Mössbauer spectra were taken at room temperature using a conventional constant-acceleration spectrometer. The γ-ray source was ^{57}Co in a Rh matrix and the calibration was made by using the spectrum of α-Fe at room temperature. The films were mounted on the spectrometer in such a way that the plane of the film was normal to the γ-ray propagation direction with the film side facing the detector. These films are 3-4 μm thick and therefore thick enough to give a magnetic hyperfine spectrum which is typical of a bulk sample spectrum.

For an ^{57}Fe nucleus, each of the two states, the excited state with $I_e=3/2$ ($E_e=14.4$ keV) and the ground state with $I_g=1/2$ ($E_g=0$), has a magnetic moment and therefore will be split by magnetic interaction ($m_e=\pm1/2$, $\pm3/2$ and $m_g=\pm1/2$). Gamma transitions between the degenerate states of the ground state and those of the excited state are governed by the selection rules $\delta I=1$, $\delta m= 0, \pm1$, and hence only six of the eight transitions are allowed. The angular dependence of the relative line intensities of gamma resonance absorption lines, corresponding to the allowed hyperfine transitions of ^{57}Fe, are given in table 6.1. In that table Θ is the angle between the γ-ray propagation direction and the Fe moment.

Since the Sm(Fe,Ti)$_{12}$ films are highly (002) textured the c-axis is normal to the film plane which makes the angle $\Theta\approx0$, only if these compounds are uniaxial with the easy axis parallel to the c-axis. Relative line intensities of both 2nd and 5th lines in the Mössbauer spectra have a $\sin^2\Theta$ angular dependence and therefore one would expect them to be absent in the spectrum. In figures 6.6(a) and 6.6(b) the intensities of 2nd and 5th lines are very small but not zero. This is because, there is some misalignment in mounting the sample, dispersion in the beam itself and some distribution of the c-axis orientations although they are highly (002) textured. All these facts contribute to a smaller non zero value for θ giving rise to a very small 2nd and 5th lines.

Near absence of 2nd and 5th lines in the Mössbauer spectra confirms that these $Sm(Fe,Ti)_{12}$ compounds are uniaxial and reconfirm the assignment of a $ThMn_{12}$ type 1-12 crystal structure based on X-ray diffraction and magnetic data.

The lines in figure 6.6(a), $Sm_{8.87}Fe_{85.08}Ti_{6.05}$, are broader than those in figure 6.6(b), $Sm_{9.16}Fe_{89.81}Ti_{1.03}$. The broadening of the lines can be attributed to the fact that there is a large distribution of adjacent Ti atoms (magnetic perturbation) in 6.6(a) than in 6.6(b) for each Fe site.

Pure magnetic dipole interactions are rarely encountered in the applications of the Mössbauer effect and one always find a situation where a nuclear state is simultaneously perturbed by both magnetic dipole and electric quadrapole interactions. As a result the sublevels of $I_e=3/2$ state of ^{57}Fe are no longer equally spaced. In the case of $Sm(Fe,Ti)_{12}$, electric quadrapole Hamiltonian is very much smaller than magnetic dipole Hamiltonian and could be treated as a first order perturbation on the magnetic dipole interaction. Hence it has no effect on hyperfine transition line intensities but affects the spacing between lines. As can be seen in Mössbauer spectra of figure 6.6 the spacing between 1st and 3rd lines are smaller than that between 4th and 6th lines, indicating a positive value for the average quadrapole splitting parameter, ε_{av}.

Each Mössbauer spectrum shown in figure 6.6 are composed of three subspectra, each subspectra containing six Lorentzian sextuplets, corresponding to the three inequivalent Fe sites 8i, 8j and 8f in $Sm(Fe,Ti)_{12}$. To obtain the Mössbauer parameters one can resolve the spectrum into three subspectra by a least square fitting procedure. Before assigning an Fe site to a subspectra one should know the order of the magnitude of the hyperfine fields at the three different Fe sites.

The interatomic distances between the adjacent atoms in $YFe_{11}Ti$, obtained using neutron diffraction technique by Yang$^{(47)}$, are given in table 6.2, 2a represent the rare earth site. Nutron diffraction studies also reveled that Ti preferentially occupy the 8i site. The exchange interaction between the Fe atoms depend on the interatomic distances and if the distance is larger than 2.45 A, the exchange interactions between the adjacent Fe atoms are positive, otherwise, the interactions are negative$^{(48)}$. The average distances of the Fe-Fe nearest neighbors are 2.71 A, 2.60 A, and 2.51 A for the 8i, 8j, and 8f sites respectively in $YFe_{11}Ti$. Although the average distances are larger than the typical Fe-Fe distance limit for positive exchange interactions, 2.45 A, the shortest Fe-Fe distances occur for Fe on 8f sites (Fe_f–Fe_f=2.381 A), which could result in a weaker interaction or lead to negative interactions between these Fe atoms. Hence an increase in the Curie temperature of these compounds can be expected by a preferential substitution of Fe on the 8f site with other atoms like Co. If we consider nearest neighbor environments the number of nearest neighbor sites for 8i are (5,4,4,1), for 8j are (4,2,4,1), for 8f are (4,4,2,1), where the numbers in brackets refer to 8i,8j,8f and 2a site neighbors. There are 2 Ti atoms per unit cell in

$YFe_{11}Ti$ and they preferentially occupy 8i sites and therefore the probability of any 8i site occupying by a Ti atom is 1/4. So iron on 8i sites has 11.75 iron neighbors, while iron on both 8f and 8j sites has 9 iron nearest neighbors. On the basis of iron coordination number and Fe-Fe distances, there is little doubt that the 8i site should have the largest moment. The Fe-Fe distance suggest that 8f iron should have the smallest moment. Therefore one can write the order of the hyperfine fields at the three different iron sites in $ThMn_{12}$ type $R(Fe,T)_{12}$ compounds as; $H_{hf}(i)>H_{hf}(j)>H_{hf}(f)$.

CHAPTER 7 MAGNETIC PROPERTIES OF $ThMn_{12}$ TYPE $Nd(Fe,T)_{12}N_X$, T=Ti OR Mo, AND $Nd(Fe,Co,Mo)_{12}N_X$ FILMS AND DISORDERED RE(Fe,Ti) PHASES BEFORE AND AFTER NITRIDING

7.1. Introduction

In the Fe rich tetragonal $ThMn_{12}$ type $R(Fe,T)_{12}$ family, where T=Ti,Mo,V,Cr,W or Si, the only promising candidate for permanent magnet applications is $Sm(Fe,Ti)_{12}$(5). A magnetocrystalline anisotropy field of 130±10 kOe and high remnant flux density values have been reported for films of highly (002) textured $Sm(Fe,Ti+V)_{12}$ samples(7). $Nd(Fe,T)_{12}$, T=Ti,Mo or V, compounds have never been attractive for permanent magnet applications, owing to their drastically low magnetocrystalline anisotropy field and relatively low Curie temperature. Recently it has been found that the planer anisotropy Sm_2Fe_{17} compound exhibits a strong uniaxial anisotropy after a nitrogenation heat treatment where nitrogen enters the lattice interstitially and forms a $Sm_2Fe_{17}N_X$

intermetallic compound$^{(10)}$. A similar behavior was also observed in the $ThMn_{12}$ type $Nd(Fe,T)_{12}$, T=Ti,Mo or V, compounds$^{(11)}$. The intrinsic magnetic properties of both the Sm_2Fe_{17} and $Nd(Fe,T)_{12}$ compounds are drastically changed after nitrogenation, resulting in increase of Curie temperature T_c, saturation magnetization M_s, and anisotropy constant K, which make these compounds potential candidates for permanent magnet applications. In $Nd(Fe,T)_{12}$, T=Ti, Mo or V, compounds the increase in Curie temperature $(\delta T_c/T_c) \approx 30\%^{(13)}$.

A general problem for bulk processed $ThMn_{12}$ systems, either with or without nitriding, is that it has been difficult to synthesize samples which exhibit the high flux density and high coercivity simultaneously to provide a high energy product$^{(31)(49)(13)}$.

We have synthesized films of $Nd(Fe,T)_{12}$ samples, for T =Ti or Mo, which were highly (002) textured with the c-axes of the individual crystallites highly oriented perpendicular to the film plane. Because the easy c-axis is highly aligned perpendicular to the film plane, magnetic measurements in the film plane and perpendicular to the film plane allow the magnetocrystalline anisotropy field before and after nitriding to be determined.

The room temperature magnetocrystalline anisotropy fields of the $NdFe_{11}Ti$, and $NdFe_{11}Mo$, films which were uniaxial, were 10 kOe, and 5 kOe respectively. After nitriding the $NdFe_{11}TN_x$ films remained uniaxial, but the anisotropy field increased to 108 kOe and 130 kOe for Ti and Mo respectively. The ${}_iH_c$ perpendicular to the film plane of $NdFe_{11}T$

increased to 5.3 kOe, T=Ti, and to 7.2 kOe, T=Mo sample with some excess Nd, after nitriding. In R-Fe-T family, at 293 K, the highest energy product of 30.2 MGOe was obtained for a T=Mo nitrided sample(12).

We have also studied the change in magnetic properties of thin films of disordered $Sm(Fe,Ti)_7$ and $Nd(Fe,Ti)_7$ upon nitriding. These disordered film samples show a high degree of crystallographic texturing, and due to different sputtering parameters, $Nd(Fe,Ti)_7$ is highly (110) textured, and $Sm(Fe,Ti)_7$ is highly (200) textured. In both these disordered phases the c-axes are randomly distributed in the film plane. The hysteresis loops of disordered $Nd(Fe,Ti)_7$ and $Sm(Fe,Ti)_7$ films, measured in the film plane and perpendicular to the film plane, showed that both are conical systems and the cone angle increased in the former and decreased in the latter upon nitriding(12).

The $Nd(Fe,Mo)_{12}$ compound was shown to be the most promising in film synthesized samples, since highly aligned and α-Fe free samples could be made for T=Mo. Hence, in tetragonal $ThMn_{12}$ type $Nd(Fe,Mo)_{12}$ system, samples have been made with some of the Mo replaced by Co in order to enhance the available flux density. The saturation flux density, $4\pi M_s$, perpendicular to the film surface was 12.9 kG without Co replacement, and was 15.5 kG with 50% of the Mo replaced with Co. The Co containing samples were uniaxial before and after nitriding. For a $NdFe_{11}Co_{0.5}Mo_{0.5}N_x$ sample the energy product at 293 K was 46.3 MGOe and the room temperature H_A was estimated to be 150 kOe. At 10 K the $4\pi M_s$ was 17.0 kG, the ${}_iH_c$ was 24.0 kOe, and the energy product was 59.6 MGOe(14).

To study the effects of anisotropy and coercivity enhancements upon the substitution of small amounts of Co for Fe, we have synthesized films which have a gradient along the substrate length in the Fe to Co ratio, $Nd(Fe_{1-y}Co_y)_{11.5}Mo_zN_x$, z≈0.5. Maximum room temperature coercivities and anisotropies of 11.3 and 190 kOe were obtained for a $ThMn_{12}$ type $Nd_{8.9}Fe_{80.3}Co_{6.0}Mo_{4.8}N_x$ (002) textured, film sample. At lower temperatures the coercivity and anisotropy rose smoothly to 29.5 and ≈245 kOe respectively by 10 K(15).

7.2. Experimental Details

Thin films were directly crystallized onto heated polycrystalline Al_2O_3 substrates by RF sputtering. The sputtering gas pressure was 100 mTorr of Ar for the disordered 1-7 phases and it was 60 mTorr of Ar for the 1-12 phase. The substrate temperature was held at 700 K for the $Nd(Fe,T)_{12}$ and $Nd(Fe,T)_7$ phases. Although the substrate temperatures were held at 700 K, in the case of $Nd(Fe,T)_{12}$ the temperature of the growing film surface was higher than that of $Nd(Fe,T)_7$ due to the low sputtering gas pressure. Substrate temperatures were held at 575 K for the disordered $Sm(Fe,Ti)_7$ phase. All the phases were highly textured and the growth mode was different for each phase.

The approximately $Nd(Fe_{1-y}Co_y)_{11.5}Mo_{0.5}$ aligned film samples were synthesized by RF diode sputtering from a collinear arrangement of three targets with the compositions as indicated.

Target	A	B	C
	at.%	at. %	at %
Nd	8	8	8
Fe	87.5	84	78.5
Co	0	4	9
Mo	4.5	4	4.5

The atomic fractions of Nd and Mo thus remained fairly constant across the length of a substrate while the relative amounts of Co to Fe increased along the substrate length from the side opposite target A to the side opposite target C. The Co atomic compositions ranged from 1.3 at.% to 6.3 at.% of the metallic elements across the substrate. Some Mo was retained in the sample since in our experience this aids in obtaining coercivity and suppressing α-Fe formation for stoichiometric samples.

The samples were nitrided after deposition by thermally heating the samples in 500 Torr N_2 at 550 °C for 2 hours. The film compositions were determined by directly analyzing film regions with electron excited x-ray fluorescence in a scanning electron microscope, SEM. The magnetic properties were measured by two different vibrating sample magnetometers. A low field one at applied fields upto 18 kOe, and a high field VSM with applied fields to 90 kOe. The sample thicknesses were determined by SEM measurements. The x-ray diffraction traces were collected by a digital stepping motor system using $Cu_{K\alpha}$ radiation. Corresponding samples before and after nitriding were measured. A demagnetization factor of 4π was used to compute the flux densities as measured perpendicular to the film plane, and zero for the in plane measurements.

7.3. Results and Discussion

7.3.a. $Sm(Fe,Ti)_{12}N_X$ and $Nd(Fe,T)_{12}N_X$, T=Ti or Mo, Compounds

Figure 7.1 shows x-ray diffraction traces for a highly (002) textured $ThMn_{12}$ type $Sm_{8.90}Fe_{85.35}Ti_{5.75}$ film before and after nitriding. An expansion of the lattice parameters is observed with a maximal volume increase of ≈7%. This 7% figure includes stress effects arising from differences in expansion coefficients of the film and substrate. Other less textured films have been used to precisely determine the a and c parameters with and without nitrogenation.

The magnetic properties of the nitrided films as shown in figure 7.2 are very different from those of the original films. The nitrided films exhibit the easy axis in plane which is only consistent with nitrogenation resulting in a conversion from easy axis to an easy plane system.

Hysteresis loops of a highly (002) textured $Nd(Fe,Ti)_{12}$ film sample, measured perpendicular and parallel to the film plane at 293 K are shown in figure 7.3(a). Although $Nd(Fe,Ti)_{12}$, which is uniaxial, is a soft magnetic material, the magnetization reversal process is similar to the highly (002) textured $Sm(Fe,Ti)_{12}$ films because the in plane coercivity is larger than that perpendicular to the film plane. Figure 7.3(b) shows the hysteresis loops measured at 10 K. The kink in the perpendicular to the film plane loop, and the loop shape, indicate a spin reorientation below room temperature. The hysteresis loops of nitrided similarly prepared

$Nd(Fe,Ti)_{12}$ films measured at 293 K are shown in figure 7.3(c), and at 10 K in figure 7.3(d). The drop in magnetization upon entry into the second quadrant is due to the α-Fe which has been precipitated during nitriding of the films. As can be seen from the figures 7.3(c) and 7.3(d), after nitriding $Nd(Fe,Ti)_{12}N_x$ remain uniaxial for the whole temperature range.

The x-ray traces of $Nd(Fe,Ti)_{12}$ before and after nitriding are shown in figure 7.4. The perpendicular to the film plane $4\pi M_r$ value at 293 K is 12 kG and this value is close to the $4\pi M_s$ value since the films are highly (002) textured. The high degree of (002) crystallographic texturing allowed the magnetocrystalline anisotropy field to be determined by extrapolating the perpendicular and in plane hysteresis loops. The magnetocrystalline anisotropy field of $Nd(Fe,Ti)_{12}$ sample is 108 kOe.

Figures 7.5(a) and 7.5(b) respectively show, T=293 K and T=10 K, first and second quadrant hysteresis loops of a $Nd(Fe,Mo)_{12}N_x$ sample. For the T=293 K loop , $4\pi M_s$=12.9 kG, ${}_iH_c$=5.3 kOe, and BH_{max}=24.4 MGOe. The anisotropy field extrapolates to 130 kOe. For the T=10 K loop, $4\pi M_s$=14.7 kG, ${}_iH_c$=22.8 kOe, and BH_{max}=46.64 MGOe. The anisotropy field extrapolates to 239 kOe. Figure 7.6 shows x-ray diffractometer traces for the sample of figure 7.5 before and after nitriding. Figure 7.6(a) shows the counts for a step of 0.03 degrees per channel and a dwell time of 5 seconds per channel. Figure 7.6(b) shows an expanded count scale for the nitrided sample used to quantify the degree of c-axis alignment and to measure the presence of α-Fe. The major reflection present is the (002) reflection of the $ThMn_{12}$ phase. The integrated intensity ratio of the

$ThMn_{12}$ (202) to (002) reflections is 0.0035. There is no detectable presence of α-Fe in this sample.

Figure 7.7 shows room temperature hysteresis loops for a sample made with some excess Nd after nitriding. For this sample at 293 K, $4\pi M_s$=12.8 kG, $_iH_c$=7.2 kOe, and BH_{max}=30.2 MGOe. X-ray diffraction traces before and after nitriding of such a sample are shown in figure 7.8. Figure 7.8(b) shows an expanded scale to quantify the $ThMn_{12}$ (222) peak and to detect α-Fe, if present.

It is possible that the small amount of α-Fe detected was mainly confined to the film surface. We have shown for $Sm_2Fe_{17}N_x$ samples that the relative size of the α-Fe diffraction peak can be reduced by sputter etching the outer film surface(50).

The x-ray traces of all the highly (002) textured $Nd(Fe,T)_{12}$, T=Ti or Mo, and $Sm(Fe,Ti)_{12}$ films before and after nitriding, exhibit the shift of line positions towards lower angles of 2θ after nitriding. The effect of nitrogen on the structure is essentially to expand the unit cell, without changing the tetragonal symmetry of the 1-12 parent compound. By neutron diffraction studies Yang et al. found that the nitrogen occupied the interstitial 2b sites(11) (1/2,1/2,0≡0 0 1/2). There is no limitation on N atoms populating the 2b sites and at full occupancy, when N occupy the all 2b sites, the value of x is one. The volume expansion due to nitrogenation (δV/V) in the bulk samples of $R(Fe,Ti)_{12}$ series is in the 3-5% range, 5 being the value for full N occupation. But the volume expansion of 1-12, Sm-Fe-Ti film is 7% due to the stress effects. The volume expansion not only depends on the stress effects but also on the N content.

Interstitial absorption of nitrogen gives rise to profound changes of magnetocrystalline anisotropies in $R(Fe,T)_{12}$ compounds. The easy magnetization direction of $Sm(Fe,Ti)_{12}$ compounds change from easy axis to easy plane upon nitriding where as the easy direction of $Nd(Fe,T)_{12}$, T=Ti or Mo, still remain uniaxial.

The easy direction is determined by the possibly competing contributions to the anisotropy, with different temperature dependence, for the rare earth and iron sublattices. The iron sublattice has an easy c axis in the $R(Fe,T)_{12}$ series at all temperatures before and after nitriding $(K_{1Fe})>0$. The sign of the rare earth sublattice anisotropy is determined by the product of the second-order Stevens coefficient α_J and the second-order crystal-field parameter A_{20}; $K_{1R}=-(3/2)\alpha_J\langle r^2\rangle A_{20}\langle O_{20}\rangle$, O_{20} is the Stevens operator.

Sign of A_{20} is negative in this tetragonal structure. However, after nitriding of $R(Fe,T)_{12}$ compounds, the modification of crystal-field at the rare earth ions, which is directly due to neighboring nitrogen atoms, makes the sign of A_{20} becomes positive(51). Hence the Nd^{3+}, Tb^{3+}, Dy^{3+}, and Ho^{3+} ions, which possess a negative second-order Steven's factor, can exhibit uniaxial anisotropy, whereas Sm^{3+} and Er^{3+} ions can exhibit the basal-plane anisotropy.

The large anisotropy field H_A of $NdFe_{11}TN_X$, T=Mo or Ti, is very favorable for permanent magnet applications. Although $NdFe_{11}Ti$ and $NdFe_{11}Mo$, which are uniaxial at room temperature, exhibit spin reorientations at low temperatures, no spin reorientations have been observed in $NdFe_{11}TiN_X$ and $NdFe_{11}MoN_X$ compounds, indicating they have uniaxial anisotropy at all temperatures. Although both $NdFe_{11}TiN_X$ and $NdFe_{11}MoN_X$ have good intrinsic magnetic properties only $NdFe_{11}Mo$ films can be synthesized free of α-Fe and and no precipitation of α-Fe has been observed in these films during nitrogenation. A shoulder of the magnetization curve in the second quadrant, which is often associated with α-Fe, drastically reduces the energy product. Hence $NdFe_{11}MoN_X$ films with a slight excess of Nd is the best candidate for permanent magnet applications.

7.3.b. Disordered $R(Fe,Ti)_7$ and $R(Fe,Ti)_7N_X$, R=Sm or Nd, Phases

Highly textured and well characterized phases were also made, which did not exhibit an appreciable increase in coercivity upon nitriding. Such films were indexed to the disordered $TbCu_7$ phase. It was possible to make $Sm(Fe,Ti)_7$ films, as shown in figure 7.9(a) and 7.9(b) before and after nitriding, such that all the crystallites had one texture mode. In these textured $Sm(Fe,Ti)_7$ films a-axis is perpendicular to the film plane and c-axis is randomly distributed in the film plane. The x-ray traces showed no α-Fe before and after nitriding, and the second quadrant drop often associated with α-Fe was absent from the hysteresis loops. Hysteresis loops as measured at 293 K, before and after nitriding, and at 10 K after nitriding, are shown in figure 7.10. Solid line - in the film plane, dashed line - perpendicular to the plane. Before nitriding, in the film plane and perpendicular to the film plane hysteresis loops, figure 7.10(a) showed at low fields the perpendicular to the film plane moment was higher than the in film plane moment. But after nitriding, figure 7.10(b), this was reversed and the in the film plane moment was very much higher than the perpendicular to the film plane moment at low fields. The before and after nitriding loops were both constricted near H=0.

In a conical system the process of magnetization reversal very easily takes place with the rotation of M_S on the envelope of the cone, since this is the anisotropy minimum. Obviously the result is a rapid change of the magnetization and constriction of the loop, vanishing coercivity, at low fields. Hence the disordered $Sm(Fe,Ti)_7$ is a conical system and magnetization reversal indicated there was a decrease in cone angle after nitriding because the c-axes were randomly distributed in the film plane.

The properties of disordered $Nd(Fe,Ti)_7$ films before and after nitriding were found to be similar to the disordered $Sm(Fe,Ti)_7$ films. The $Nd(Fe,Ti)_7$ films were highly (110) textured with the c-axes of the individual crystallites randomly distributed in the film plane. X-ray diffractometer traces, $Cu_{K\alpha}$ radiation, before and after nitriding are shown in figures 7.11(a) and 7.11(b). The disordered Nd phases did contain some α-Fe so that the interpretation was not as clear cut as for the Sm disordered phases. Figures 7.12(a) and 7.12(b) before nitriding, and 7.12(c) and 7.12(d) after nitriding, show hysteresis loops of a similarly prepared disordered $Nd(Fe,Ti)_7$ sample at 293K and at 10K. The perpendicular loop came up faster before and after nitriding, but in plane loop came up considerably slower after nitriding which indicated that the easy axis direction was shifted to lie more out of the plane away from the c-axis direction. Thus the cone angle was increased after nitriding. The in plane hysteresis loops were very constricted as for the $Sm(Fe,Ti)_7$ disordered phases.

7.3.c. $Nd(Fe,Co,Mo)_{12}N_X$ Compounds

In $ThMn_{12}$ type $Nd(Fe,T)_{12}N_X$ family, as explained before, $Nd(Fe,Mo)_{12}N_X$ is the best candidate for permanent magnet applications. Hence samples have been made with some of the Mo replaced by Co in order to enhance the remanent flux density. Figure 7.13 shows the room temperature hysteresis loops for a sample containing 50% of the Mo replaced with Co, $NdFe_{11}Mo_{0.5}Co_{0.5}N_X$. The saturation flux density measured perpendicular to the film plane was 15.5 koe. The energy product measured perpendicular to the film plane was 46.3 MGOe and was not coercivity limited since ${}_iH_c$ was 8.7 kOe. The anisotropy field estimated by extrapolating the in-plane flux density to the perpendicular value was 150 kOe. Figure 7.14 shows T=10K measurement for the sample of figure 7.13. The $4\pi M_s$=17 kG, ${}_iH_c$=24.0 kOe, and the BH_{max} value was 59.6 MGOe. At 10 K, H_A was estimated to be 250 kOe. Figure 7.15 shows x-ray diffraction traces for such a Co substituted film before and after nitriding. Neither α-Fe nor any free Nd can be seen in the nitrided sample as shown in figure 7.15(b).

The magnetic and x-ray data for the three types of samples after nitriding are summarized in table 7.1. The magnetic data shown are room temperature values for VSM measurements with H perpendicular to the film plane. Samples which had 50% of the Mo replaced by Co exhibited an enhanced $4\pi M_s$ of 15.5 kG versus 12.9 kG for corresponding samples without Co. The room temperature static energy product of the sample with a slight Nd excess was 30.2 MGOe. For the sample with Co for Mo (50%) replacement the energy product at room temperature was 46.3 MGOe.

To study the effects of anisotropy and coercivity enhancements upon the substitution of small amounts of Co for Fe, we have synthesized films which have a gradient along the substrate length in the Fe to Co ratio, $Nd(Fe_{1-y}Co_y)_{11.5}Mo_zN_x$, $z \approx 0.5$. Figure 7.16 shows the hysteresis loops for a $Nd_{8.0}Fe_{85.8}Co_{1.8}Mo_{4.4}N_x$ sample as measured at 293K, perpendicular to the film plane, and in the film plane. For this sample the room temperature remanent flux density was 16.2 kG and is essentially the same as the saturation value. The room temperature ${}_iH_c$ perpendicular to the plane was 8.7 kOe, and the static energy product was 30.4 MGOe. The large drop in flux density upon entering the demagnetization quadrant greatly lowers the possible energy product from that theoretically possible for such a high remanent flux density. The drop in flux density as H internal reverses is expected because such samples contain a trace of α-Fe as indicated in the x-ray diffractometer data shown in figure 7.17 This sample was strongly (002) textured, but not to the same extreme degree as previous films which were made to maintain uniform composition films. The room temperature magnetocrystalline anisotropy obtained by extrapolating the in plane flux density to the perpendicular value was 145 kOe.

Figure 7.18 shows hysteresis loops as measured at 293 K for a $Nd_{8.9}Fe_{80.3}Co_{6.0}Mo_{4.8}N_x$ predominantly (002) textured film sample. The main points of interest for this sample are that the room temperature coercivity has been increased to 11.3 kOe and the room temperature anisotropy field to an estimated 190 kOe. The room temperature static energy product perpendicular to the plane was also respectable at 30 MGOe. Figure 7.19 shows an x-ray diffraction trace after nitriding for this sample. Since this sample was only 1.5 μm thick, the characteristic polycrystalline Al_2O_3 substrate lines are clearly evident at $2\Theta=35.13°$, 37.78°, 43.36°,and 52.55°. Only a small α-Fe peak is evident at 44.70°. The second strongest $ThMn_{12}$ reflection is the (202). Hysteresis loops for this sample measured at 10 K are shown in figure 7.20. By 10 K the magnetic properties had increased to $4\pi M_s=16.5$ kG, ${}_iH_c=29.5$ kOe, and $BH_{max.}=40.5$ MGOe. The anisotropy field at 10 K can only be estimated to be a relatively high value of 245 kOe.

Exceptionally high values of intrinsic coercivity and anisotropy fields have been measured in film samples made with a gradient in the Fe to Co ratio along the substrate length. The highest intrinsic coercivity and anisotropy values obtained at 293 K were ${}_iH_c=11.3$ kOe and $H_A=190$ kOe. The corresponding values were 29.5 kOe and 245 kOe at 10 K. Despite the new high values of ${}_iH_c$ and H_A obtained for an Fe to Co ratio 13.4 to 1, the room temperature BH_{max} value of 30 MGOe was comparatively low because of the partial decrease of the flux density for small demagnetizing fields. A new high value of H_A=190 kOe was also measured at 293 kOe. Even though this value must have a large tolerance because it was obtained by extrapolation from high field measurements to only 90 kOe, it should be noted that this value is about twice the room temperature value for $Nd_2Fe_{14}B$(52), and higher than the room temperature value of nitrided $Sm_2Fe_{17}N_3$(53).

CHAPTER 8 HIGH COERCIVITY R_5Fe_{17} PHASE IN Sm-Fe-T, T=Ti,V OR Ti+V, SYSTEM.

8.1. Introduction

The structure of the high coercivity phase, reported for the first time in sputtered Sm-Fe-Ti films for a composition ratio of Sm:Fe:Ti=20:70:10, that exhibited a room temperature intrinsic coercivity, ${}_iH_c$, of 38.5 kOe as measured at 293 K(17), has recently been found to be that of Nd_5Fe_{17}(19). The crystal structure of Nd_5Fe_{17} belongs to the hexagonal space group p63/mcm with lattice parameters a=20.214 A and c=12.329 A and there are 12 formula units (z=12) in this relatively large unit cell. The hexagonal 5-17 lattice parameters for $Sm_{20}Fe_{70}Ti_{10}$ are a=20.169 A and c=12.354 A. Room temperature intrinsic coercivities of 50 kOe has been achieved subsequently for the same composition Sm-Fe-Ti compounds by mechanical alloying.(54)

We were able to synthesize the high coercivity 5-17 phase in sputtered films for compositions Sm-Fe-V, Sm-Fe-(Ti-V) for a range of (Ti,V), and Sm-Fe-Ti for Ti<1 At.%(20)(21). Binary Sm_5Fe_{17} has also been reported by our group in sputtered films, adding a new stable phase to the binary Sm–Fe system(22). The films for the whole composition range have been made in a two step process. First, the material has been deposited in an amorphous state, and then the deposits have been crystallized in situ. This method of preparation generally produces fine grained crystallites, 300 to 600 A in diameter. The orientation of such crystallites is expected to be random and therefore samples are magnetically isotropic. The best coercivities obtained for Sm–Fe–V and Sm–Fe–Ti–V compositions are 15.7 kOe and 45.6 kOe respectively. Magnetic measurements shows that the ratio of remanent magnetization (B_r) to the magnetization at 90 kOe, the maximum applied field available in the lab, is substantially greater than 0.5 expected for a random collection of single domain uniaxial grains. The reason for this is that the field of 90 kOe is not sufficient to saturate the magnetization. All of these magnetic measurements of ultra high coercivity samples are for the as measured, usually minor, hysteresis loop values without any second phase corrections.

The drop in magnetization upon entry into the second quadrant, typical of these very high coercivity samples, is thought to be associated with a second phase which lowers the coercivity. Occurrence of soft second phases, in minute amount, is hard to detect in the x-ray diffraction pattern because line density of powder 5–17 pattern itself is very high. Precipitation of $Sm(Fe,Ti)_2$ in addition to the dominant 5–17 phase from a Sm rich matrix is discussed for the composition Sm–Fe–Ti, Ti≈1 At.%. Presence of possible second phases in a Sm–Fe–Ti–V sample, Ti:V≈2:1, which exhibited a room temperature ${}_iH_c$ of 44 kOe, is also discussed using thermomagnetic data. In Sm-Fe-V films $ThMn_{12}$ type $Sm(Fe,V)_{12}$ precipitates as a second phase as can be seen in x-ray diffraction pattern and unlike in other hard phase compositions the second phase here is not a soft magnetic phase.

The hexagonal unit cell volume shows a clear and systematic expansion upon the partial replacement of Fe with V, V+Ti, and Ti, indicating that these elements are acting as replacement elements for Fe in the primary magnetic phase(23). A 10% replacement of Fe by V caused a 0.83% volume expansion and a 11% replacement of Fe by Ti caused a 1.63% volume expansion. In Ref. 19 it has been estimated that a 10% replacement of Fe by Ti leads to a volume expansion of 2%.

In contrast to the Sm-Fe-T, T=Ti, V, and Ti+V, samples, similarly prepared Sm-Fe-Zr samples have not exhibited the high $_iH_c$ phase, but instead form into a disordered 1-5, $TbCu_7$ type structure(20). The lattice parameters for disordered 1-5 type Sm-Fe-Zr are a=5.109 Å and c=4.074 Å. The room temperature $_iH_c$ value and $4\pi M$ value, at 18 kOe, are 6.4 kOe and 5.6 kG respectively(21).

Nd_5Fe_{17} films prepared by subsequent crystallization showed soft magnetic properties where as Sm_5Fe_{17} was magnetically hard with a room temperature coercivity of 14.7 kOe(22).

8.2. Experimental details

The high $_iH_c$, 5–17, Sm–Fe–T films have been made in a two step process. First, the material has been deposited in an amorphous state onto water cooled Al_2O_3 substrate by rf sputtering. Amorphous films have then been crystallized in situ by annealing them in an Ar atmosphere. Annealing temperature was in the 600–700 K range and annealing time was 135 minutes. Targets for rf sputtering were made by arc melting the pure constituents (at least 99% pure), with a desired ratio , in an Ar atmosphere into a homogeneous button. Excess Sm was incorporated into the button targets to compensate for Sm losses during arc melting and film synthesis process. The sputtering gas used was Ar at pressures from 100 to 150 mTorr. These pressures were high enough to thermalize the sputtered atoms before their arrival at the substrate. A magnetic field, that we call H_s, $H_s<2.5$ kOe, was applied in the substrate plane during deposition and subsequent crystallization processes. The effect of the field is thought to be minor besides the fact that the films are magnetized as they are removed from the sputtering system.

8.3. Results and Discussion

X ray diffraction pattern of a 5-17 type $Nd_{20.14}Fe_{79.86}$ film are shown in figure 8.1. The vertical lines shows the angles and intensities of calculated powder pattern of Nd_5Fe_{17} (a=20.214 A and c=12.329 A), obtained from ref. 19. Reflections that does not belong to 5-17 phase has been found to be that of Nd_2Fe_{17} and stars indicate the angles of Nd_2Fe_{17} powder pattern lines with relative line intensities, $I/I_0>20$. In plane hysteresis loop of the same sample which is magnetically soft, is shown in figure 8.2.

Figure 8.3 shows the x-ray diffraction pattern of a almost single phase $Sm_{21.5}Fe_{69.1}Ti_{4.7}V_{4.7}$ sample. Solid curve is the x-ray fit for the diffraction pattern which is the sum of 44 modified Lorentz functions corresponding to the 44 reflections, that could be expected in the 24 to 54 degree range. The 2Θ angle (position), half width (w), height (y_0), area (intensity-I), and relative line intensity (I/I_0) of each reflection is shown in table 8.1. All the observed 39 lines given in table 8.1 could be fitted, within 0.05° with a weighted root mean square angular deviation of 0.1°, to a 5-17 type hexagonal cell with a=20.130 A and c=12.334 A. No lines has been found that does not belong to the 5-17 phase.

X-ray diffraction trace of a $Sm_{19.5}Fe_{79.5}Ti_1$ film is shown in figure 8.4, solid line is the x-ray fit for this pattern. All the observed lines between 24 to 54 degree range could be fitted within 0.05° to a 5-17 type hexagonal cell with a=20.112 A and c=12.31 A. In plane hysteresis loop of this Sm-Fe sample with a trace of Ti is shown in figure 8.5 (solid line). The second quadrant drop in the hysteresis loop is very small and the loop shape together with the x-ray trace suggest the amount of second phases present is extremely small. Figure 8.6(a) shows the x-ray diffraction trace of a Sm rich Sm-Fe sample with a trace of Ti, $Sm_{26.6}Fe_{72.3}Ti_{1.1}$. During subsequent crystallization, in this Sm rich film, $Sm(Fe,Ti)_2$ precipitates as a second phase from the Sm rich matrix in addition to the main 5-17 phase. In figure 8.6(a), stars indicate the $SmFe_2$ powder pattern line positions. For comparison, x-ray diffraction trace of the almost single phase $Sm_{19.5}Fe_{79.5}Ti_1$ film is shown in figure 8.6(b). Presence of magnetically soft $Sm(Fe,Ti)_2$ as a second phase not only decreases the coercivity but also kills the loop shape, in the second quadrant, as can be seen in the hysteresis loop of $Sm_{26.6}Fe_{72.3}Ti_{1.1}$, shown in figure 8.5, dashed line.

The maximum room temperature intrinsic coercivity, ${}_iH_c$, observed for a subsequently crystallized sputtered film sample was 45.6 kOe for the composition $Sm_{15.1}Fe_{70.4}Ti_{10.8}V_{3.7}$. The in plane hysteresis loop of a similar composition $Sm_{16.96}Fe_{70.2}Ti_{8.99}V_{3.85}$ film, measured at 293 K, is shown in figure 8.7, solid line. Dashed line in figure 8.7 shows the hysteresis loop measured in plane at 5 K for this high ${}_iH_c$ Sm-Fe-Ti-V film. The observed in plane coercivity at 293 K and at 5 K are 43.4 kOe and 75 kOe respectively.

Both in plane loops in figure 8.7 shows a drop in magnetization upon entry into the 2nd quadrant. X-ray trace of this high ${}_iH_c$ sample is shown in figure 8.8. Although the x-ray trace clearly identifies the most intense lines of the hard 5-17 phase, any presence of a second phase is hard to detect due to the poor quality of the trace and the high line density of 5-17 phase itself. The second phases that could be present are $Sm(Fe,T)_2$, $Sm(Fe,T)_3$ and $Sm_2(Fe,T)_{17}$, whose Curie temperature's are 402 °C, 377 °C and 112 °C respectively. Figure 8.9 shows the thermomagnetic data of the high ${}_iH_c$ sample. The variation of magnetization with temperature is fairly smooth except for the drop near 100 °C and it reaches zero near 320 °C. Presence of 1-2, 1-3 and α-Fe as second phases could be ruled out because the magnetization drops to zero near 320 °C and all these three phases have T_c's greater than 320 °C. Non zero value for magnetization should result at 320 °C if there is any of these three phases present as a second phase. In plane hysteresis loops of the same sample, room temperature and above, are shown in figure 8.10 and conditions under which each curve was measured are as follows, curve (a) as measured at room temperature before heating the sample to 320 °C, curve (b) as measured at room temperature after cooling the sample, which had been heated above 320 °C, to room temperature, curve (c) as measured at 270 °C while heating the sample and curve (d) as measured at 320 °C, T_c. Curves (a) and (b) are similar, which indicates that there is no contamination or decomposition of the sample during high temperature magnetometer measurement. Curve (c) shows no drop in magnetization upon entry into the second quadrant conforming that the only second phase present is $Sm_2(Fe,T)_{17}$ whose T_c is less than 270 °C. The magnetization loop measured at curie temperature, curve (d), shows a paramagnetic behavior indicating that decomposition or contamination of the sample at this temperature resulting in precipitation of α-Fe has not been occurred. Hence the shoulders on the demagnetization curves in the second quadrant of the, high ${}_iH_c$, Sm-Fe-Ti-V sample is a direct result of the second phase $Sm_2(Fe,T)_{17}$.

The 5-17 hard phase has also been synthesized in Sm-Fe-V film samples by a similar process, that were used to synthesis high coercivity Sm-Fe-T, T=Ti or Ti+V, film samples. In this similar method, these high coercivity Sm-Fe-V samples were first deposited in a microcrystalline amorphous state and then subsequently crystallized. Figure 8.11 shows a hysteresis loop for a $Sm_{20}Fe_{73}V_7$ sample as measured at 293 K. The hysteresis loop shown was measured in plane and parallel to a field H_s which was applied in the film plane during the deposition and subsequent crystallization. The intrinsic coercivity, ${}_iH_c$, 4πM at 90 kOe applied field, and remanent magnetization, B_r, as a function of temperature is shown in figure 8.12. The ${}_iH_c$ rises smoothly from 15.1 kOe to 31 kOe at 6K. The maximum 4πM at 90 kOe and the B_r both rise smoothly with decreasing temperature. This indicates that the high ${}_iH_c$ phase remains uniaxial to low temperatures. The synthesis method used usually introduces very little preferred texturing for the films. The observed B_r values are thus expected to be 0.5 of the saturation magnetization as for a collection of random single domain uniaxial particles. The magnetization at 90 kOe extended to $2B_r$ can be used to estimate the anisotropy field at 293 K as H_A=150 kOe.

The x-ray pattern for the Sm-Fe-V sample of fig. 11 is shown in figure 8.13(a) and for comparison the x-ray pattern of nearly single phase $Sm_{21.5}Fe_{69.1}Ti_{4.7}V_{4.7}$ sample is shown in figure 8.13(b). The x-ray pattern of Sm-Fe-V sample, figure 8.13(a), clearly shows the presence of a second phase besides the hard magnetic 5−17 phase when compared with nearly single phase x-ray pattern, figure 8.13(b). The second phase present here is $ThMn_{12}$ type $Sm(Fe,V)_{12}$ which could be easily identified and stars in figure 8.13(a) indicate the 2θ angle positions of $Sm(Fe,T)_{12}$ powder pattern with relative line intensities greater than 10%.

Unlike in hard magnetic Sm−Fe−T, T=Ti or Ti+V, films the second phase present in hard magnetic Sm−Fe−V films is not magnetically soft. Hence the drop in magnetization upon entry into the second quadrant depends on the intrinsic coercivity of the second phase and the magnetic coupling between 5−17 and 1−12 grains. In mechanically alloyed $Sm_{28}Fe_{62}Ti_{10}$ samples, ${}_iH_c$=60 kOe, the 5−17 grains are completely surrounded by a nonmagnetic SmO-phase and therefore this microstructure is close to an ideal one with noninteracting single domain particle grains(55). One could expect a similar microstructure for hard magnetic Sm−Fe−V films and therefore all the grains are completely surrounded by a nonmagnetic SmO phase which leads to very small magnetic coupling between 5−17:5−17, 1−12:1−12, and 5−17:1−12 grains. As a result of this both 5−17 and 1−12 phases have high coercivities and the hysteresis loop looks like a multilayer film with two layers having different coercivities. Hysteresis loops of the same $Sm_{20}Fe_{73}V_7$ film (a) at 293 K, (b) at 160 K, and (c) at 5 K are shown in figure 8.14. The drop in second quadrant at 293 K and 160 K are barely visible but at 5 K it is clearly visible. The reason for this could be that both $Sm_5(Fe,V)_{17}$ and $Sm(Fe,V)_{12}$ have comparable ${}_iH_c$ values and they have the same temperature dependence except at very low temperatures where the 5−17 phase has very strong temperature dependence.

Figure 8.15 shows the low field hysteresis loops of the same $Sm_{20}Fe_{73}V_7$ sample, solid curve, and a sample deficient in Sm, $Sm_{12.8}Fe_{81.0}V_{6.2}$, dashed curve. Although both loops are minor, shoulder on the demagnetization curve in the second quadrant is very large in the dashed curve which belongs to the Sm deficient sample. X-ray diffraction patterns of these two samples are shown in figure 8.16(a) and (b) respectively. Both x-ray traces show the presence of no other phases but 5-17, major phase and 1-12, minor phase. Although we labeled 1-12 as a minor phase in Sm deficient sample, amount of 1-12 phase in this sample is comparable to 5-17 phase. The large second quadrant drop and hence low coercivity in the hysteresis loop of Sm deficient sample could be due to the lack of a SmO-grain boundary phase, which isolate both 1-12 and 5-17 grains as in $Sm_{20}Fe_{73}V_7$ sample explained in the preceding paragraph. Absence of a grain boundary phase lead to magnetic coupling between neighboring grains. Therefore the 1-12 grains can no longer be considered as noninteracting single domain grains like in the other sample which results in not only a low coercivity 1-12 phase but also a low coercivity 5-17 phase, through the magnetic coupling between 1-12 and 5-17 grains. Hence the drop in magnetizaton upon entry into the second quadrant is very large in the Sm deficient $Sm_{12.8}Fe_{81.0}V_{6.2}$ sample.

Although the above explanations based on microstructure agree with the observed results, microstructure studies of Sm-Fe-V samples has not been done other than grain size measurements by using SEM. Extensive microstructure studies of mechanically alloyed, 5-17, Sm-Fe-Ti samples described in ref. 55 were useful in above explanations.

In ref. 19 Stadelmaier et al. reached the conclusion that the Ti in the high coercive force Sm-Fe-Ti must be in grain boundary phases, and not to any significant extent incorporated into the main phase. Experimental changes in the lattice parameters and unit cell volume for binary Sm_5Fe_{17}, and for changes in the third element from T=V to Ti are shown in table 8.2. The indexing in each case was done using only the indicated powder pattern lines from ref. 19. The hexagonal unit cell volume shows a clear and systematic expansion upon the partial replacement of Fe with V, V-Ti, and Ti. It was estimated in ref. 19 that if 10% of the Fe were replaced by Ti, that this would lead to about a 2% volume expansion of the unit cell. This estimate was based on differences in the atomic radii of Fe(0.126 nm) and Ti(0.147 nm).

The fact that we have been able to synthesize binary Sm_5Fe_{17} provides a base line for the volume expansions. Experimentally it was observed that a 10% replacement of V for Fe caused a 0.83% volume expansion, and that an 11% replacement of Ti for Fe caused a 1.67% volume expansion. The fact that these additions are accompanied by a systematic volume expansion of the expected size shows that the Ti and V are actually acting as replacement elements for Fe in the primary magnetic phase.

In figure 8.17 an in plane hysteresis loop for a subsequently crystallized $Sm_{19.9}Fe_{72}Zr_{8.1}$ film is shown as measured at 293 K. This similarly processed Sm-Fe-Zr film exhibits very different magnetic properties and crystal structure from the Sm-Fe-T, T=Ti, V, Ti+V, films. The room temperature coercivity was 6.7 kOe and B_r=4 kG, and $4\pi M$ @ 18 kOe=6 kG. An extrapolated anisotropy field when $4\pi M$ goes to $2B_r$ of 36 kOe is thus indicated. The x-ray diffractometer trace of the same $Sm_{19.9}Fe_{72}Zr_{8.1}$ sample is shown in figure 8.18 and can be indexed for the 7 lines at 35.14, 41.32, 41.71, 44.35, 61.88, 62.95, 67.51, and 74.17 degrees for $Cu_{K\alpha 1}$ as a $TbCu_7$ structure with a=5.109 A and c=4.074 A. The root mean square fitting tolerance is 0.013 degrees. The x-ray pattern is remarkably simple as expected for the small cell disordered 1-5 structure.

CHAPTER 9 CONCLUSIONS

A systematic study of the deposition process control and magnetic properties of $ThMn_{12}$ type R-Fe-T family was carried out. Study of magnetic properties of nitrided film samples of this family exhibited that Nd-Fe-Mo poses very good magnetic properties and these properties could be enhanced greatly by replacing part of Mo by Co.

It was found that texture mode of the sputter synthesized films could be varied by controlling sputter deposition parameters, such as sputtering gas pressure, deposition rate, and substrate temperature. These parameters affect adatom surface mobility on the growing film surface, which greatly influence the texture mode. The adatom surface mobility was lowered by high deposition rates and high sputtering gas pressures where as increased by high substrate temperatures. Hence effects of deposition rate and sputtering gas pressure could be counter balanced by substrate temperature and still get the desired texture mode. Films were made with the easy c-axis highly aligned perpendicular to the film plane exhibiting perpendicular to the film plane square shape loops with remanent magnetization values close to the saturation values. For highly (002) textured films $4\pi M_r/4\pi M_s$ ratio was ≈ 0.99.

In $ThMn_{12}$ type R-Fe-T family $Sm(Fe,T)_{12}$ is a good candidate for permanent magnet applications and for a $Sm_{8.04}Fe_{79.16}Ti_{9.11}V_{3.69}$ film sample the $4\pi M_s$ value was 12.1 kG and perpendicular to the film plane maximum energy product was 20.7 MGOe. The intrinsic coercivity ${}_iH_c$ in this sample was 5 kOe. This energy product value is the highest value reported for a $ThMn_{12}$ type unnitrided $R(Fe,T)_{12}$ sample. Extreme alignment of the easy c-axis perpendicular to the film plane allowed the determination of anisotropy field, H_A, by extrapolating the inplane and perpendicular to the film plane hysteresis loops.

Sm-Fe-Ti films were synthesized for the first time with the non magnetic third element concentrations as low as 1 at. % contradicting a common belief that large amount of non magnetic third element concentrations were necessary to stabilize the $ThMn_{12}$ phase. Synthesization of binary $SmFe_{12}$ was reported by our group recently.

Magneto optical and Mössbauer studies were carried out for $Sm(Fe,Ti)_{12}$ samples to explore them further. Magnetometer measurements exhibited that the average grain size was smaller in (222) textured films than (002) textured films. But it was found, in optical measurements, that the difference in grain size was greater at the surface layers than in the bulk of the film sample. Magneto optical measurements also revealed that the rate of change of grain size as the film grow in thickness was very high for (222) textured films when compared with that of (002) textured films. The polar Kerr rotation observed for $Sm(Fe,Ti)_{12}$ films was similar to that observed for pure Fe over the photon energy range from 1.25 to 2.45 ev. For practical purposes these highly textured crystalline films acted as Fe films, but with a much higher and variable coercivity.

Nitriding of soft $Nd(Fe,T)_{12}$, T=Ti or Mo, drastically changed the magnetic properties, giving rise to hard magnetic properties. The intrinsic magnetic properties of nitrided $Nd(Fe,T)_{12}$, T=Ti or Mo, film samples surpassed the best values observed in the unnitrided R-Fe-T family. It was found that $Nd(Fe,Mo)_{12}$ was the most promising in film synthesized samples since highly aligned α-Fe free samples could be made. The highest coercivity, ${}_{i}H_{c}$, value observed in $Nd(Fe,T)_{12}$, T=Ti or Mo, samples was 7.2 kOe for a $Nd(Fe,Mo)_{12}$ sample with some excess Nd. The maximum energy product for this sample was 30.2 MGOe.

It was found that remanent flux density of $Nd(Fe,Mo)_{12}$ samples could be enhanced by replacing some of the Mo by Co. A film sample made with 50% of Mo replaced by Co showed perpendicular to the film plane energy product of 46.3 MGOe. This value was the highest energy product value reported for a $ThMn_{12}$ type R-Fe-T sample. The room temperature ${}_{i}H_{c}$ and $4\pi M_s$ values were 8.7 kOe and 15.5 kG respectively. The highest room temperature coercivity observed in Co substituted samples was 11.3 kOe for $Nd_{8.9}Fe_{80.3}Co_{6.0}Mo_{4.8}N_x$ and this ${}_{i}H_{c}$ value increased to 29.5 kOe by 10 K.

An interesting feature was observed in disordered $TbCu_7$ type $Sm(Fe,Ti)_7$ and $Nd(Fe,Ti)_7$ films after nitriding. Both are conical systems and the cone angle decreased in the former and increased in the latter upon nitriding.

The characteristic drop in magnetization upon entry into the second quadrant associated with hard 5-17 type Sm-Fe-T films was found to be due to second phases. Since these films were synthesized by subsequent crystallization, richness of the Sm matrix and the amount of non magnetic third element present in the amorphous film deposit influenced the type and amount of second phases. Second phases observed in hard magnetic 5-17 type Sm-Fe-T films were soft magnetic except in the case of Sm-Fe-V, where the second phase was hard magnetic $ThMn_{12}$ type $Sm(Fe,V)_{12}$. In high coercivity 5-17 type Sm-Fe-V films, it was found that magnetic coupling between hard magnetic 5-17 type Sm-Fe-V grains and 1-12 type second phase Sm-Fe-V grains was greatly affected by a possible grain boundary SmO phase.

Table 4.1

2θ (deg.)	h k l
30.07	2 1 1
37.52	0 0 2
43.25	2 0 2
48.46	2 2 2
51.06	3 1 2
62.39	4 2 2
62.98	2 1 3
67.26	3 0 3
71.13	3 2 3
79.95	0 0 4

Table 4.2

h k l	d (A)	Intensity
1 0 1	4.185	4
2 2 0	3.030	8
2 1 1	2.994	39
3 1 0	2.710	12
3 0 1	2.454	36
0 0 2	2.398	14
4 0 0	2.143	51
3 2 1	2.130	100
2 0 2	2.093	83
3 3 0	2.020	8
4 2 0	1.916	14
2 2 2	1.880	25
3 1 2	1.796	5
5 1 0	1.681	3
4 3 1	1.614	5
3 3 2	1.545	5
4 4 0	1.514	5
5 2 1	1.510	8
4 2 2	1.497	7
5 3 0	1.470	8

Table 4.3

2θ	Hex. 1-5			Rhombo. 2-17			Tetrag. 1-12		
	h	k	l	h	k	l	h	k	l
30.10	1	0	1	1	1	3	2	1	1
37.33	1	1	0	3	0	0	0	0	2
43.30	2	0	0	2	2	0	2	0	2
48.58	2	0	1	2	2	3	2	2	2
51.13							3	1	2
60.34							3	3	2
62.56	2	0	2	2	2	6	4	2	2
63.01							2	1	3
67.21	3	0	0	3	3	0	3	0	3
71.29	3	0	1	3	3	3	3	2	3
	a=4.821 A c=4.218 A F_{min}=0.01°			a=8.351 A c=12.652 A F_{min}=0.01°			a=8.438 A c=4.805 A F_{min}=0.01°		

Table 6.1

Transition		δm	Angular Dependence of Line Intensities	Line Intensitis		
				Random	$\Theta=0$	$\Theta=\pi/2$
±3/2	±1/2	±1	$(3/4)(1+\text{Cos}^2\Theta)$	3	3	3
±1/2	±1/2	±0	$\text{Sin}^2\Theta$	2	0	4
±3/2	±1/2	±1	$(1/4)(1+\text{Cos}^2\Theta)$	1	1	1

Θ – Angle between the γ ray propagation direction and hyperfine field

Table 6.2

Site	8i	8j	8f	2a
8i	2.390(1) 2.920(4)	2.664(2) 2.661(2)	2.636(4)	3.104(1)
8j	2.664(2) 2.661(2)	2.711(2)	2.468(4)	3.058(2)
8f	2.636(4)	2.468(4)	2.382(2)	3.265(2)

The interatomic distances are given in A and the number of adjacent atoms for each site are given in brackets.

Table 7.1

	$NdFe_{11}MoN_x$	$Nd^+Fe_{11}MoN_x$	$NdFe_{11}Mo_{0.5}Co_{0.5}N_x$
$4\pi M_s$(kG)	2.9	12.8	15.5
$_iH_c$(kOe)	5.3	7.2	8.7
H_A(kOe)	130	130	150
BH_{max}(MGOe)	24.4	30.2	46.3
I(002)counts	55478	30998	39477
I(α-Fe)/I(002)	0	0.0072	0
I(Nd)/I(002)	0	0.044	0
I(202)/I(002)	0.0035	0.0018	0.0071
I(222)/I(002)	0	0	0
I(420)/I(002)	0	0.027	0

Table 8.1

Angle $(2\theta)_{exp.}$	Half width (w)	Height (y_0)	Area (I)	I/I_0	h k l
24.46	0.2211	24.0	5168	9	4 1 1
25.01	0.1450	24.7	3489	6	4 0 2
26.54	0.1350	95.8	12617	23	3 2 2 3 0 0
27.51	0.1632	42.4	6753	12	3 3 1
28.00	0.1213	89.0	10528	19	2 2 3 4 2 1
28.90	0.1004	22.79	2232	4	0 0 4
29.40	0.1420	139.3	19290	35	1 0 4
30.29	0.1347	170.0	22341	40	3 3 2
30.75	0.1108	40.36	4365	8	6 0 0
31.17	0.1327	69.9	9052	16	3 2 3
32.03	0.1339	92.8	12130	22	2 1 4
33.64	0.1352	40.05	5285	10	6 1 0
34.13	0.1930	163.1	30681	55	2 2 4
34.47	0.1363	417.1	55478	100	3 1 4
35.25	0.1100	94.0	10082	18	5 2 2
35.63	0.1540	79.05	11873	21	4 0 4
36.04	0.1414	73.18	10094	18	5 3 0
36.79	0.1449	132.6	18750	34	5 3 1
37.52	0.1681	34.92	5727	10	4 1 4
37.87	0.0996	41.18	4007	7	6 2 1
38.24	0.1603	100.2	15675	28	4 3 3
38.96	0.1515	72.04	10651	19	5 0 4 5 2 3

Continue...

Continued from the previous page

39.66	0.1158	94.0	10620	19	3 3 4 7 1 1
40.02	0.2032	142.0	28125	51	4 2 4 6 2 2
40.39	0.1795	278.0	48666	88	6 1 3
41.03	0.0946	42.3	3906	7	5 4 1
41.39	0.1892	102.0	18816	34	8 0 0
41.74	0.1760	70.1	12037	22	7 1 2 6 3 1
42.41	0.1666	196.5	31929	58	5 3 3 7 2 0
43.06	0.1842	203.8	36598	66	3 2 5
43.74	0.2625	108.2	27639	50	4 1 5 5 2 4
44.27	0.2183	36.27	7712	14	1 0 6
45.59	0.1896	46	8508	15	3 3 5
46.26	0.1199	24.2	2830	5	5 4 3 7 3 0
46.85	0.1234	43.4	5230	9	6 3 3
47.79	0.1465	40.3	5764	10	2 2 6
48.14	0.1156	15.4	1738	3	7 2 3
51.59	0.0959	12.1	1129	2	5 0 6 7 3 3 8 3 0
52.41	0.0900	12.3	1082	2	4 2 6

Table 8.2

Composition	a (A)	c (A)	% Cell Expansion	$_iH_c$ at 293K (kOe)
Sm_5Fe_{17}	20.061	12.282	-------	7
$Sm_5(Fe_{0.90}V_{0.1})_{17}$	20.115	12.318	0.83%	16
$Sm_5(Fe_{0.89}V_{0.055}Ti_{0.055})_{17}$	20.142	12.336	1.25%	45
$Sm_5(Fe_{0.89}Ti_{0.11})_{17}$	20.169	12.354	1.67	39

Figure 2.1

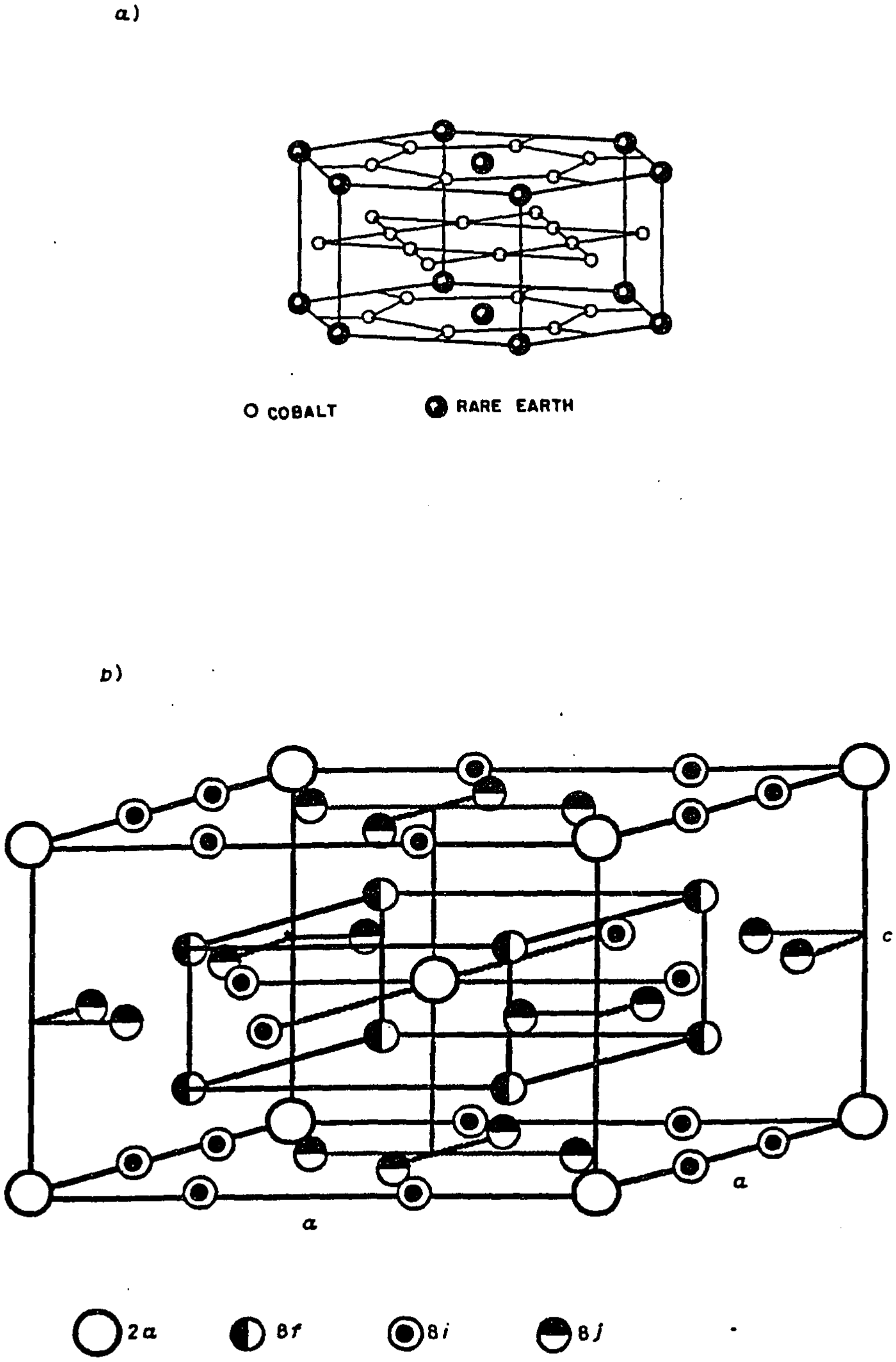

Figure 4.1

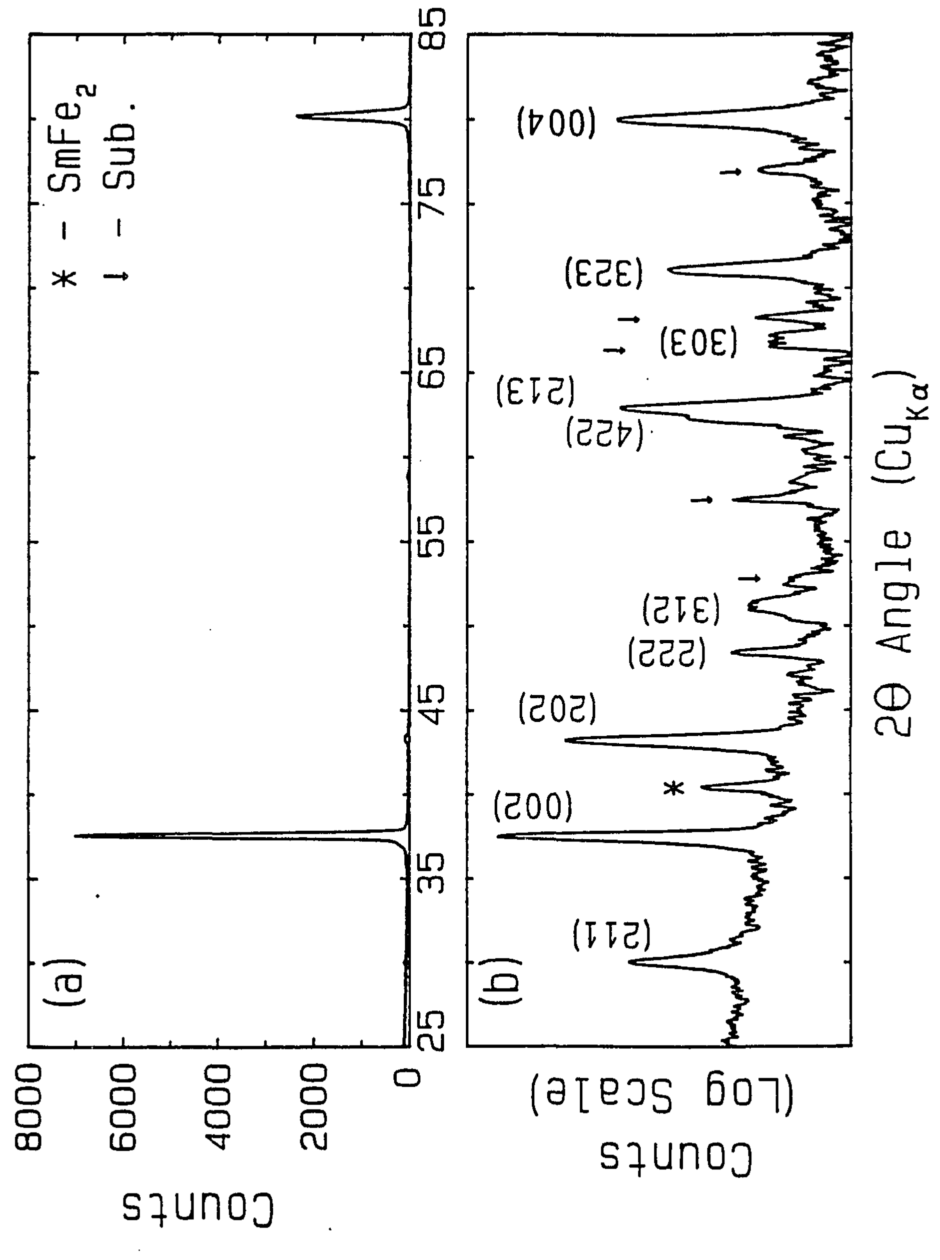
(a)
(b)
* - SmFe$_2$
↓ - Sub.
Counts
8000
6000
4000
2000
0
Counts
(Log Scale)
25
35
45
55
65
75
85
(211)
(002)
*
(202)
(222)
(312)
(422)
(213)
(303)
(323)
(004)
2Θ Angle (Cu$_{K\alpha}$)

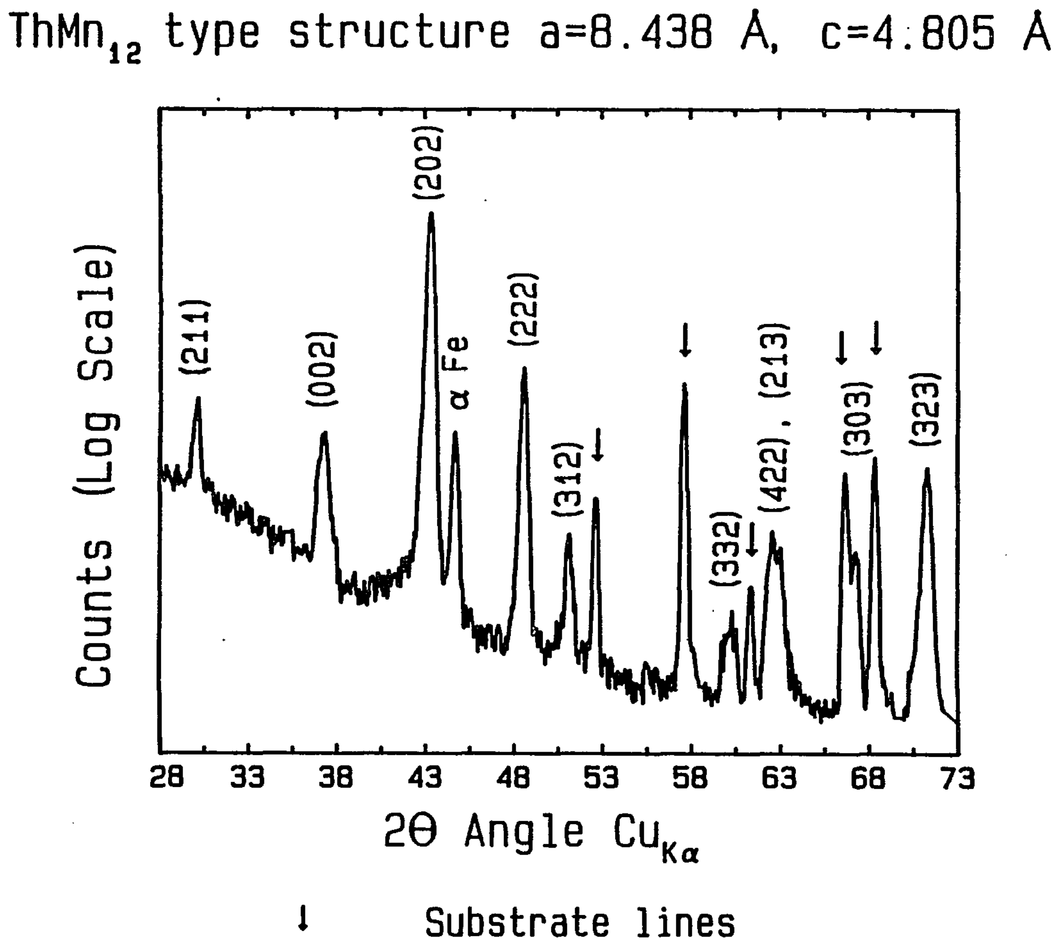
ThMn12 type structure a=8.438 Å, c=4.805 Å
Counts (Log Scale)
(211)
(002)
(202)
α Fe
(222)
(312)
(332)
(422), (213)
(303)
(323)
28
33
38
43
48
53
58
63
68
73
2Θ Angle CuKα
↓ Substrate lines

Figure 4.2

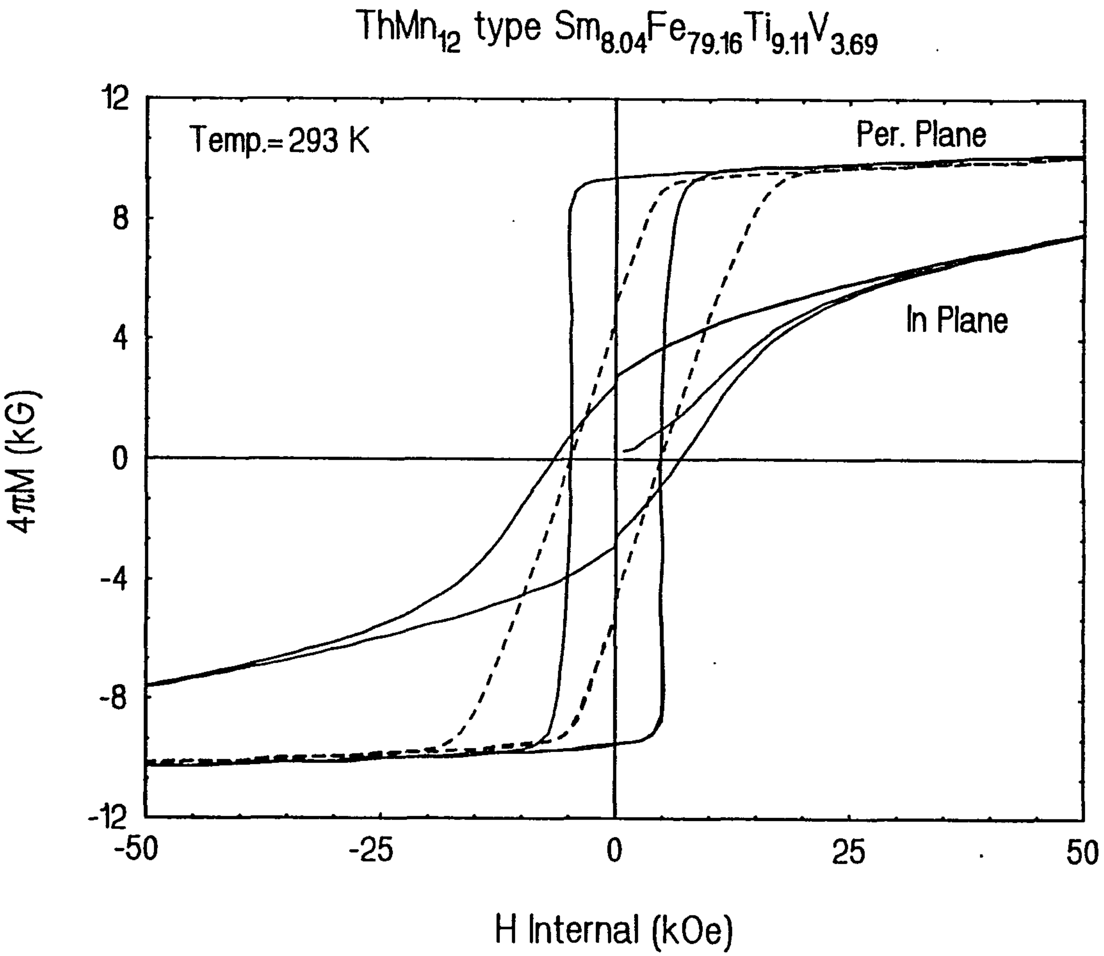
ThMn$_{12}$ type Sm$_{8.04}$Fe$_{79.16}$Ti$_{9.11}$V$_{3.69}$
Temp.= 293 K
Per. Plane
In Plane
12
8
4
0
-4
-8
-12
4πM (kG)
-50
-25
0
25
50
H Internal (kOe)

Figure 4.3

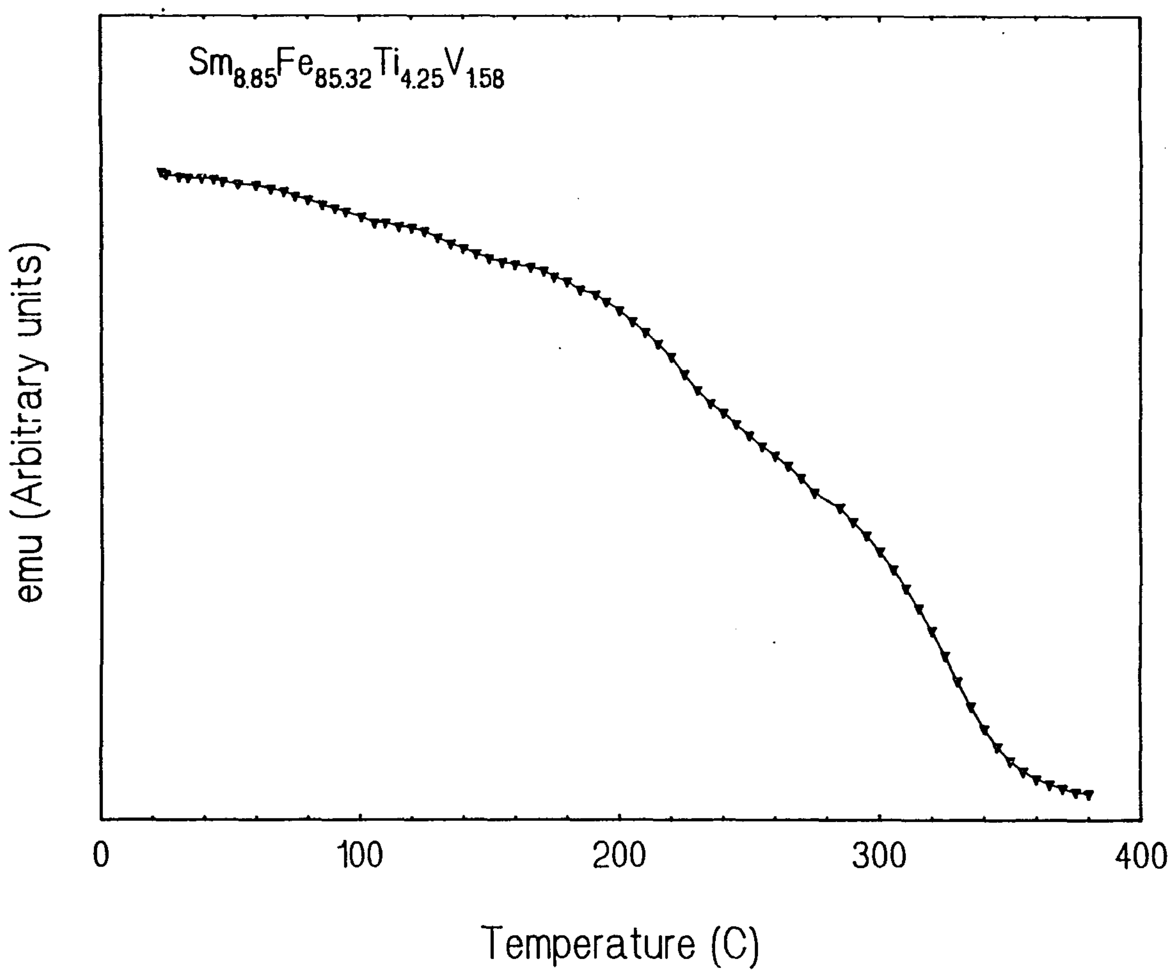
$Sm_{8.85}Fe_{85.32}Ti_{4.25}V_{1.58}$
emu (Arbitrary units)
0
100
200
300
400
Temperature (C)

Figure 4.4

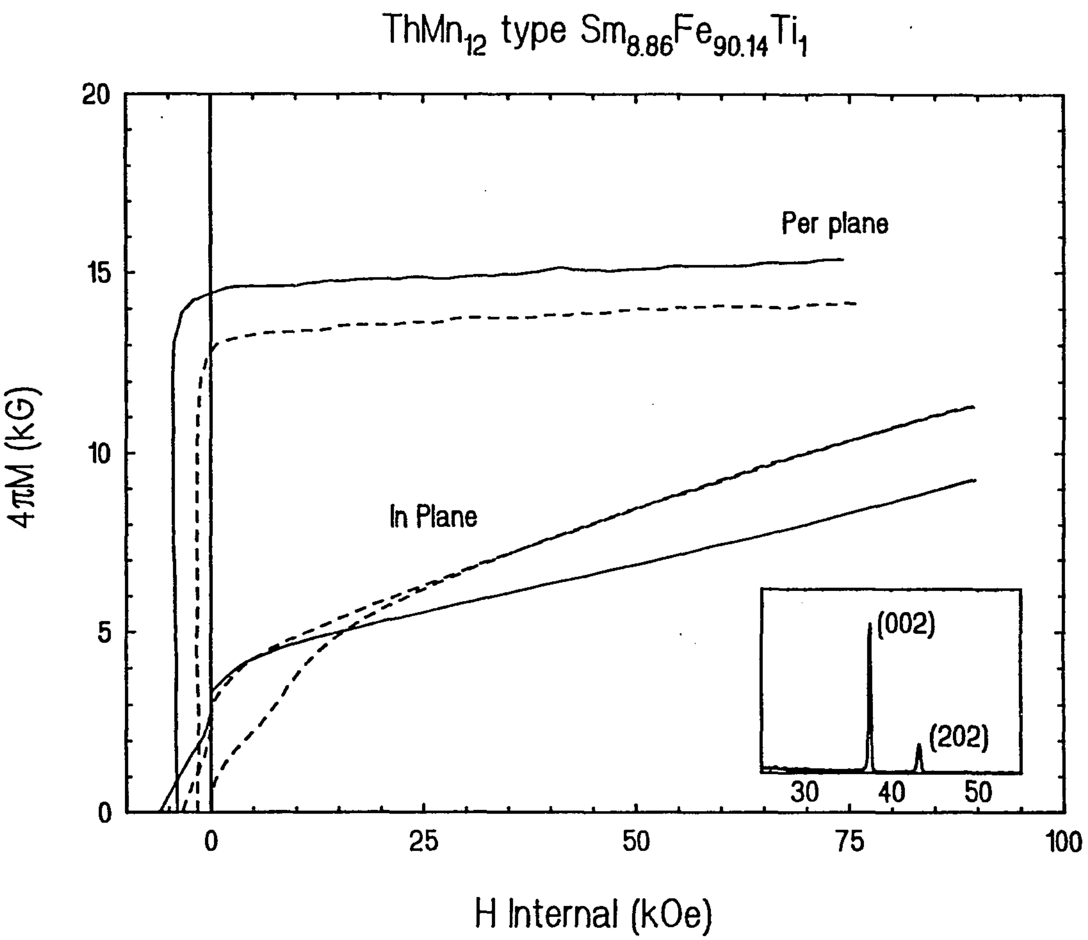
ThMn$_{12}$ type Sm$_{8.86}$Fe$_{90.14}$Ti$_{1}$
4πM (kG)
20
15
10
5
0
0
25
50
75
100
H Internal (kOe)
Per plane
In Plane
(002)
(202)
30
40
50

Figure 4.5

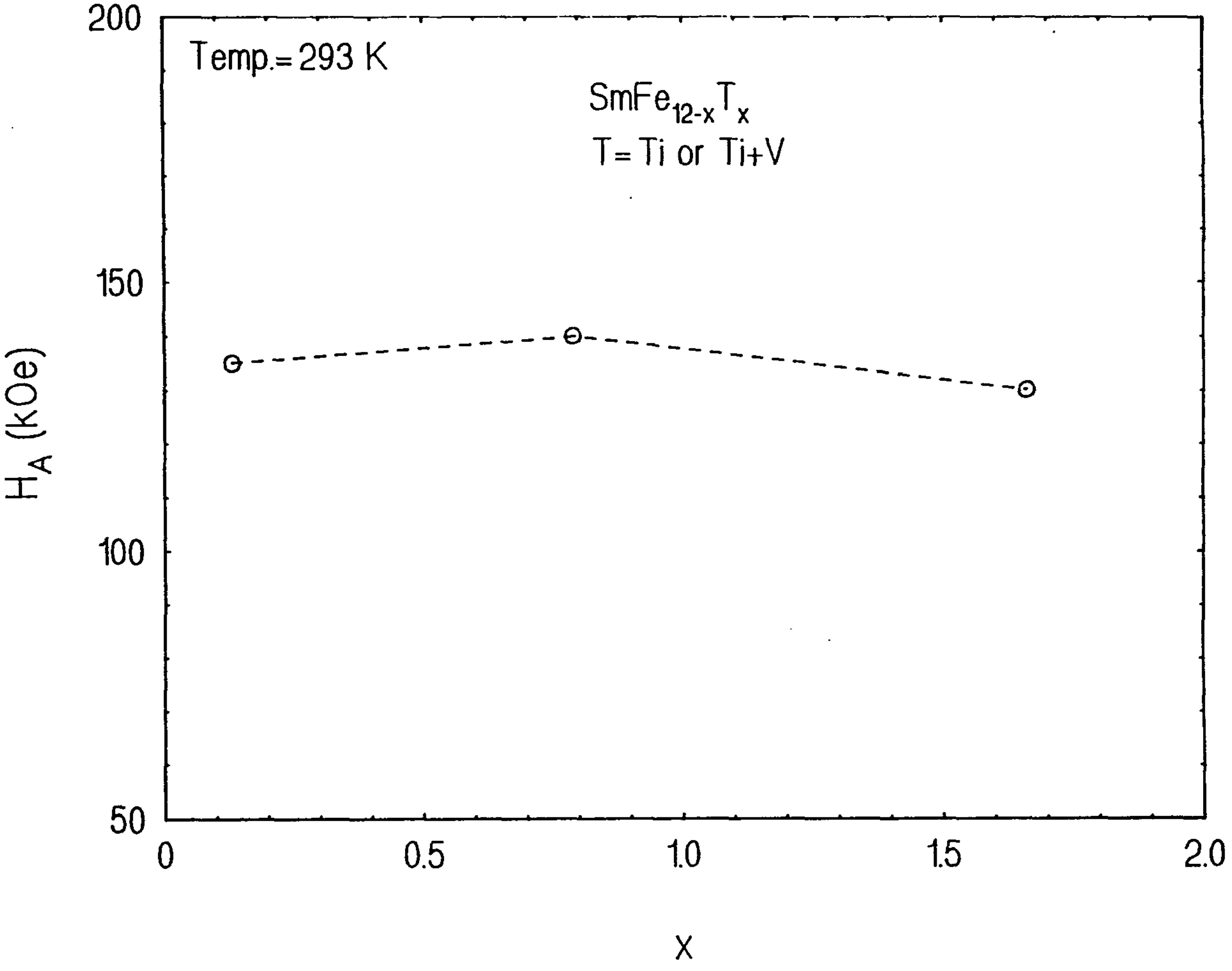

Temp.= 293 K
SmFe$_{12-x}$T$_x$
T= Ti or Ti+V
200
150
100
50
H$_A$ (kOe)
0
0.5
1.0
1.5
2.0
X

Figure 4.6

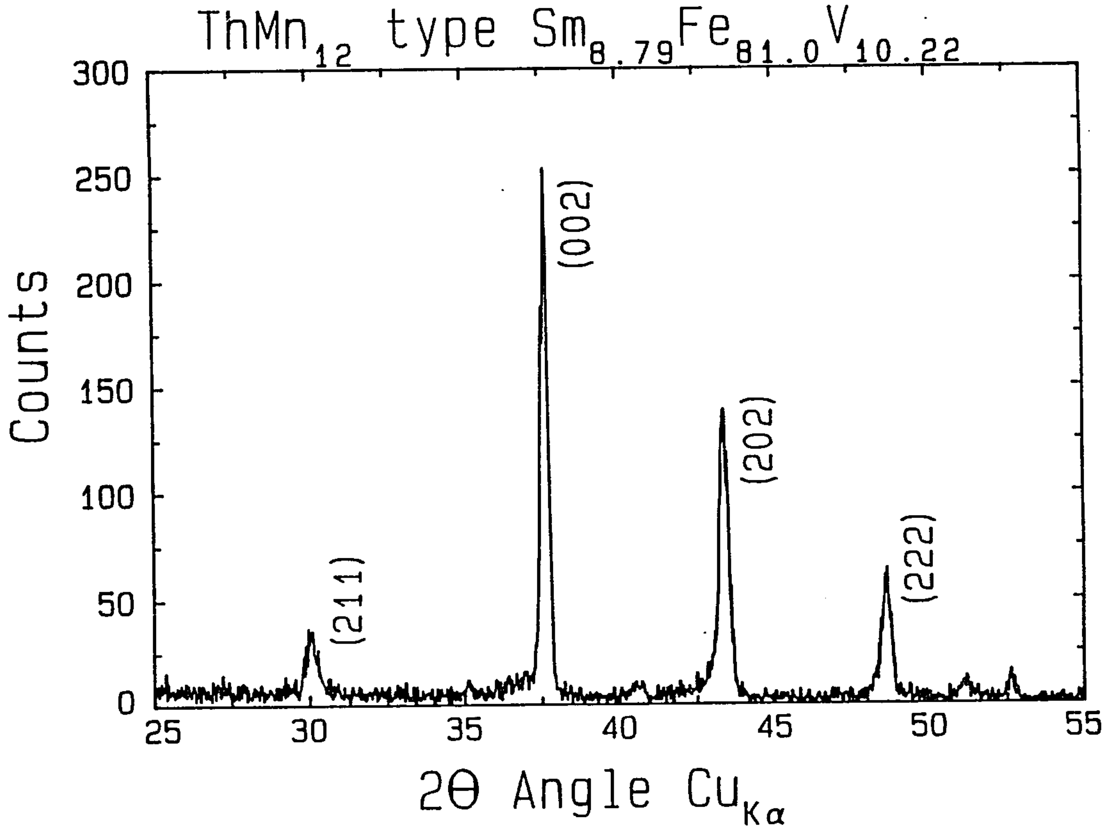
ThMn12 type Sm8.79Fe81.0V10.22
Counts
300
250
200
150
100
50
0
25
30
35
40
45
50
55
2Θ Angle CuKα
(211)
(002)
(202)
(222)

Figure 4.7

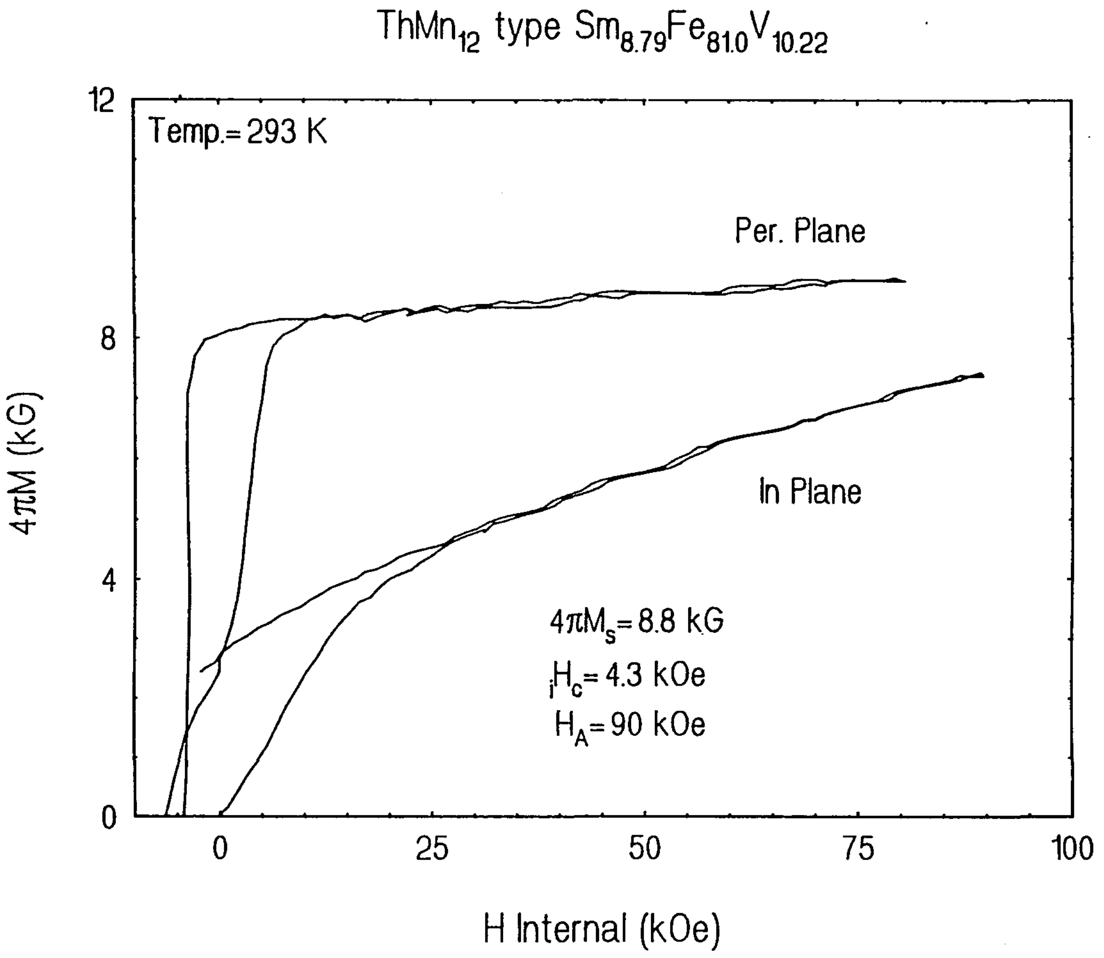

ThMn$_{12}$ type Sm$_{8.79}$Fe$_{81.0}$V$_{10.22}$
Temp.= 293 K
Per. Plane
In Plane
4πM$_s$= 8.8 kG
$_i$H$_c$= 4.3 kOe
H$_A$= 90 kOe
4πM (kG)
H Internal (kOe)
0
4
8
12
0
25
50
75
100

Figure 4.8

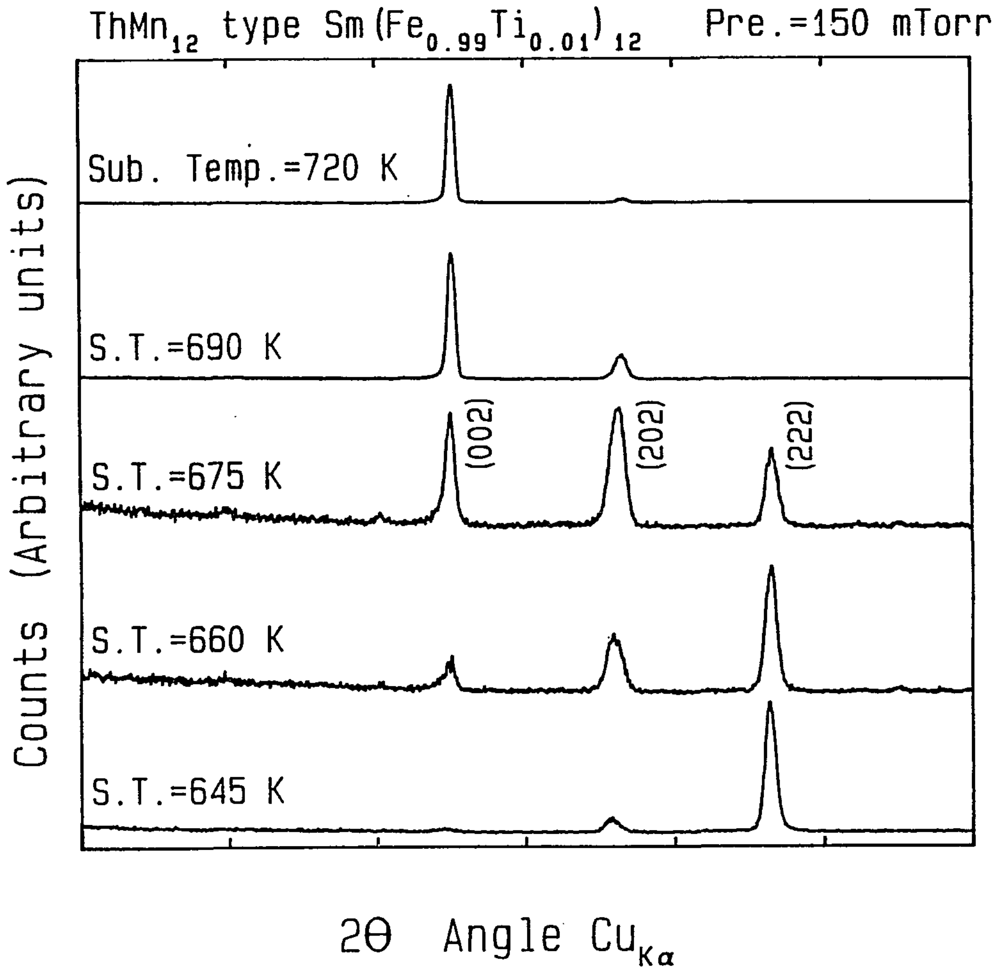
ThMn12 type Sm(Fe0.99Ti0.01)12 Pre.=150 mTorr
Sub. Temp.=720 K
S.T.=690 K
S.T.=675 K
S.T.=660 K
S.T.=645 K
(002)
(202)
(222)
Counts (Arbitrary units)
2Θ Angle CuKα

Figure 5.1

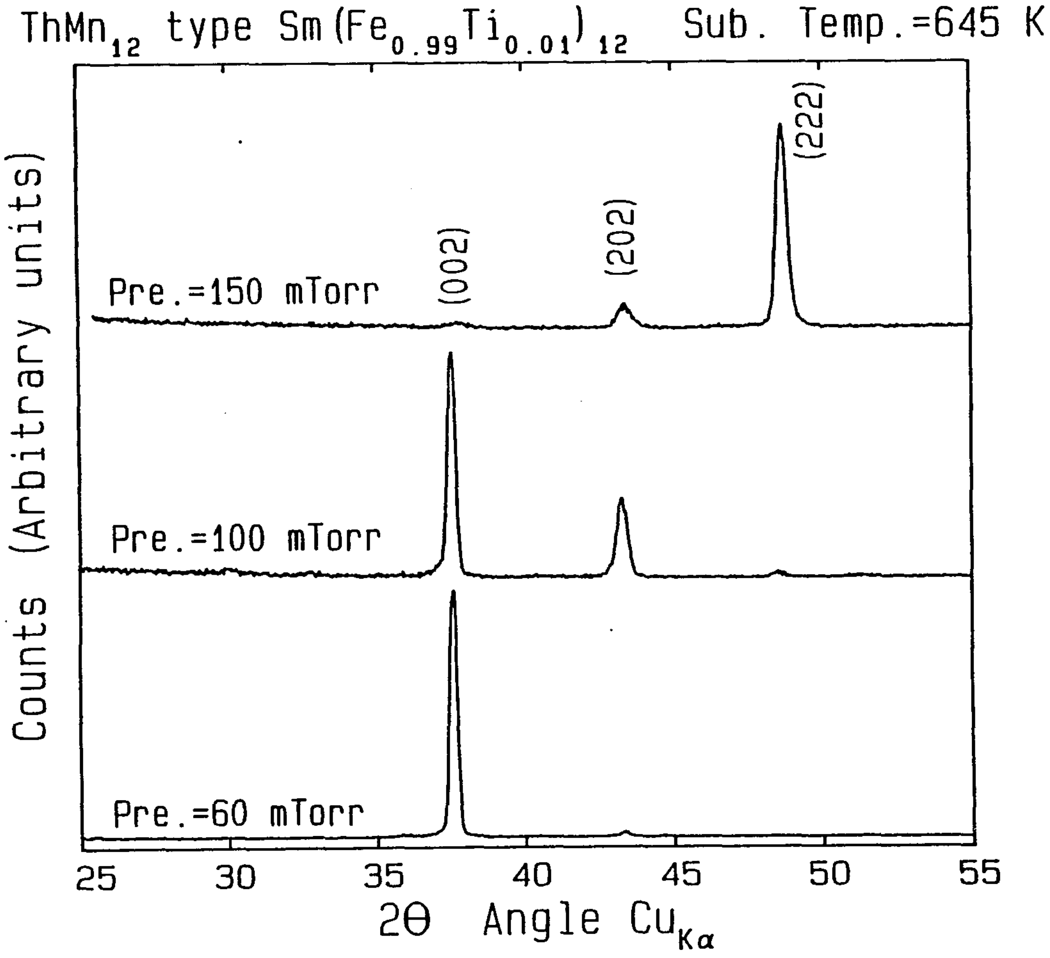
ThMn$_{12}$ type Sm(Fe$_{0.99}$Ti$_{0.01}$)$_{12}$ Sub. Temp.=645 K
Counts (Arbitrary units)
Pre.=150 mTorr
Pre.=100 mTorr
Pre.=60 mTorr
(002)
(202)
(222)
25
30
35
40
45
50
55
2Θ Angle Cu$_{K\alpha}$

Figure 5.2

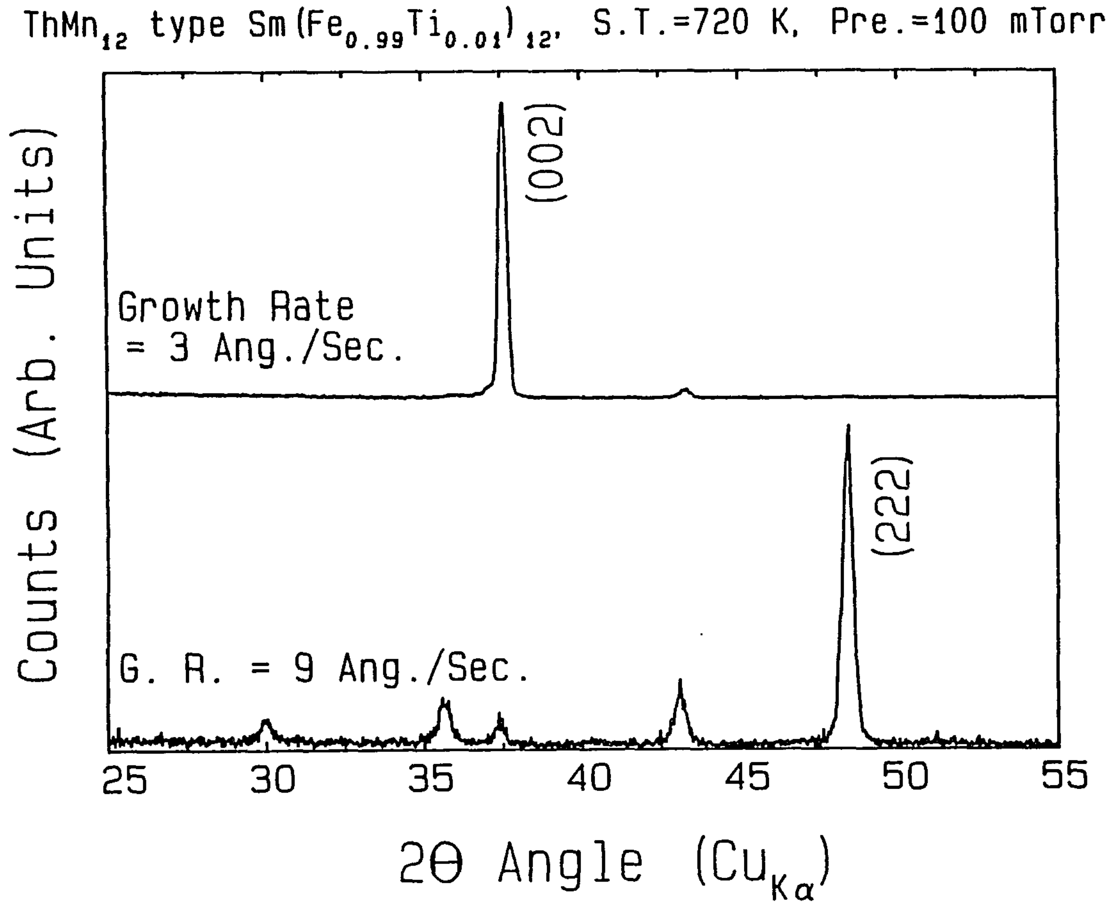

ThMn$_{12}$ type Sm(Fe$_{0.99}$Ti$_{0.01}$)$_{12}$, S.T.=720 K, Pre.=100 mTorr

Figure 5.3

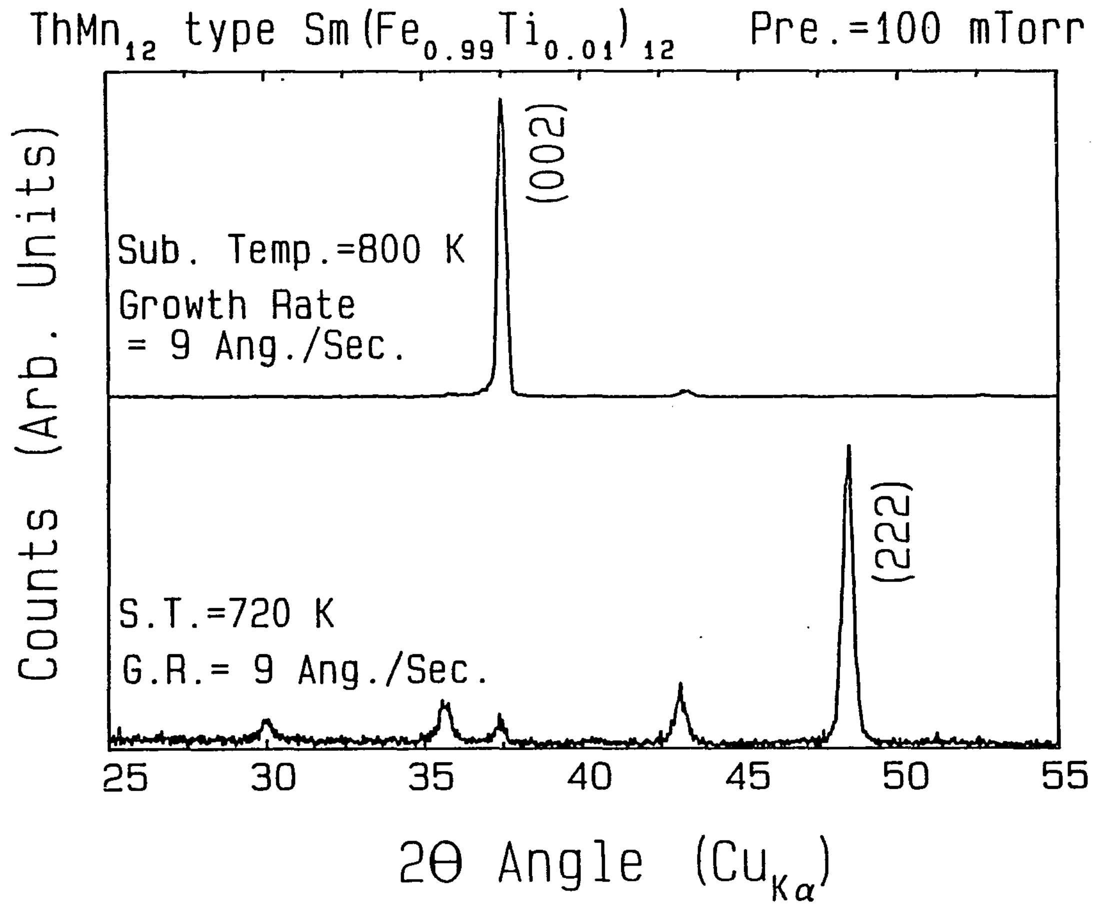
ThMn$_{12}$ type Sm(Fe$_{0.99}$Ti$_{0.01}$)$_{12}$
Pre.=100 mTorr
(002)
Sub. Temp.=800 K
Growth Rate
= 9 Ang./Sec.
(222)
S.T.=720 K
G.R.= 9 Ang./Sec.
Counts (Arb. Units)
25
30
35
40
45
50
55
2Θ Angle (Cu$_{K\alpha}$)

Figure 5.4

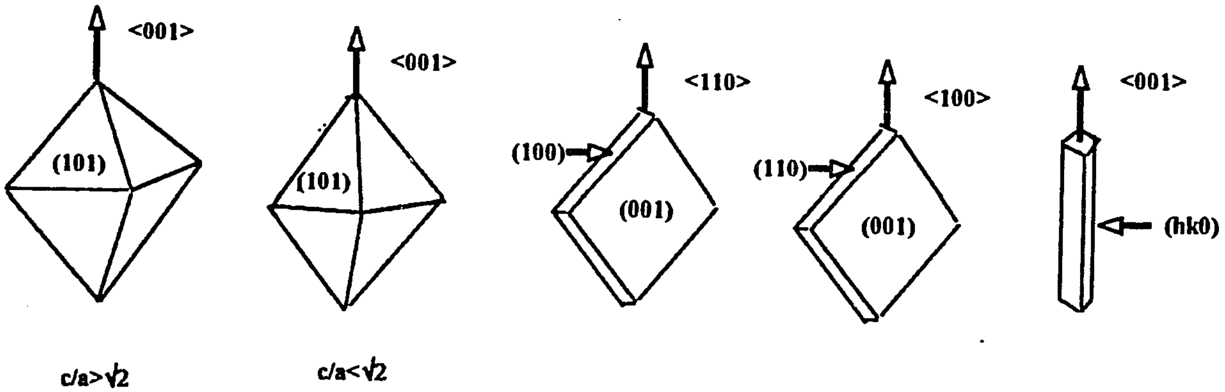

Tetragonal bipyramid

Tetragonal prisms

Basal pinacoid

Figure 5.5

Figure 5.6

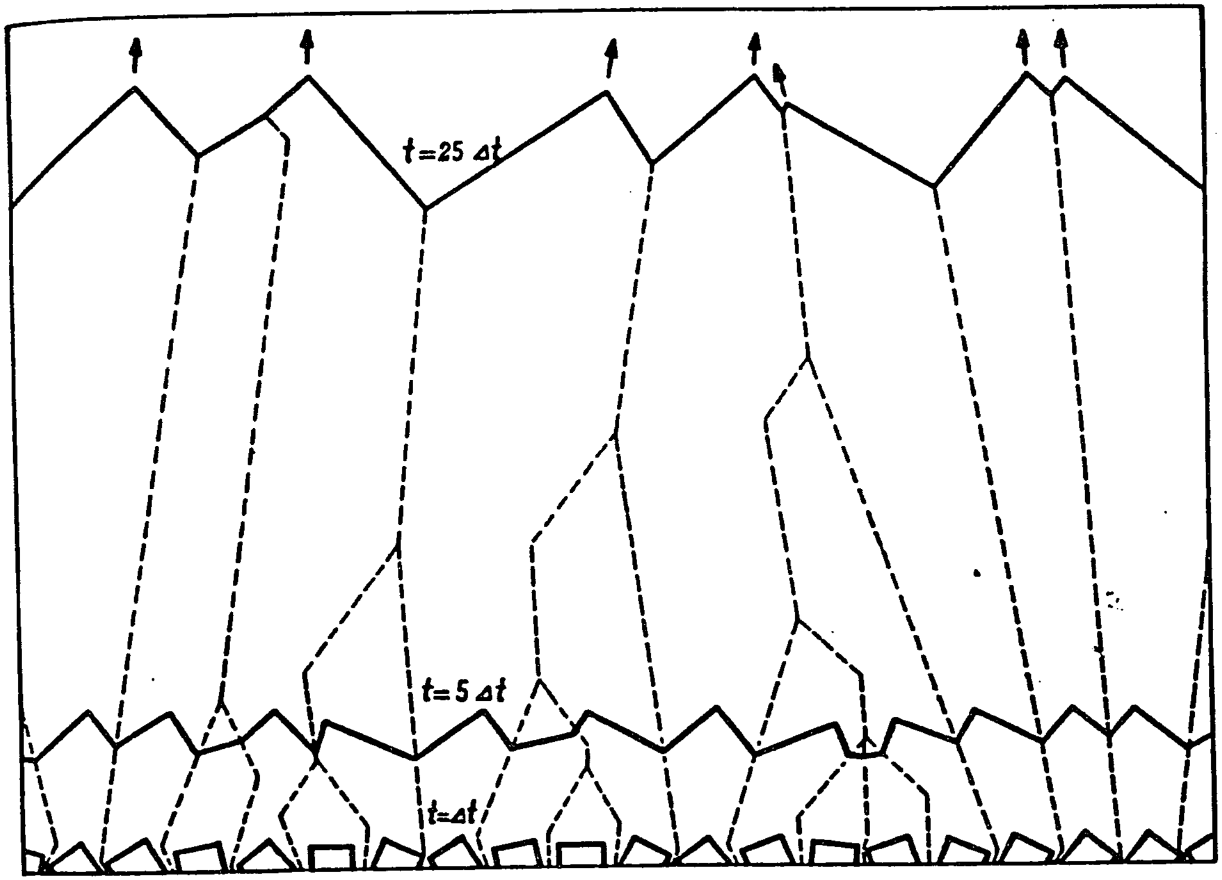

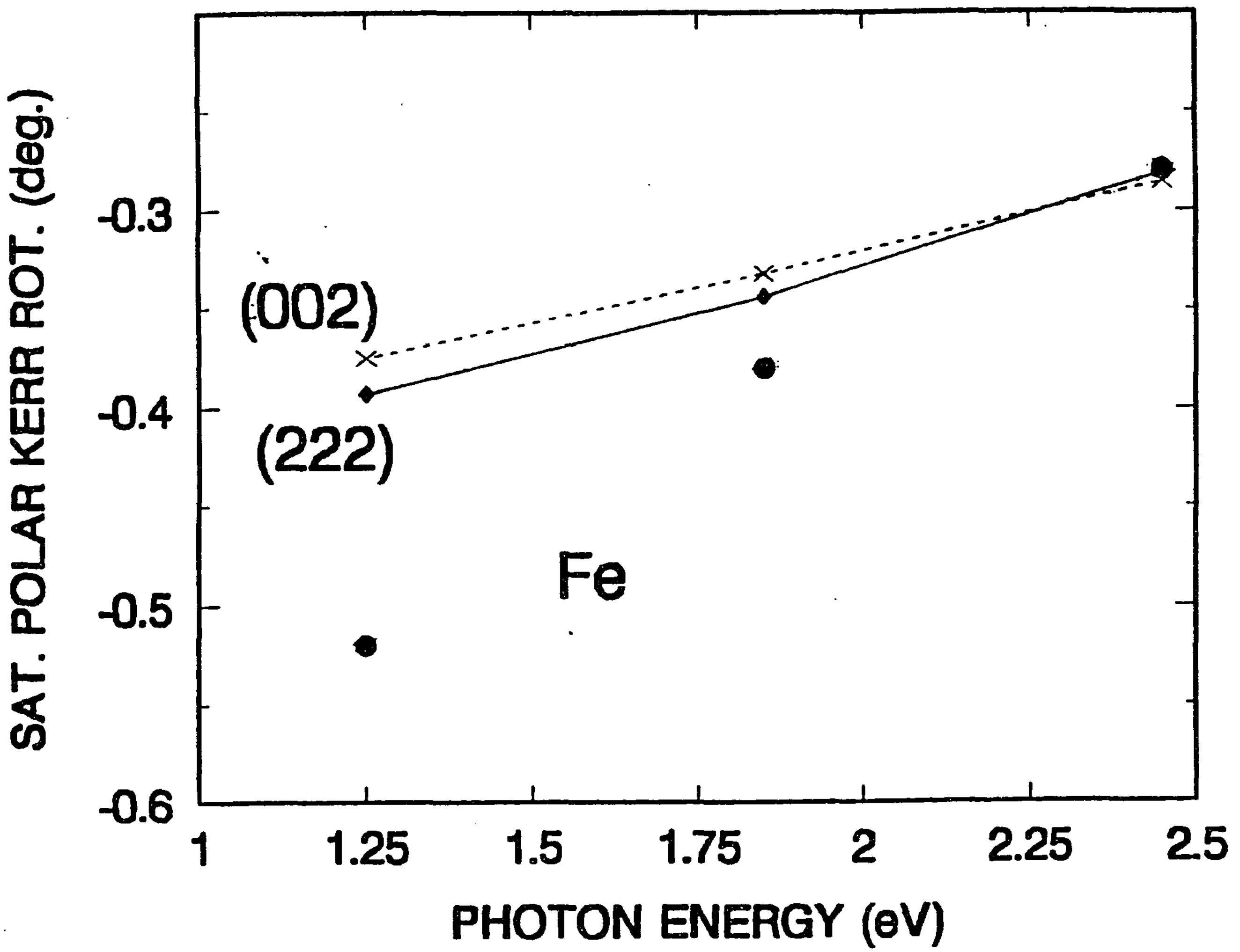
SAT. POLAR KERR ROT. (deg.)
-0.3
-0.4
-0.5
-0.6
(002)
(222)
Fe
1
1.25
1.5
1.75
2
2.25
2.5
PHOTON ENERGY (eV)

Figure 6.1

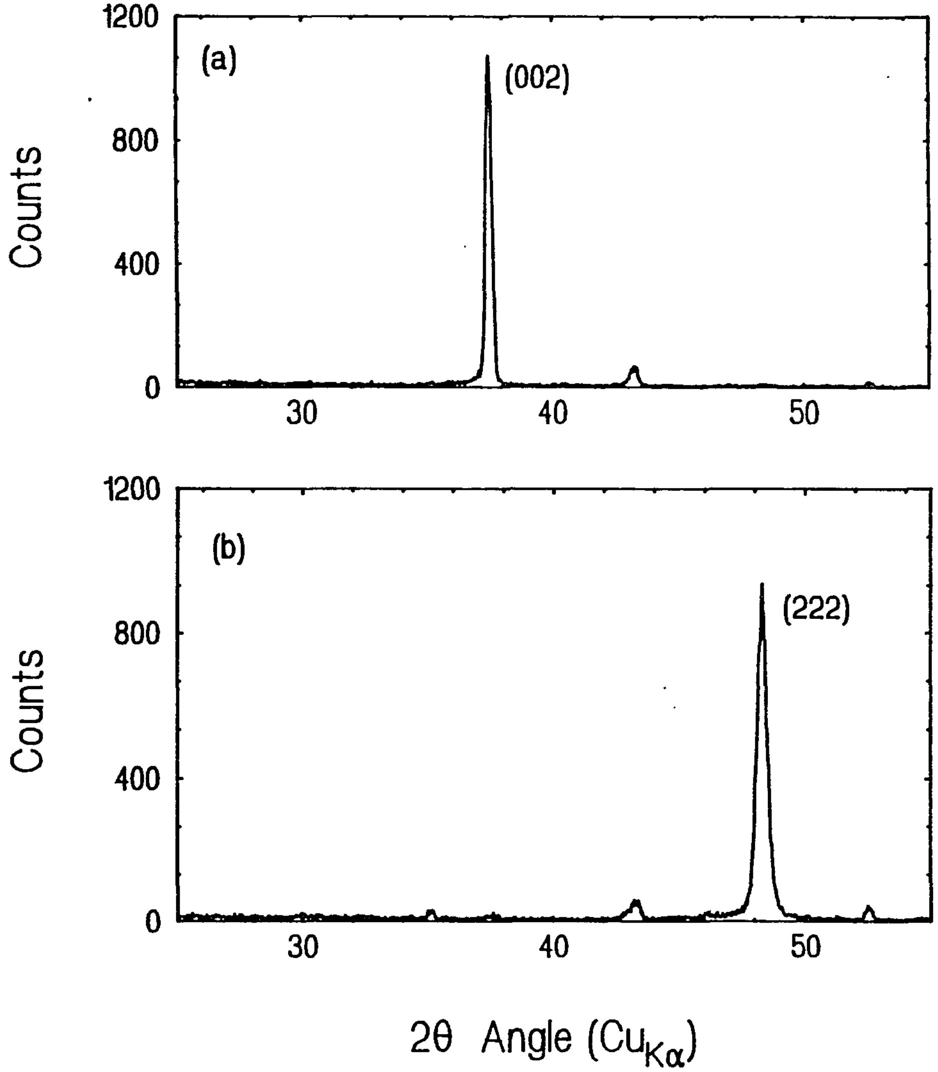
(a)
(002)
(b)
(222)
Counts
Counts
1200
800
400
0
30
40
50
2θ Angle (Cu$_{K\alpha}$)

Figure 6.2

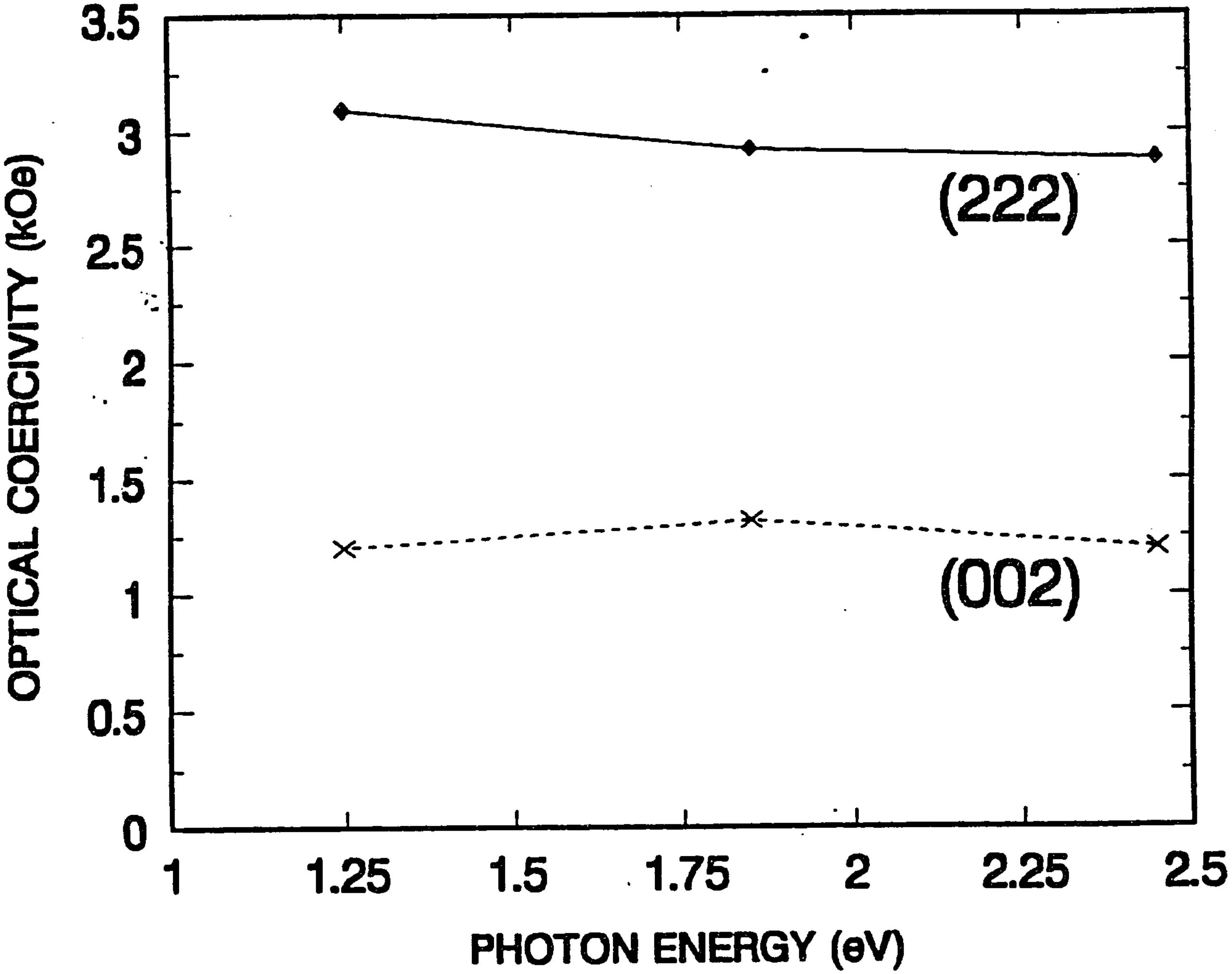
3.5
3
2.5
2
1.5
1
0.5
0
OPTICAL COERCIVITY (kOe)
1
1.25
1.5
1.75
2
2.25
2.5
PHOTON ENERGY (eV)
(222)
(002)

Figure 6.3

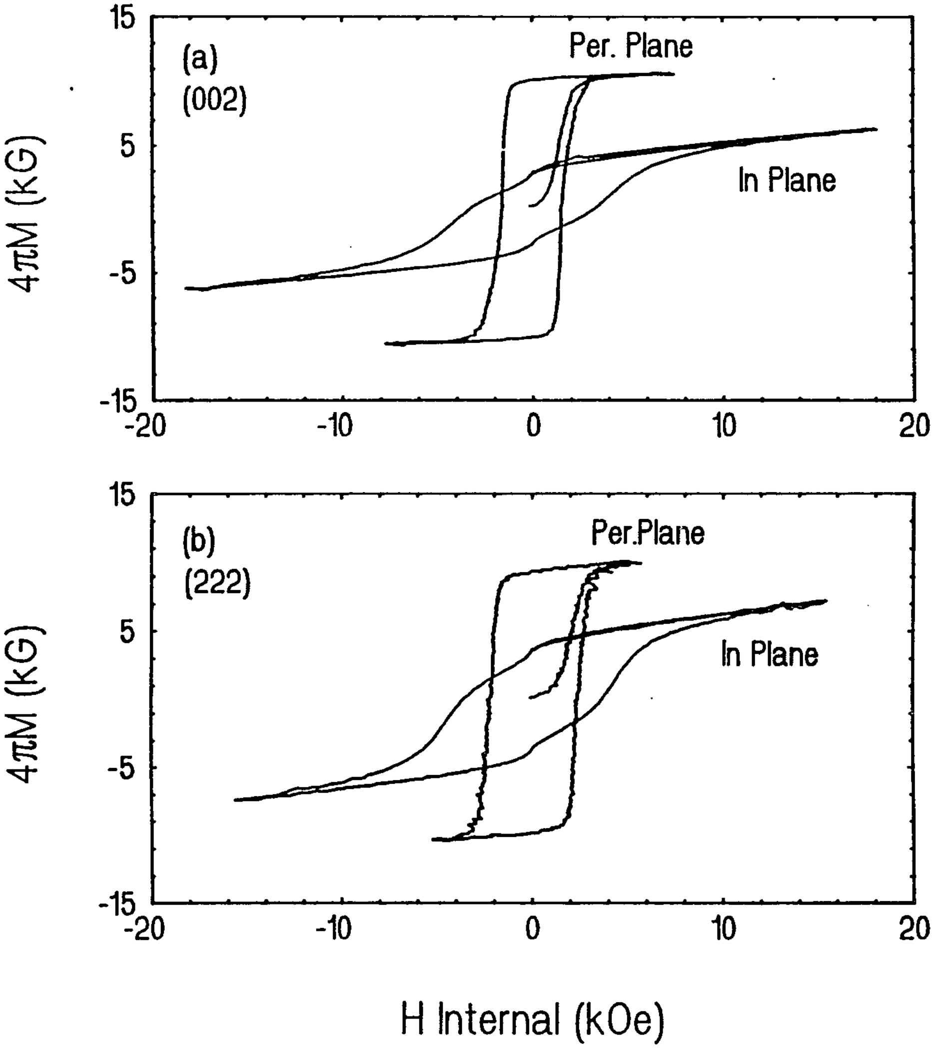
(a)
(002)
Per. Plane
In Plane
4πM (kG)
15
5
-5
-15
-20
-10
0
10
20
(b)
(222)
Per.Plane
In Plane
4πM (kG)
15
5
-5
-15
-20
-10
0
10
20
H Internal (kOe)

Figure 6.4

Figure 6.5

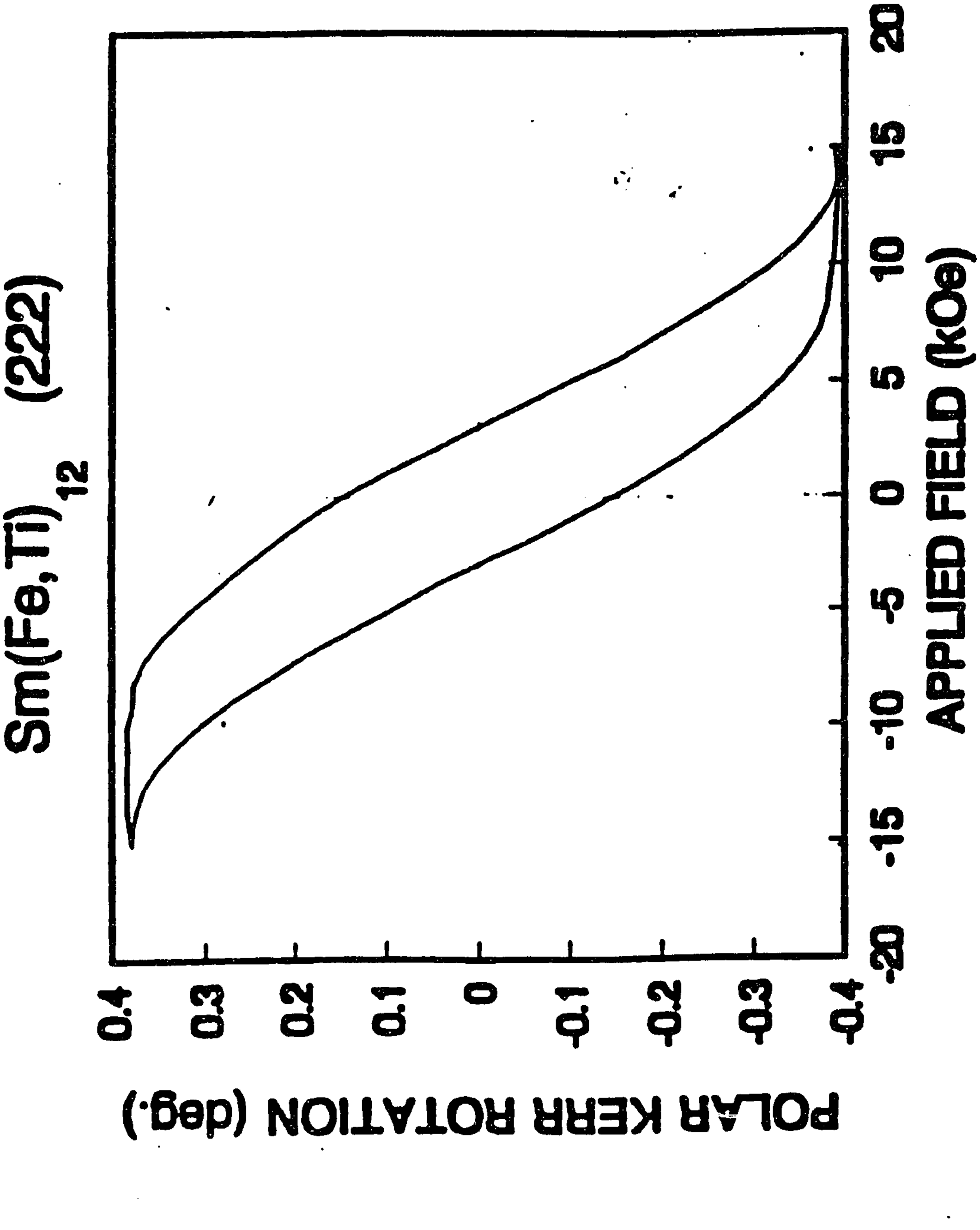
Sm(Fe,Ti)12 (222)
POLAR KERR ROTATION (deg.)
0.4
0.3
0.2
0.1
0
-0.1
-0.2
-0.3
-0.4
APPLIED FIELD (kOe)
-20
-15
-10
-5
0
5
10
15
20

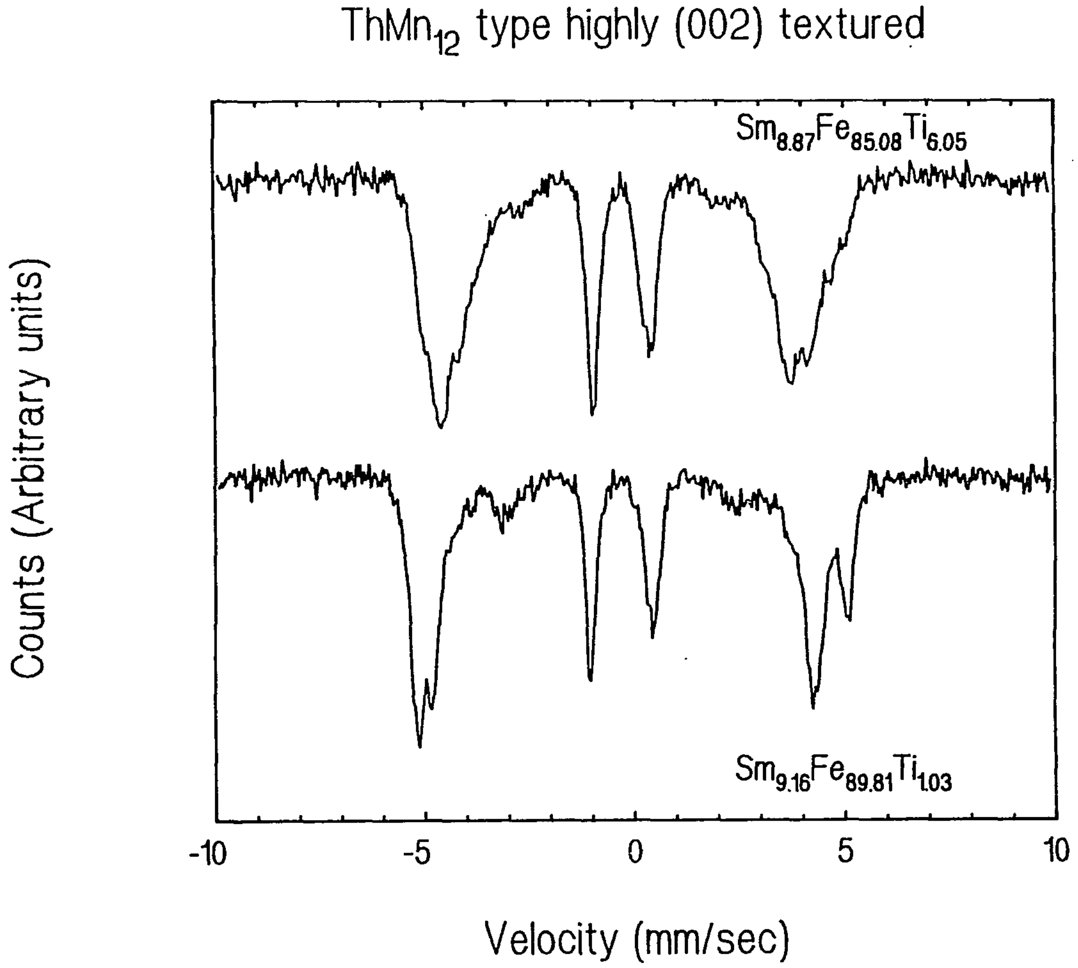
ThMn$_{12}$ type highly (002) textured
Sm$_{8.87}$Fe$_{85.08}$Ti$_{6.05}$
Sm$_{9.16}$Fe$_{89.81}$Ti$_{1.03}$
Counts (Arbitrary units)
-10
-5
0
5
10
Velocity (mm/sec)

Figure 6.6

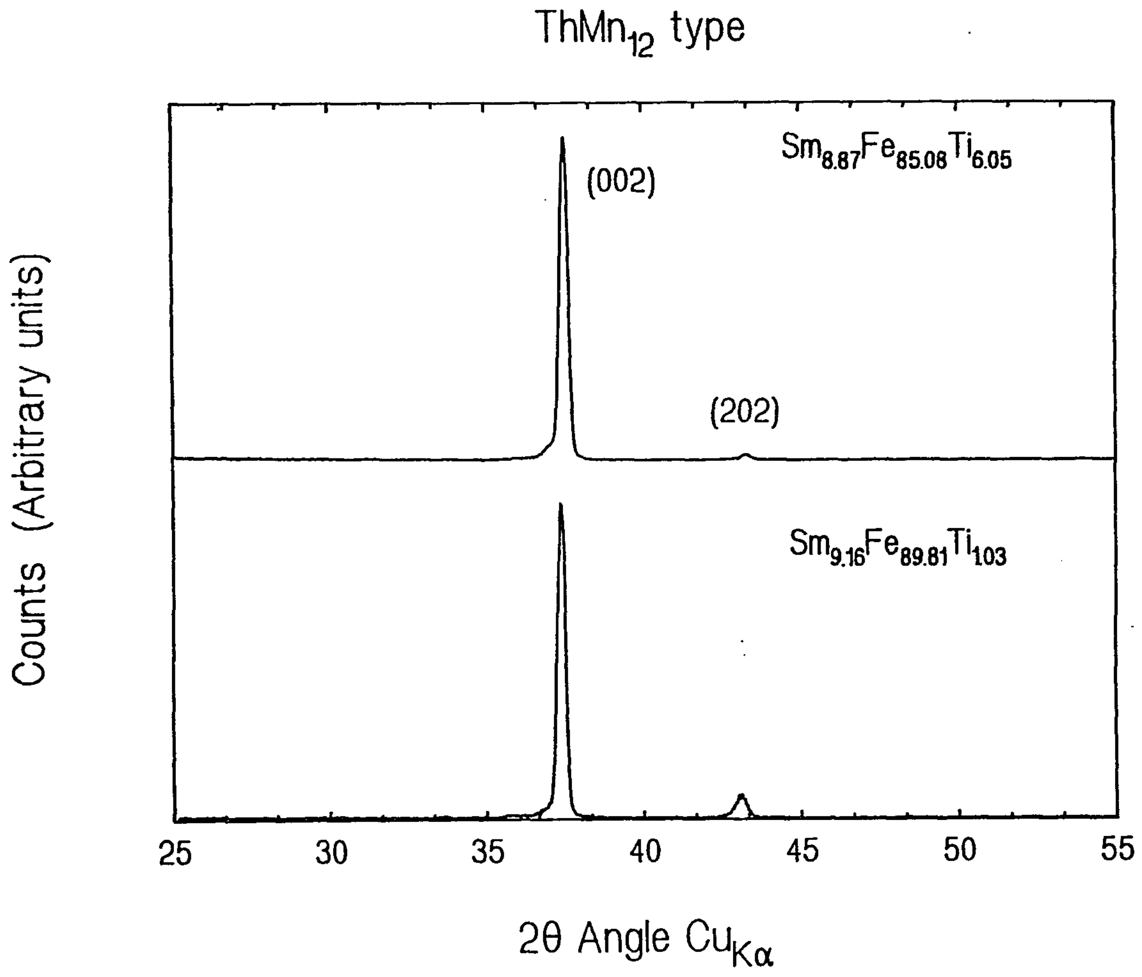
ThMn$_{12}$ type
(002)
$Sm_{8.87}Fe_{85.08}Ti_{6.05}$
(202)
$Sm_{9.16}Fe_{89.81}Ti_{1.03}$
Counts (Arbitrary units)
25
30
35
40
45
50
55
2θ Angle $Cu_{K\alpha}$

Figure 6.7

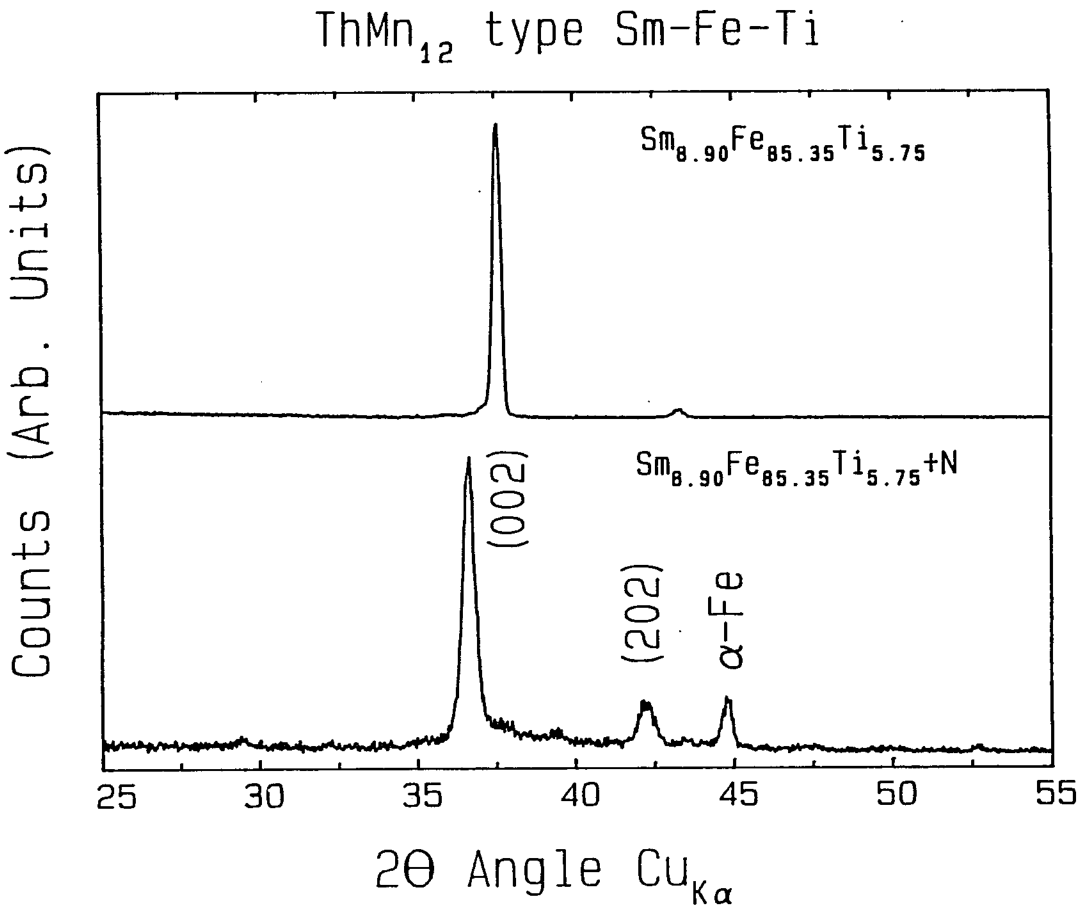

ThMn$_{12}$ type Sm-Fe-Ti
Counts (Arb. Units)
$Sm_{8.90}Fe_{85.35}Ti_{5.75}$
$Sm_{8.90}Fe_{85.35}Ti_{5.75}$+N
(002)
(202)
α-Fe
25
30
35
40
45
50
55
2Θ Angle Cu$_{K\alpha}$

Figure 7.1

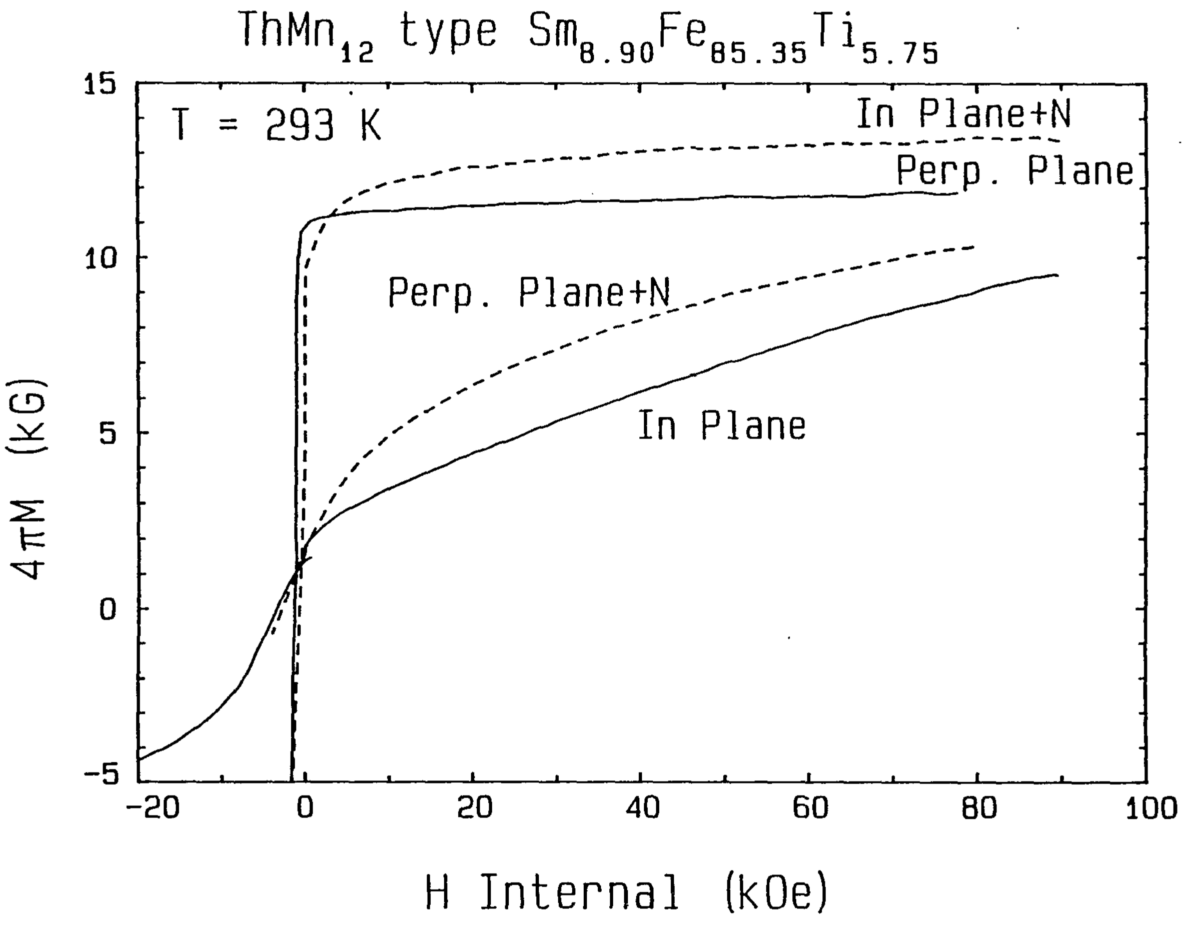
ThMn$_{12}$ type Sm$_{8.90}$Fe$_{85.35}$Ti$_{5.75}$
T = 293 K
In Plane+N
Perp. Plane
Perp. Plane+N
In Plane
15
10
5
0
-5
-20
0
20
40
60
80
100
4πM (kG)
H Internal (kOe)

Figure 7.2

(002) Textured Nd(Fe, Ti)$_{12}$

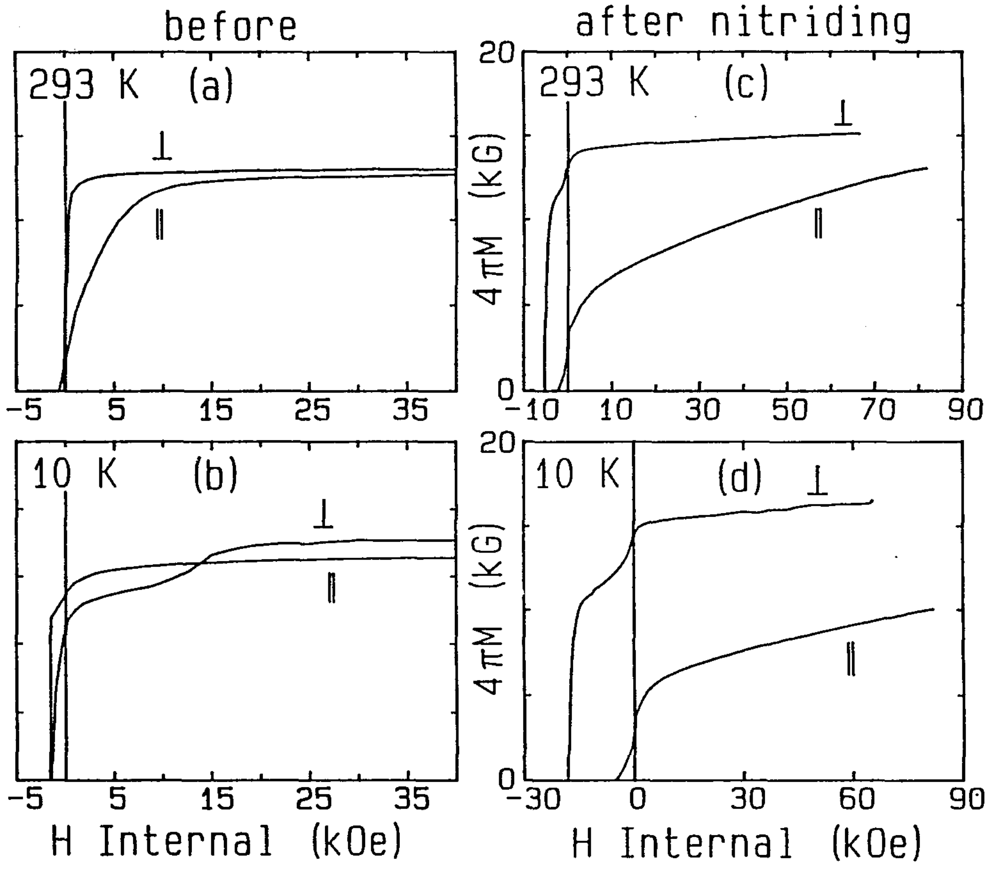

$(BH)_{max}$=26 MGOe
H_A=108 kOe

$(BH)_{max}$=36.7 MGOe
H_A=220 kOe

Figure 7.3

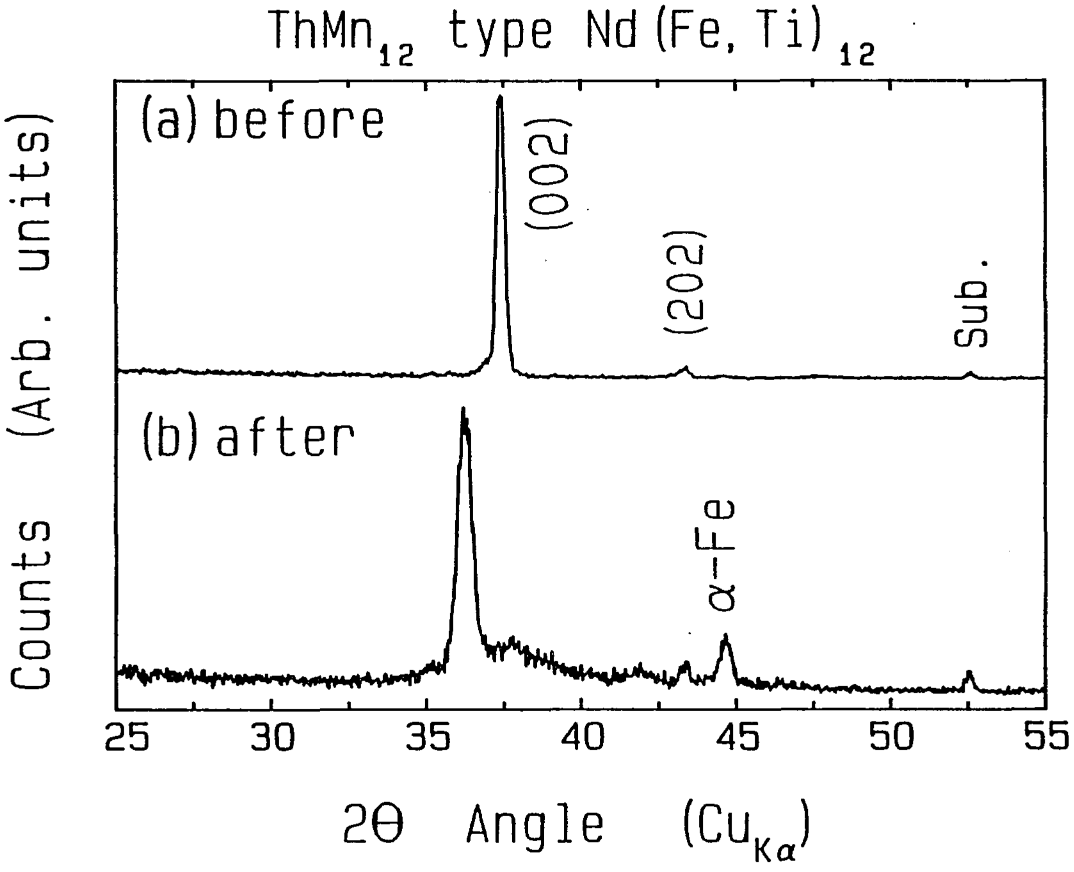
ThMn$_{12}$ type Nd(Fe, Ti)$_{12}$
(a) before
(002)
(202)
Sub.
(b) after
α-Fe
Counts (Arb. units)
25
30
35
40
45
50
55
2Θ Angle (Cu$_{K\alpha}$)

Figure 7.4

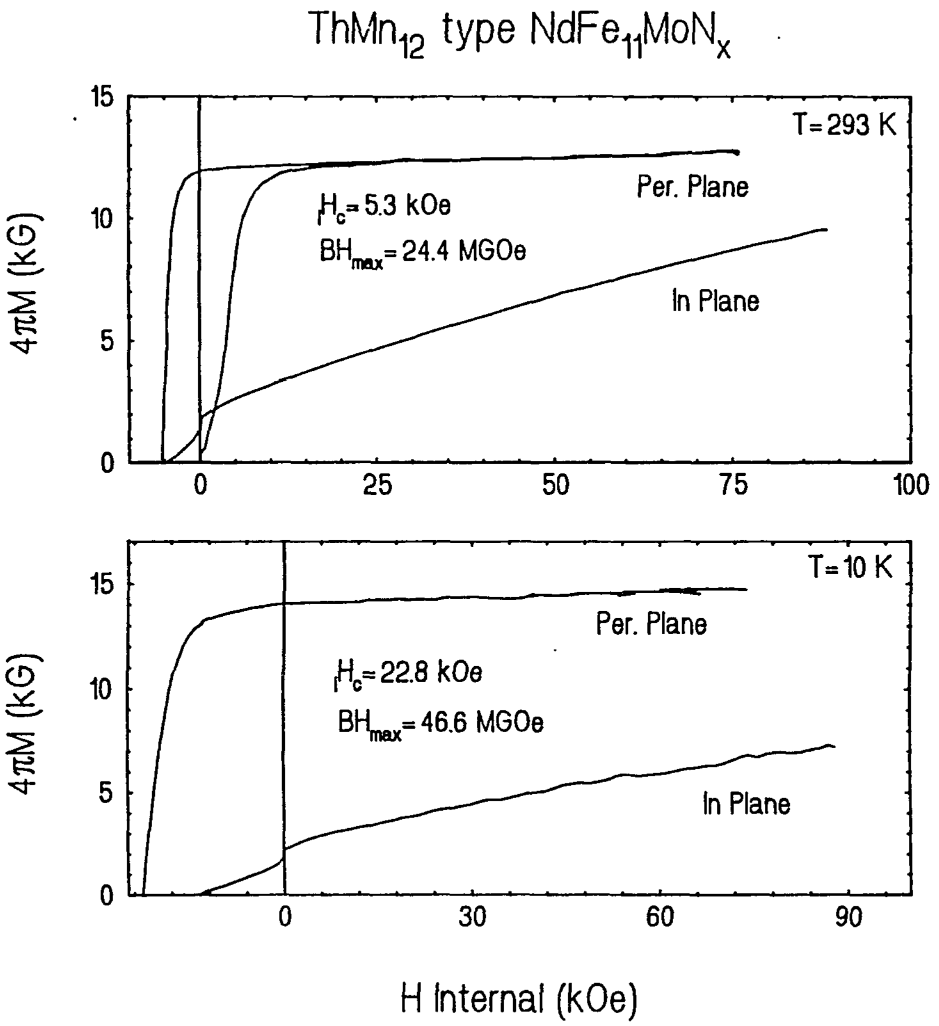
ThMn12 type NdFe11MoNx
T=293 K
Per. Plane
iHc= 5.3 kOe
BHmax= 24.4 MGOe
In Plane
4πM (kG)
15
10
5
0
0
25
50
75
100
T=10 K
Per. Plane
iHc= 22.8 kOe
BHmax= 46.6 MGOe
In Plane
4πM (kG)
15
10
5
0
0
30
60
90
H Internal (kOe)

Figure 7.5

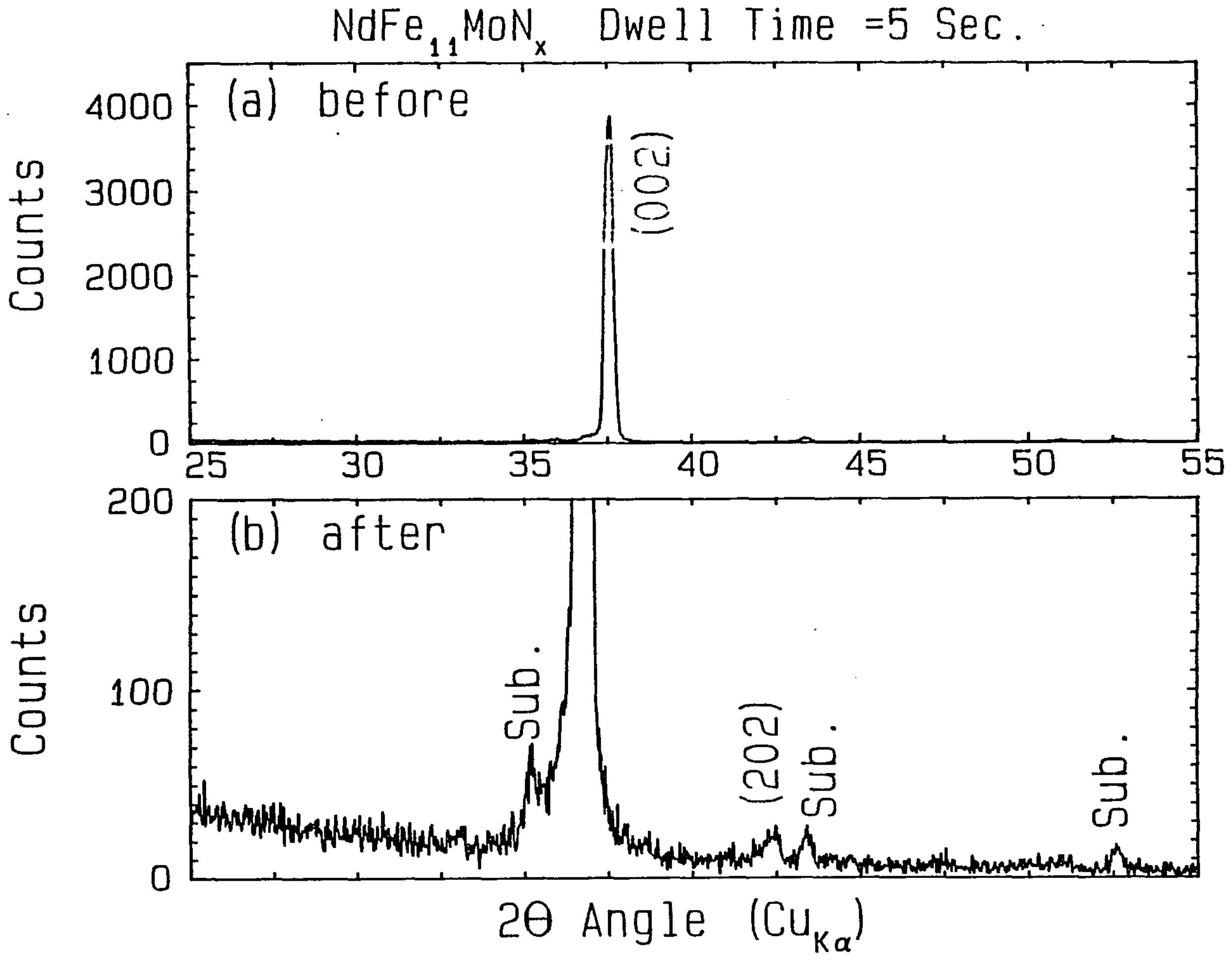
NdFe$_{11}$MoN$_x$ Dwell Time =5 Sec.
(a) before
(002)
Counts
4000
3000
2000
1000
0
25
30
35
40
45
50
55
(b) after
200
100
0
Counts
Sub.
(202)
Sub.
Sub.
2Θ Angle (Cu$_{K\alpha}$)

Figure 7.6

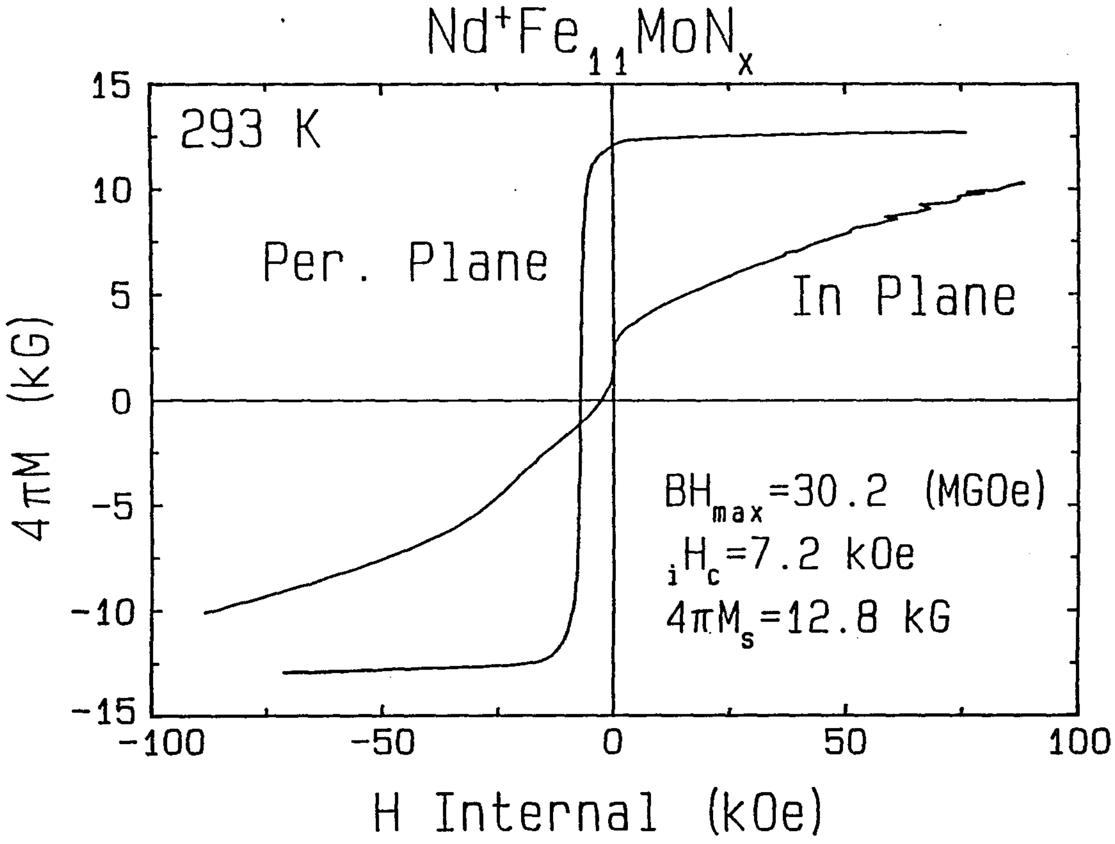
Nd⁺Fe₁₁MoNₓ
293 K
Per. Plane
In Plane
BH_max=30.2 (MGOe)
_iH_c=7.2 kOe
4πM_s=12.8 kG
4πM (kG)
15
10
5
0
-5
-10
-15
-100
-50
0
50
100
H Internal (kOe)

Figure 7.7

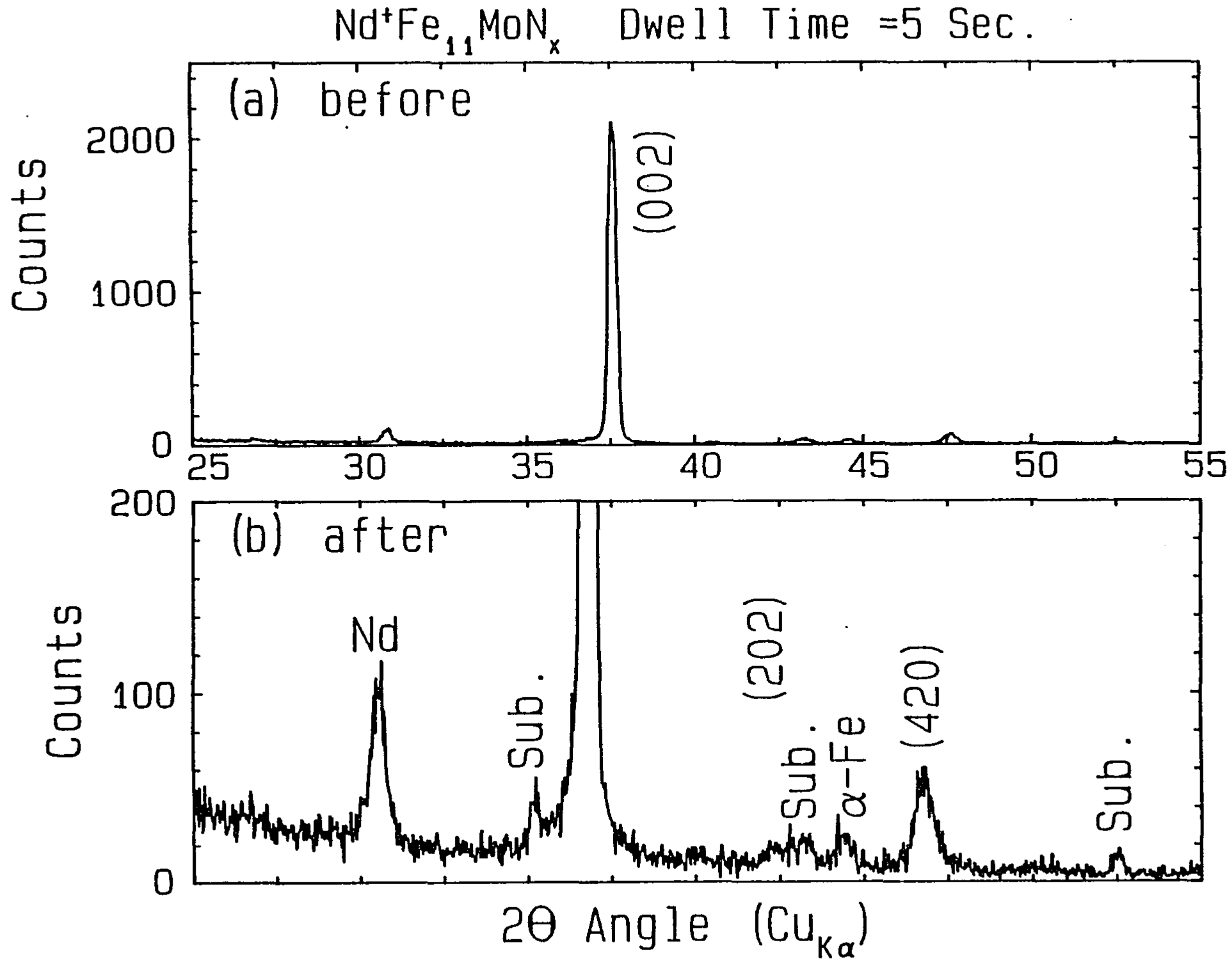
Nd+Fe11MoNx Dwell Time =5 Sec.
(a) before
(002)
Counts
2000
1000
0
25
30
35
40
45
50
55
(b) after
200
100
0
Counts
Nd
Sub.
(202)
Sub.
α-Fe
(420)
Sub.
2Θ Angle (CuKα)

Figure 7.8

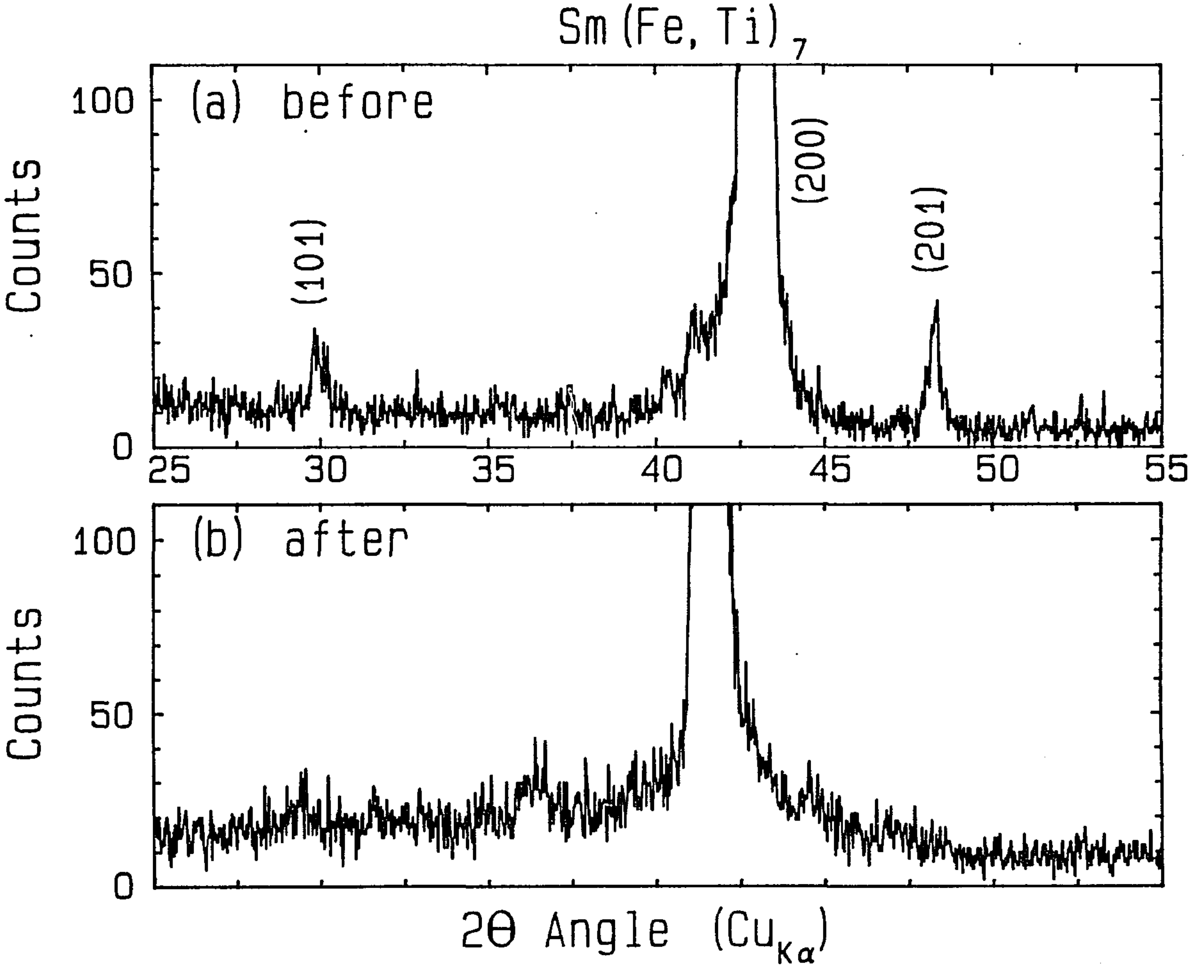
Sm(Fe, Ti)$_7$
(a) before
(101)
(200)
(201)
Counts
0
50
100
25
30
35
40
45
50
55
(b) after
Counts
0
50
100
2Θ Angle (Cu$_{K\alpha}$)

Figure 7.9

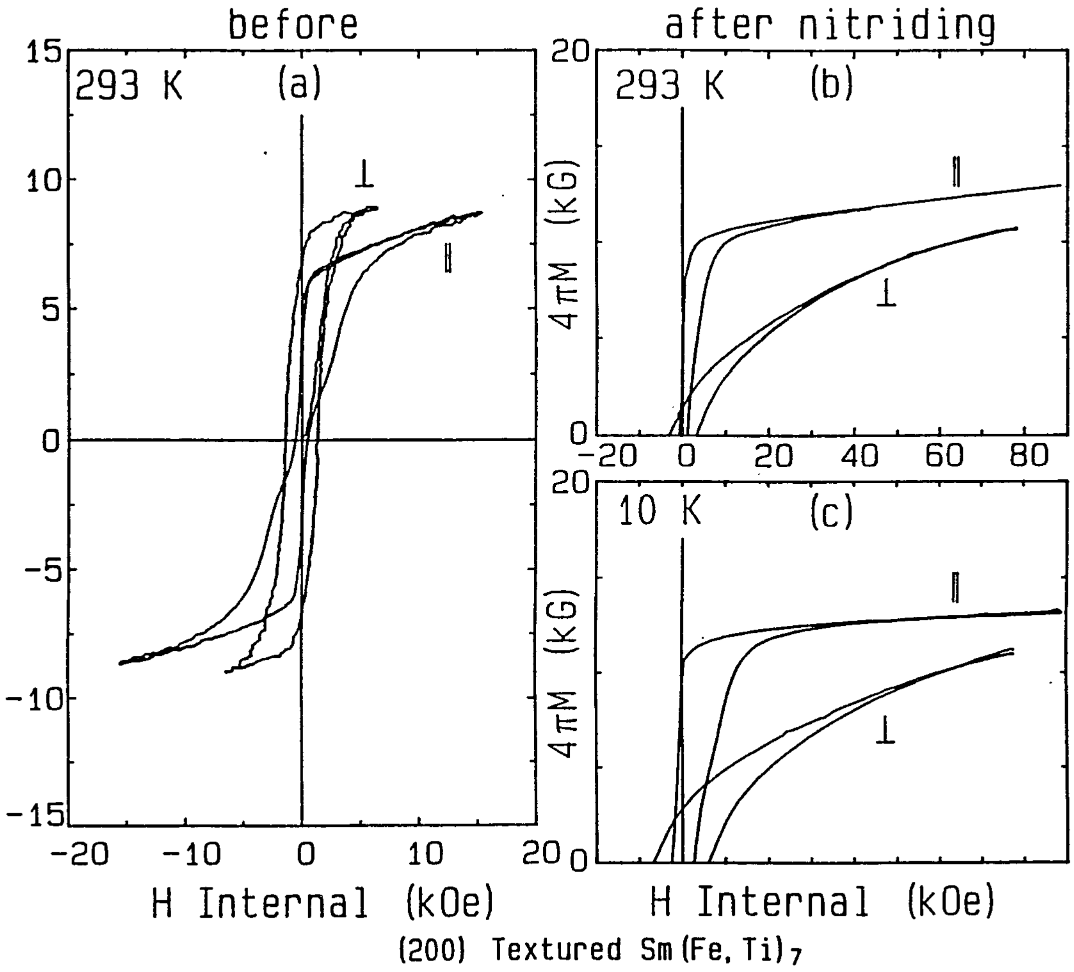
before
after nitriding
293 K
(a)
(b)
10 K
(c)
⊥
∥
4πM (kG)
H Internal (kOe)
15
10
5
0
-5
-10
-15
-20
20
40
60
80
(200) Textured Sm(Fe, Ti)$_7$

Figure 7.10

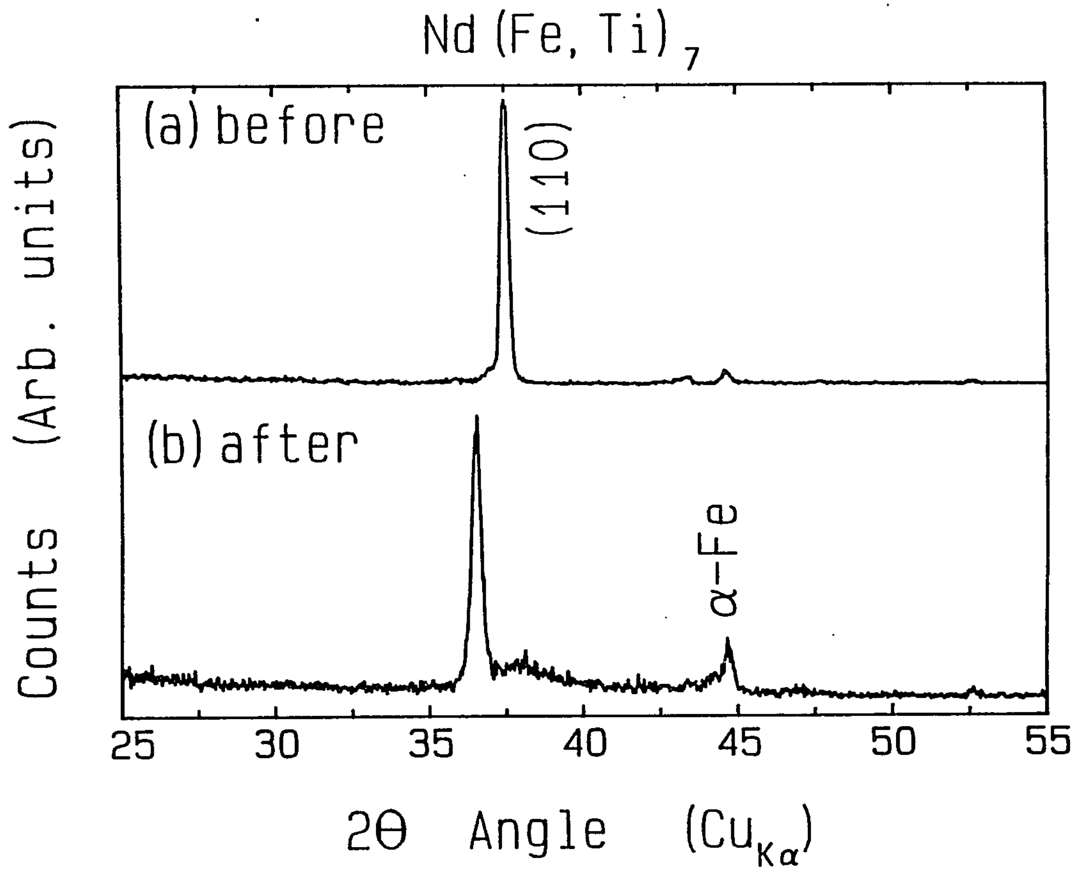
Nd (Fe, Ti)$_7$
(a) before
(110)
(b) after
α-Fe
Counts (Arb. units)
25
30
35
40
45
50
55
2Θ Angle (Cu$_{K\alpha}$)

Figure 7.11

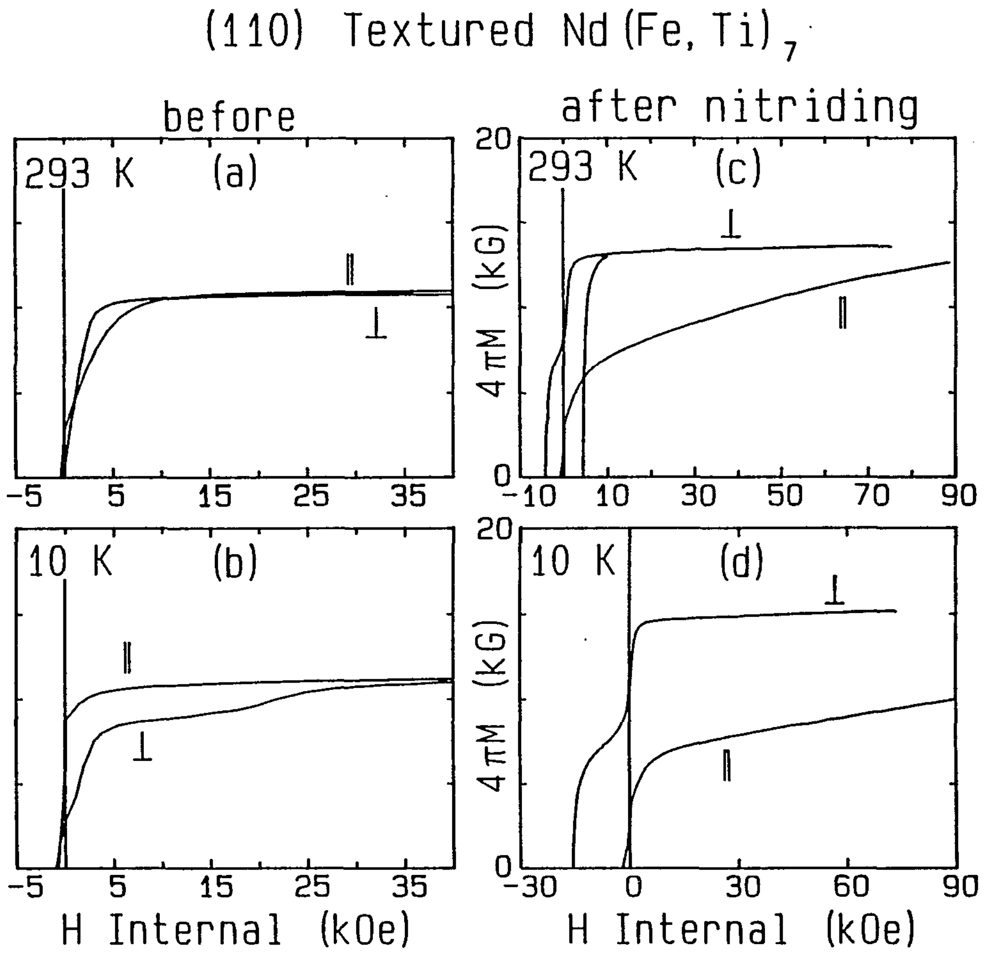
(110) Textured Nd(Fe, Ti)$_7$
before
after nitriding
293 K
(a)
∥
⊥
-5
5
15
25
35
10 K
(b)
∥
⊥
-5
5
15
25
35
H Internal (kOe)
20
0
293 K
(c)
⊥
∥
4πM (kG)
-10
10
30
50
70
90
20
0
10 K
(d)
⊥
∥
4πM (kG)
-30
0
30
60
90
H Internal (kOe)

Figure 7.12

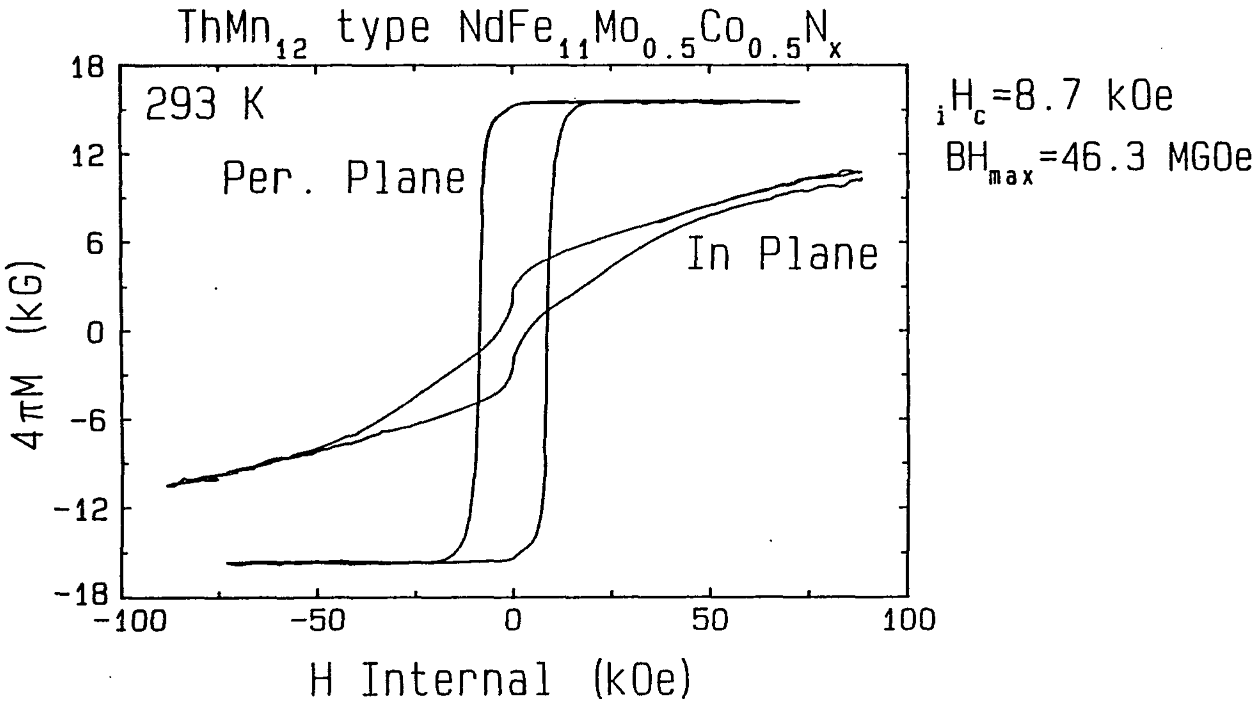
$ThMn_{12}$ type $NdFe_{11}Mo_{0.5}Co_{0.5}N_x$
293 K
Per. Plane
In Plane
$_iH_c$=8.7 kOe
BH_{max}=46.3 MGOe
$4\pi M$ (kG)
18
12
6
0
-6
-12
-18
-100
-50
0
50
100
H Internal (kOe)

Figure 7.13

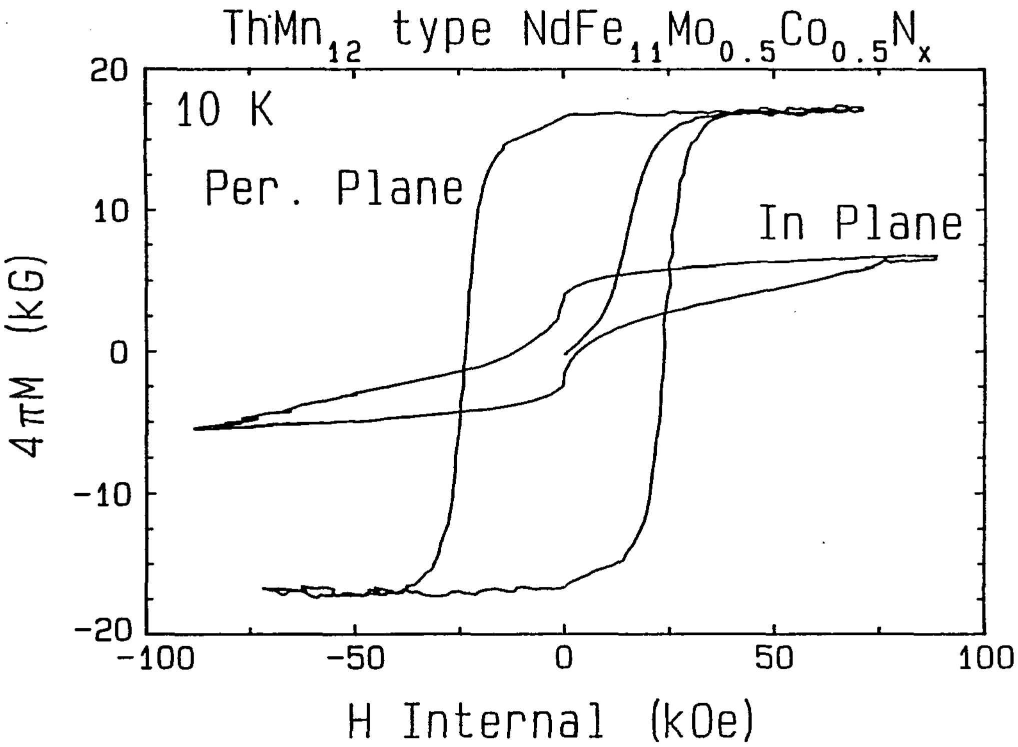

$_iH_c$=24 kOe

BH_{max}=59.6 MGOe

Figure 7.14

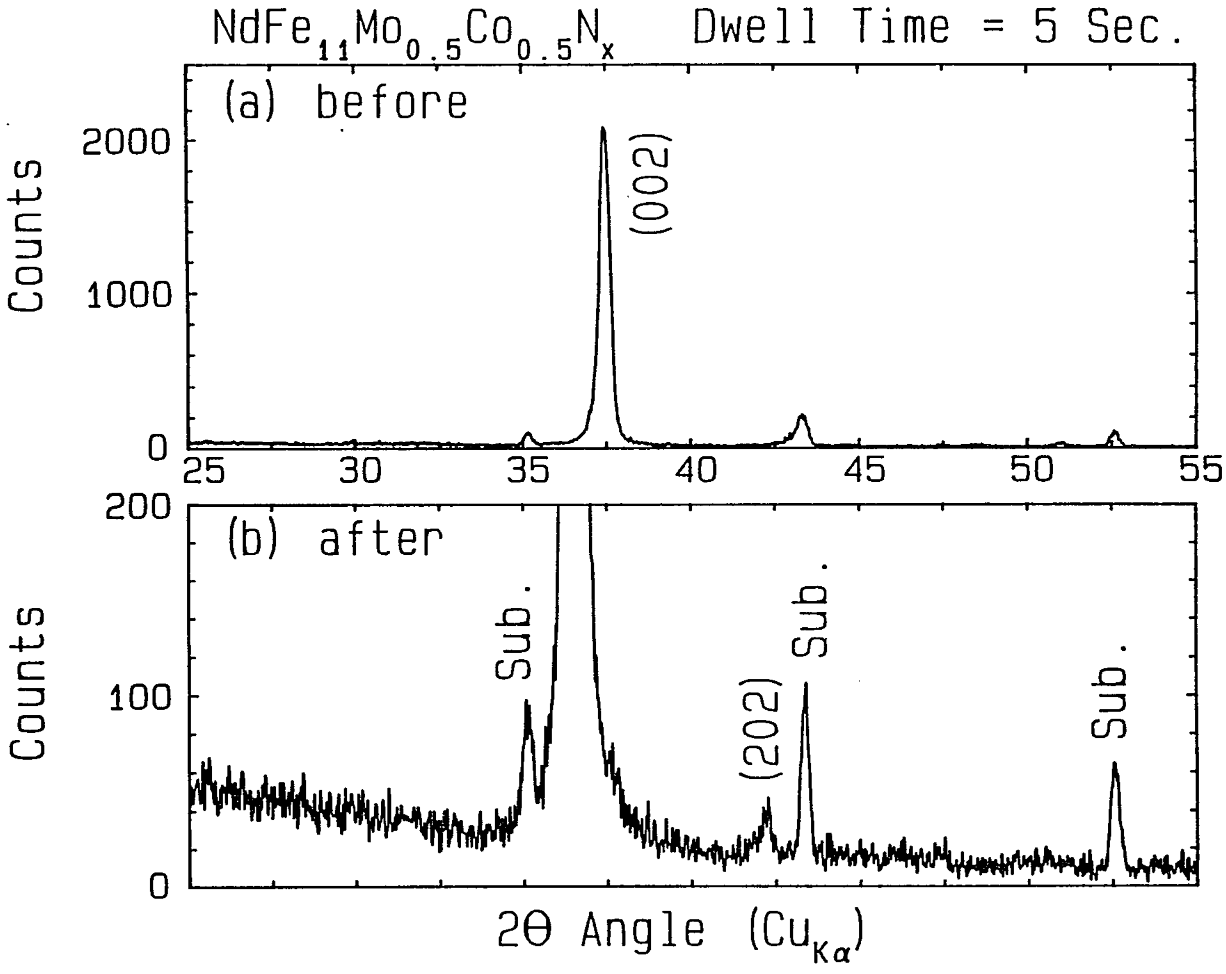

NdFe$_{11}$Mo$_{0.5}$Co$_{0.5}$N$_x$ Dwell Time = 5 Sec.
(a) before
(002)
Counts
0
1000
2000
25
30
35
40
45
50
55
(b) after
Sub.
(202)
Sub.
Sub.
Counts
0
100
200
2Θ Angle (Cu$_{K\alpha}$)

Figure 7.15

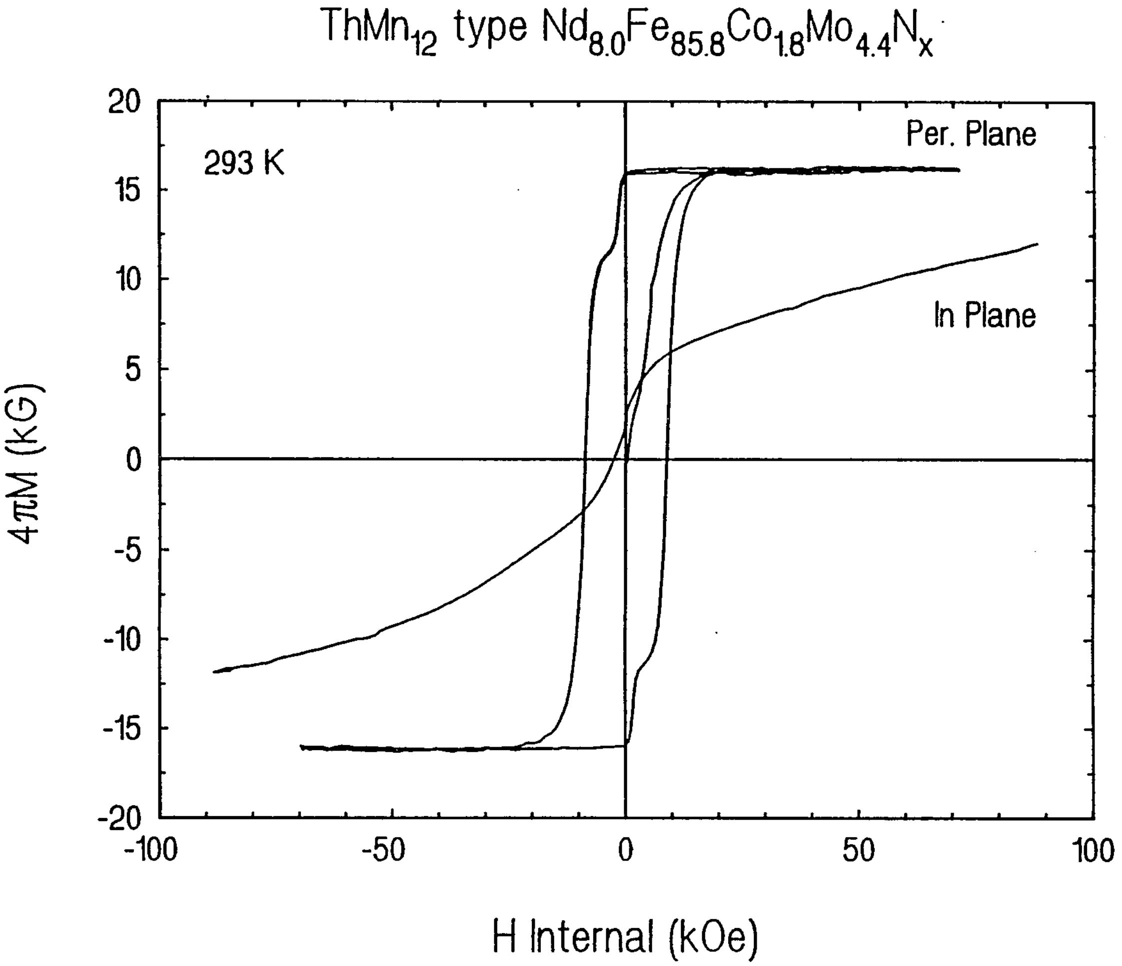
ThMn12 type Nd8.0Fe85.8Co1.8Mo4.4Nx
293 K
Per. Plane
In Plane
20
15
10
5
0
-5
-10
-15
-20
-100
-50
0
50
100
4πM (kG)
H Internal (kOe)

Figure 7.16

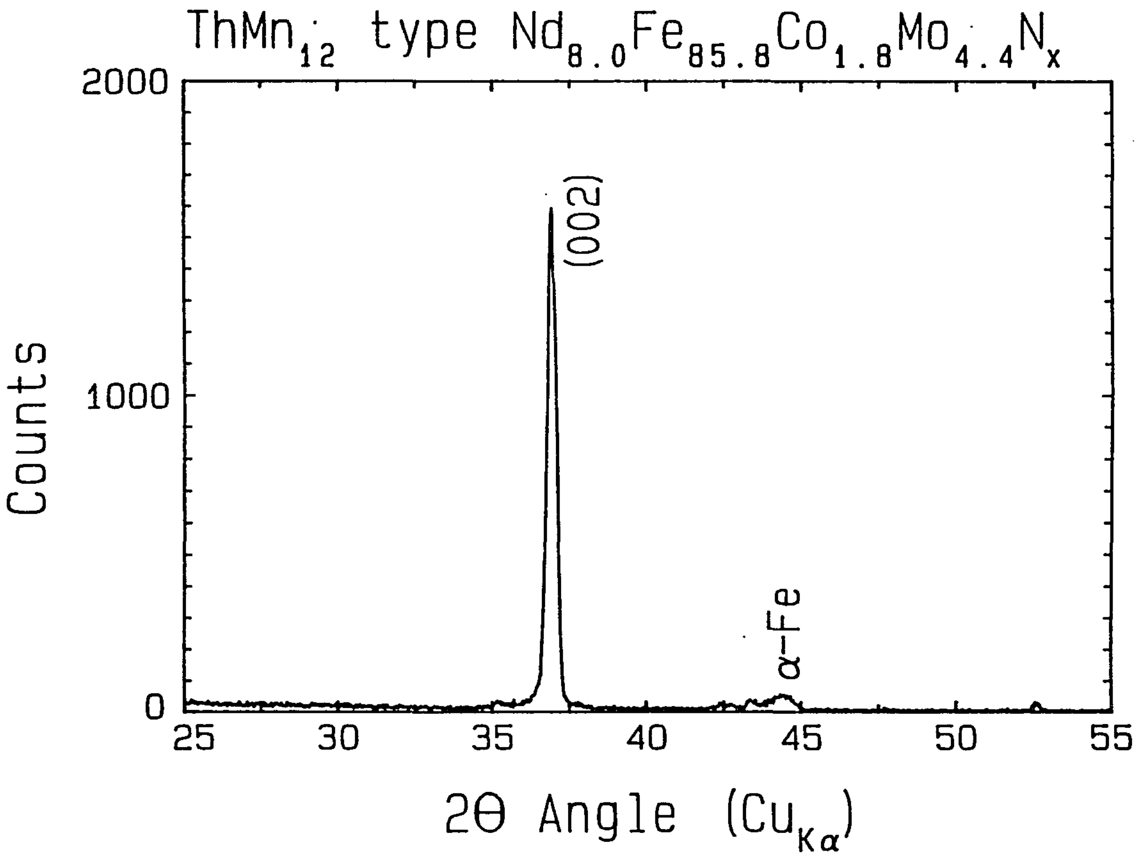
ThMn$_{12}$ type Nd$_{8.0}$Fe$_{85.8}$Co$_{1.8}$Mo$_{4.4}$N$_x$
2000
1000
0
Counts
(002)
α-Fe
25
30
35
40
45
50
55
2Θ Angle (Cu$_{K\alpha}$)

Figure 7.17

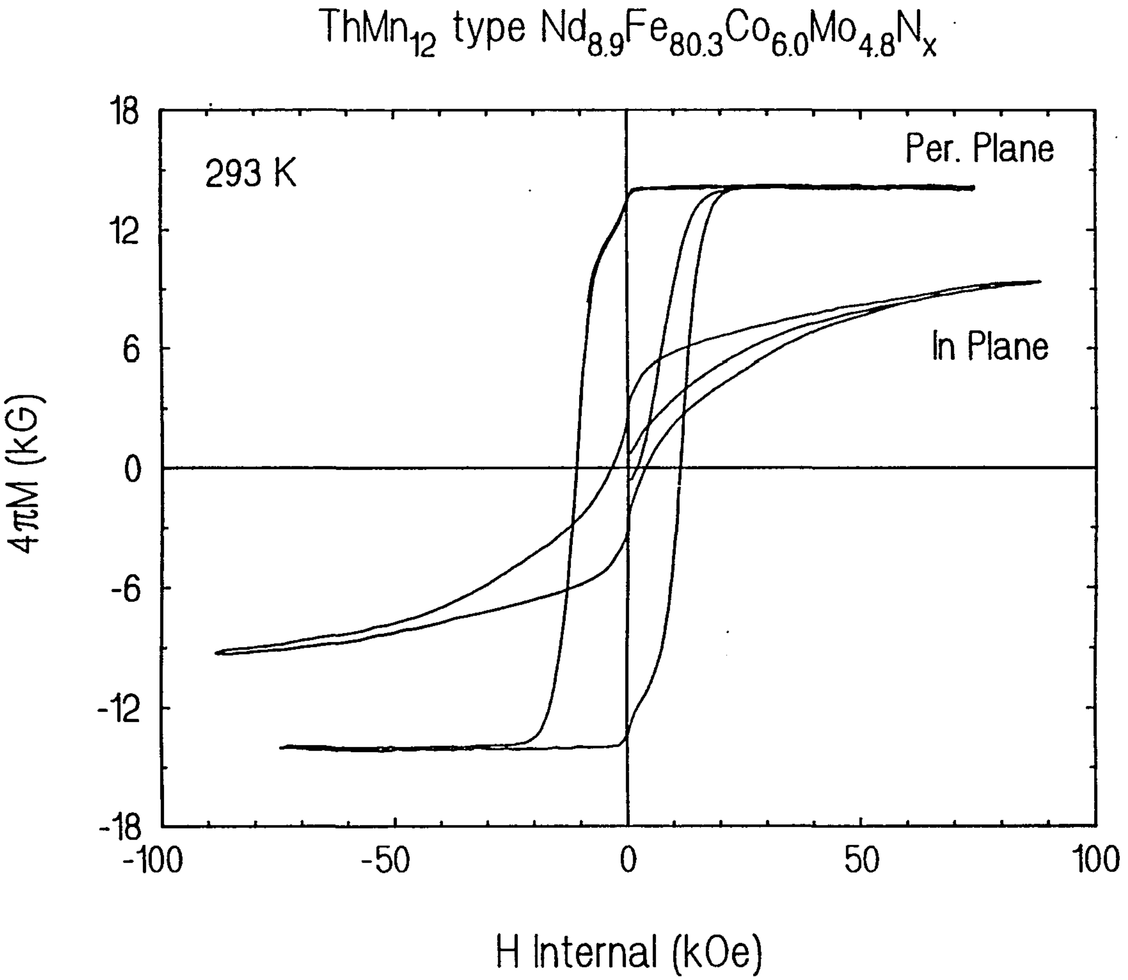
ThMn$_{12}$ type Nd$_{8.9}$Fe$_{80.3}$Co$_{6.0}$Mo$_{4.8}$N$_x$
293 K
Per. Plane
In Plane
4πM (kG)
18
12
6
0
-6
-12
-18
-100
-50
0
50
100
H Internal (kOe)

Figure 7.18

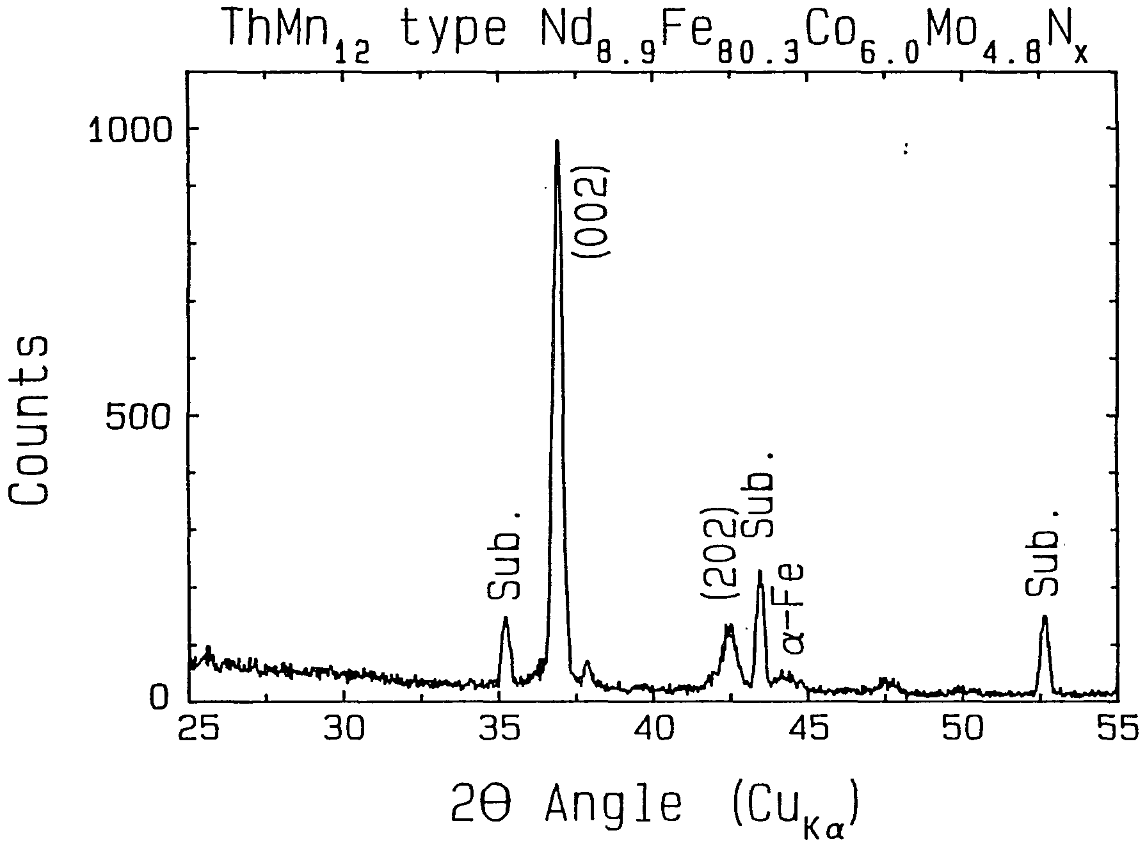
ThMn$_{12}$ type Nd$_{8.9}$Fe$_{80.3}$Co$_{6.0}$Mo$_{4.8}$N$_x$
Counts
1000
500
0
25
30
35
40
45
50
55
2Θ Angle (Cu$_{K\alpha}$)
(002)
Sub.
(202)
Sub.
α-Fe
Sub.

Figure 7.19

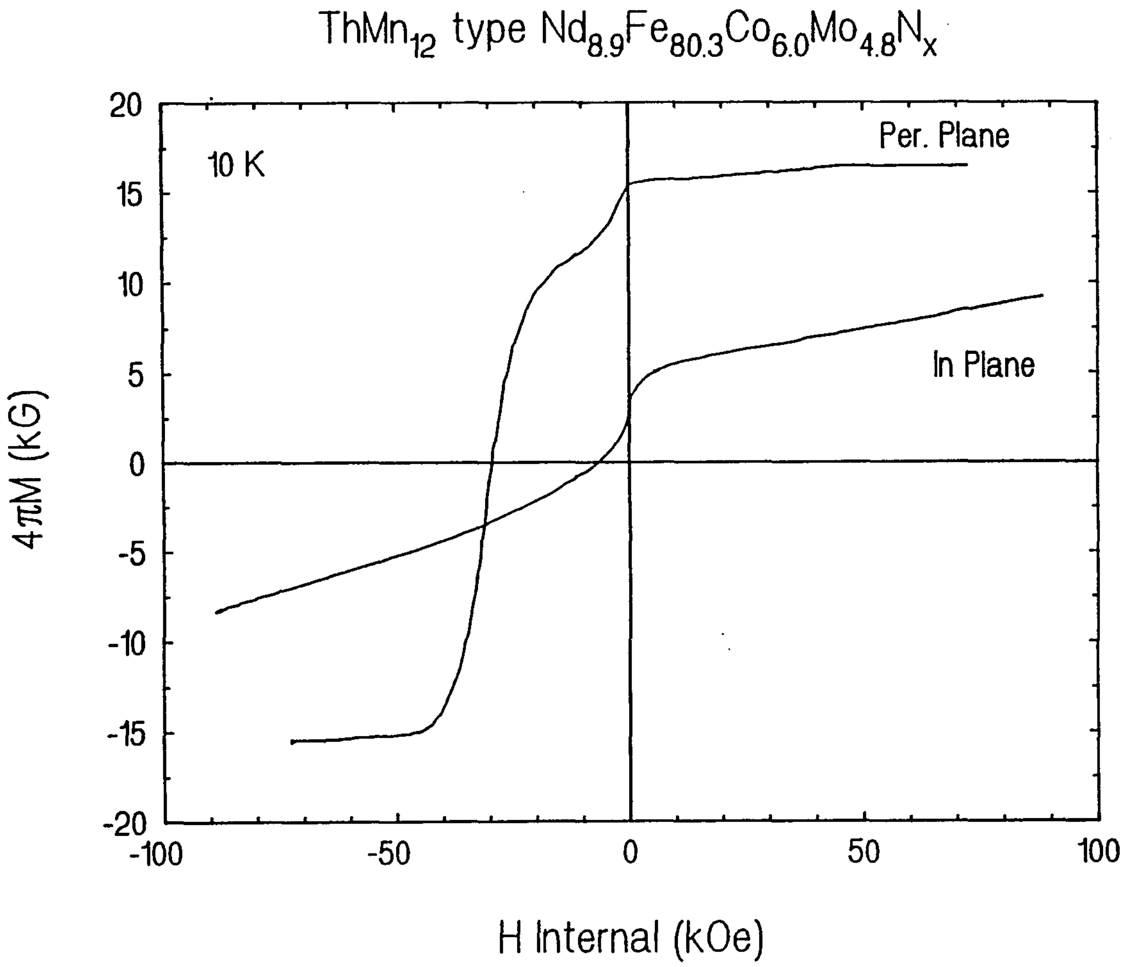
ThMn$_{12}$ type Nd$_{8.9}$Fe$_{80.3}$Co$_{6.0}$Mo$_{4.8}$N$_x$
10 K
Per. Plane
In Plane
4πM (kG)
20
15
10
5
0
-5
-10
-15
-20
-100
-50
0
50
100
H Internal (kOe)

Figure 7.20

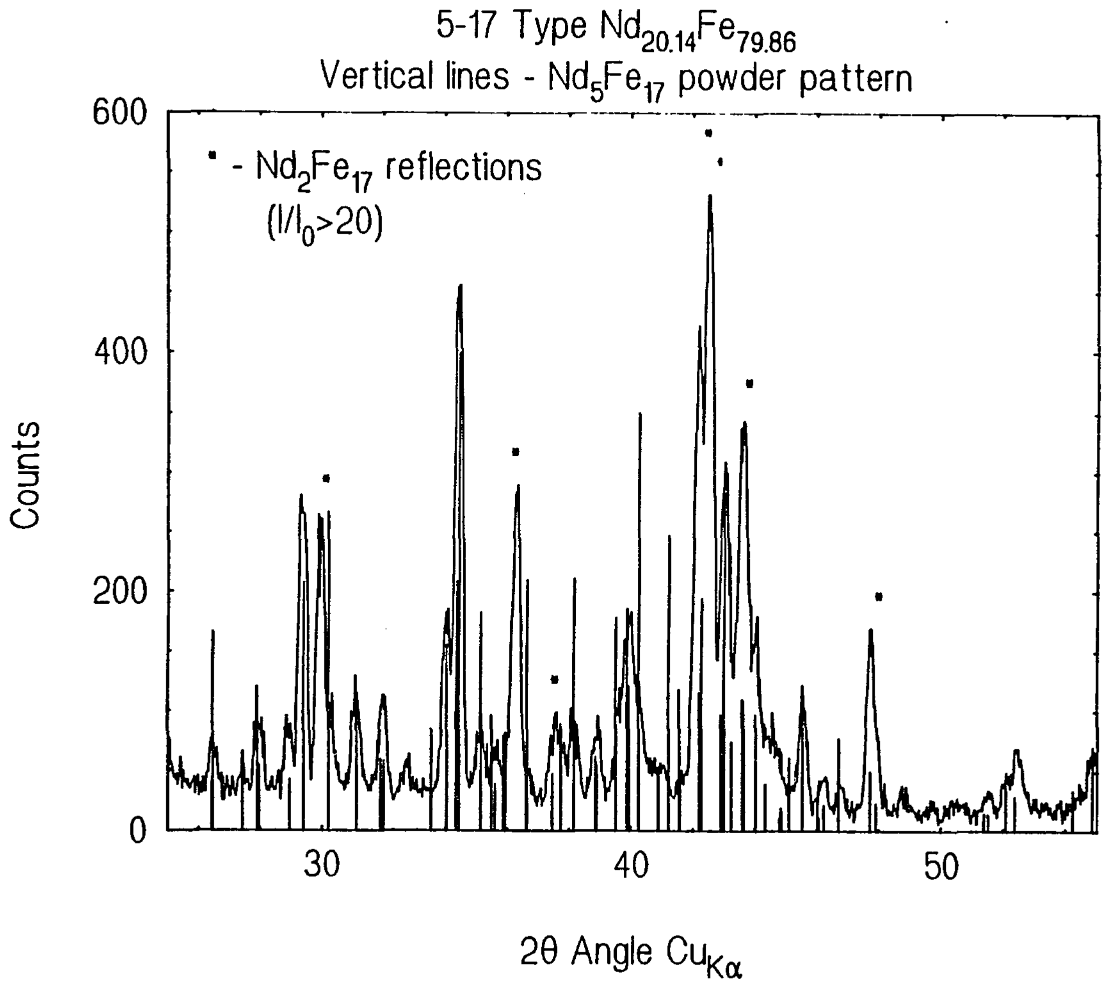
5-17 Type $Nd_{20.14}Fe_{79.86}$
Vertical lines - Nd_5Fe_{17} powder pattern
* - Nd_2Fe_{17} reflections
($I/I_0>20$)
600
400
200
0
Counts
30
40
50
2θ Angle $Cu_{K\alpha}$

Figure 8.1

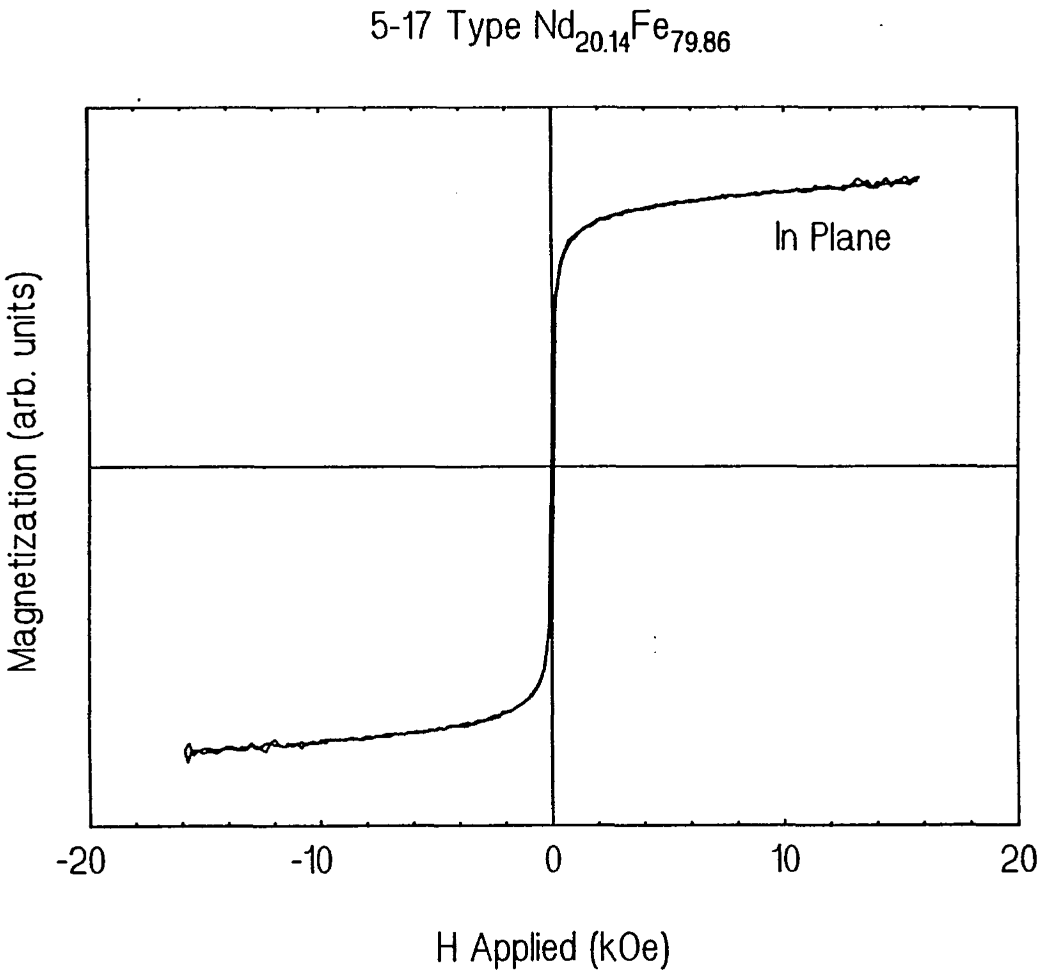
5-17 Type $Nd_{20.14}Fe_{79.86}$
In Plane
Magnetization (arb. units)
H Applied (kOe)
-20
-10
0
10
20

Figure 8.2

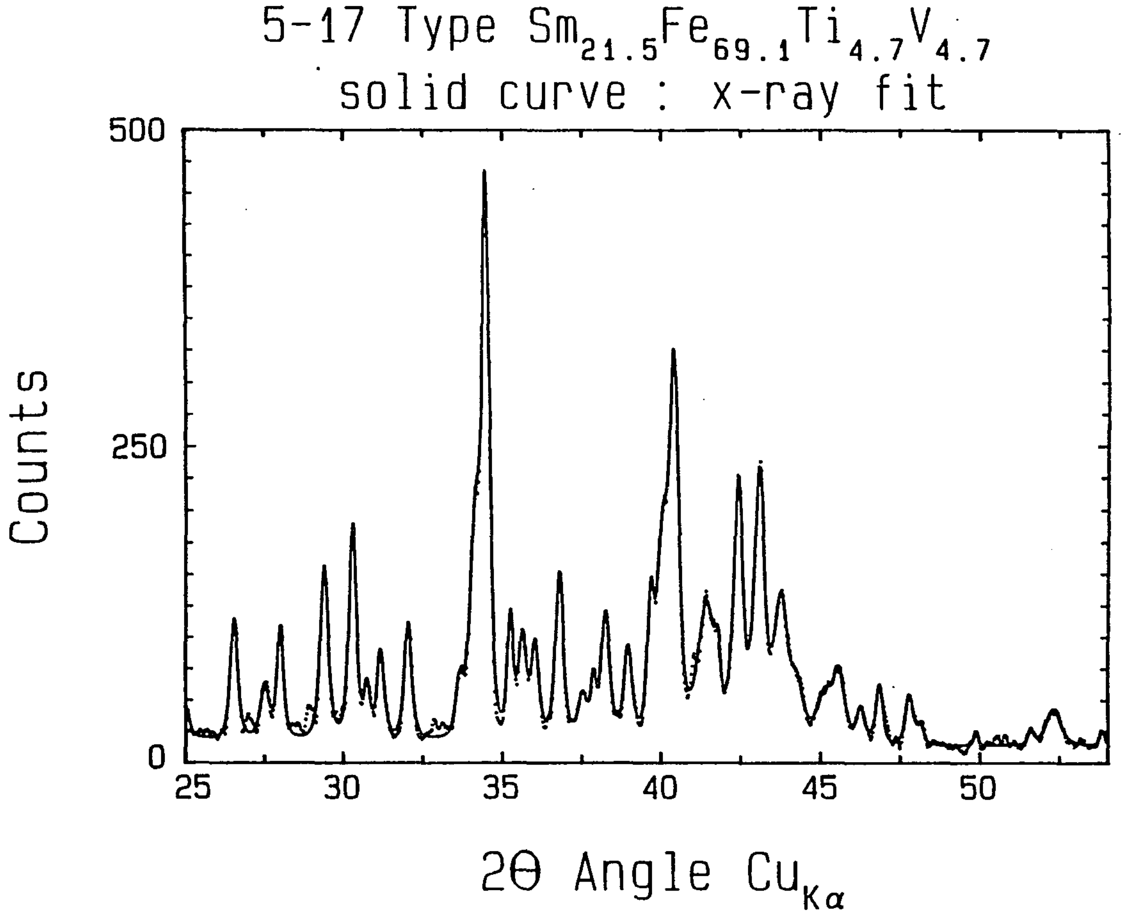
5-17 Type $Sm_{21.5}Fe_{69.1}Ti_{4.7}V_{4.7}$
solid curve : x-ray fit
Counts
500
250
0
25
30
35
40
45
50
2Θ Angle $Cu_{K\alpha}$

Figure 8.3

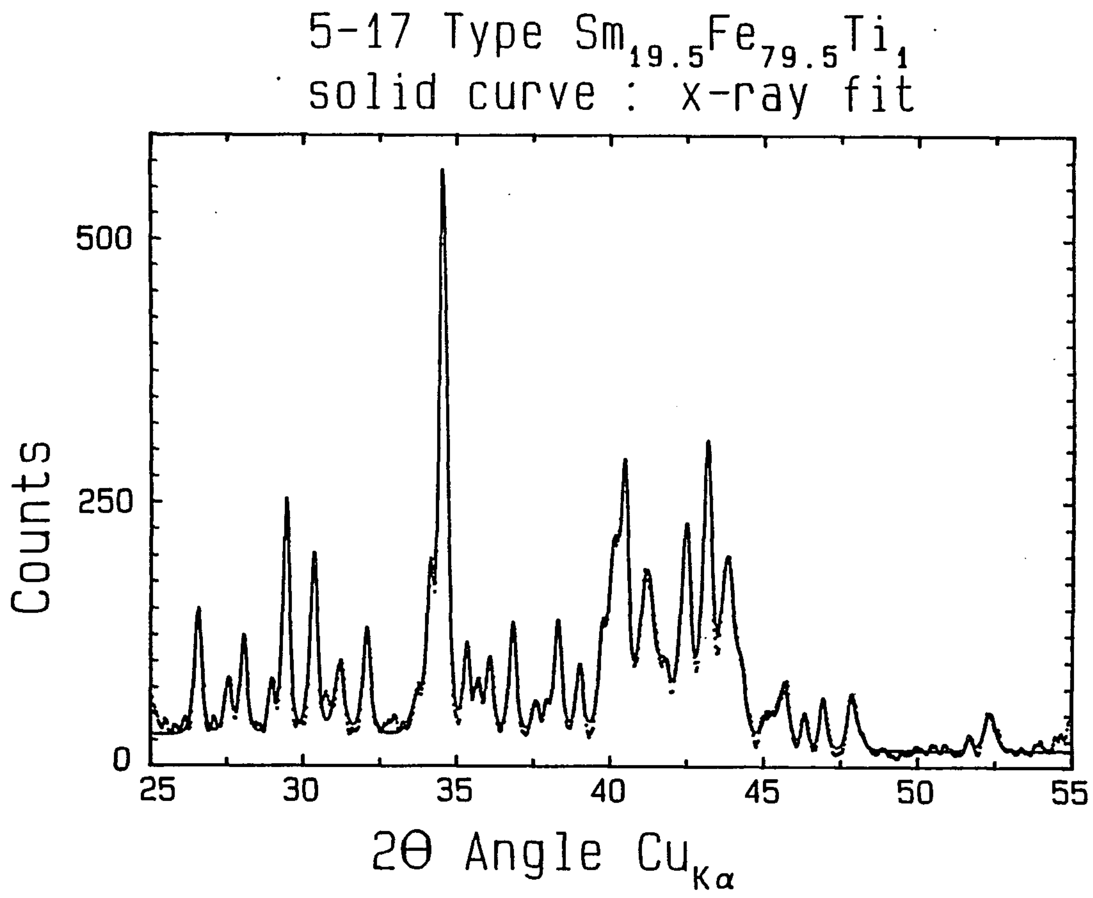
5-17 Type $Sm_{19.5}Fe_{79.5}Ti_1$
solid curve : x-ray fit
Counts
500
250
0
25
30
35
40
45
50
55
2Θ Angle $Cu_{K\alpha}$

Figure 8.4

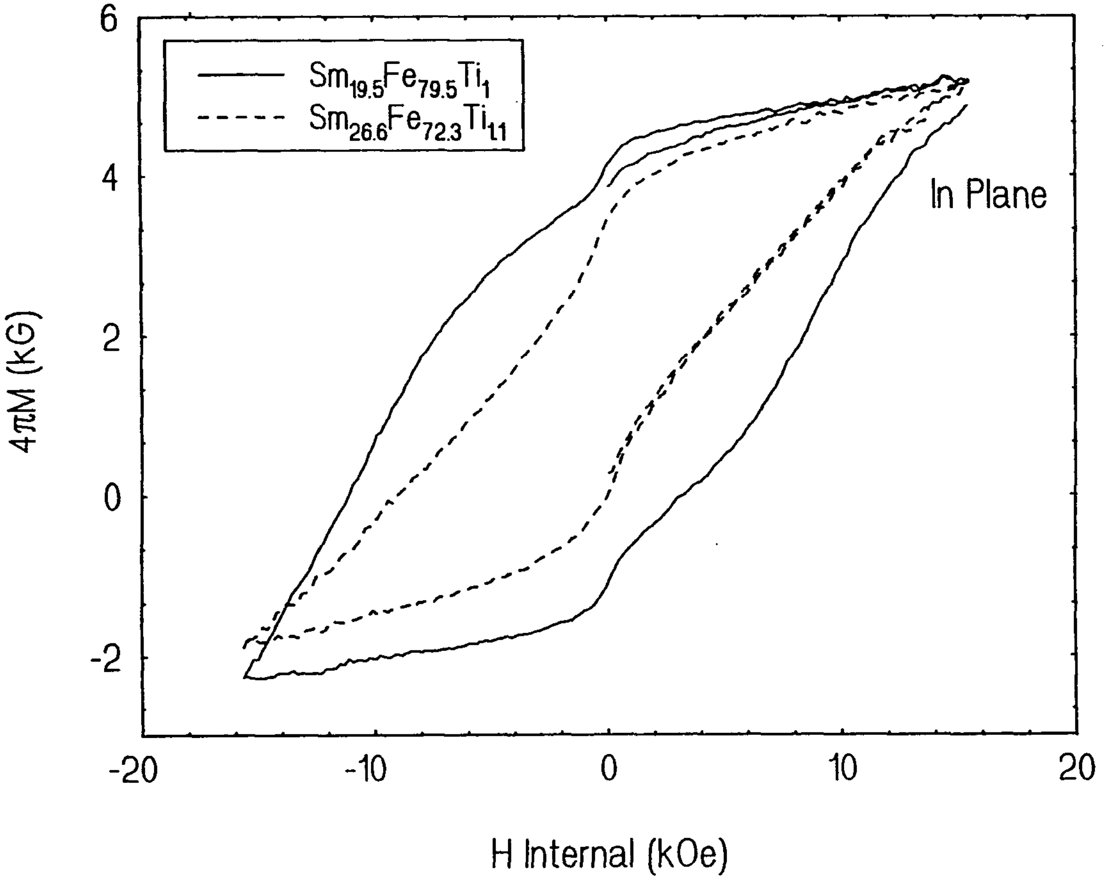

5-17 type Sm-Fe with a trace of Ti

Figure 8.5

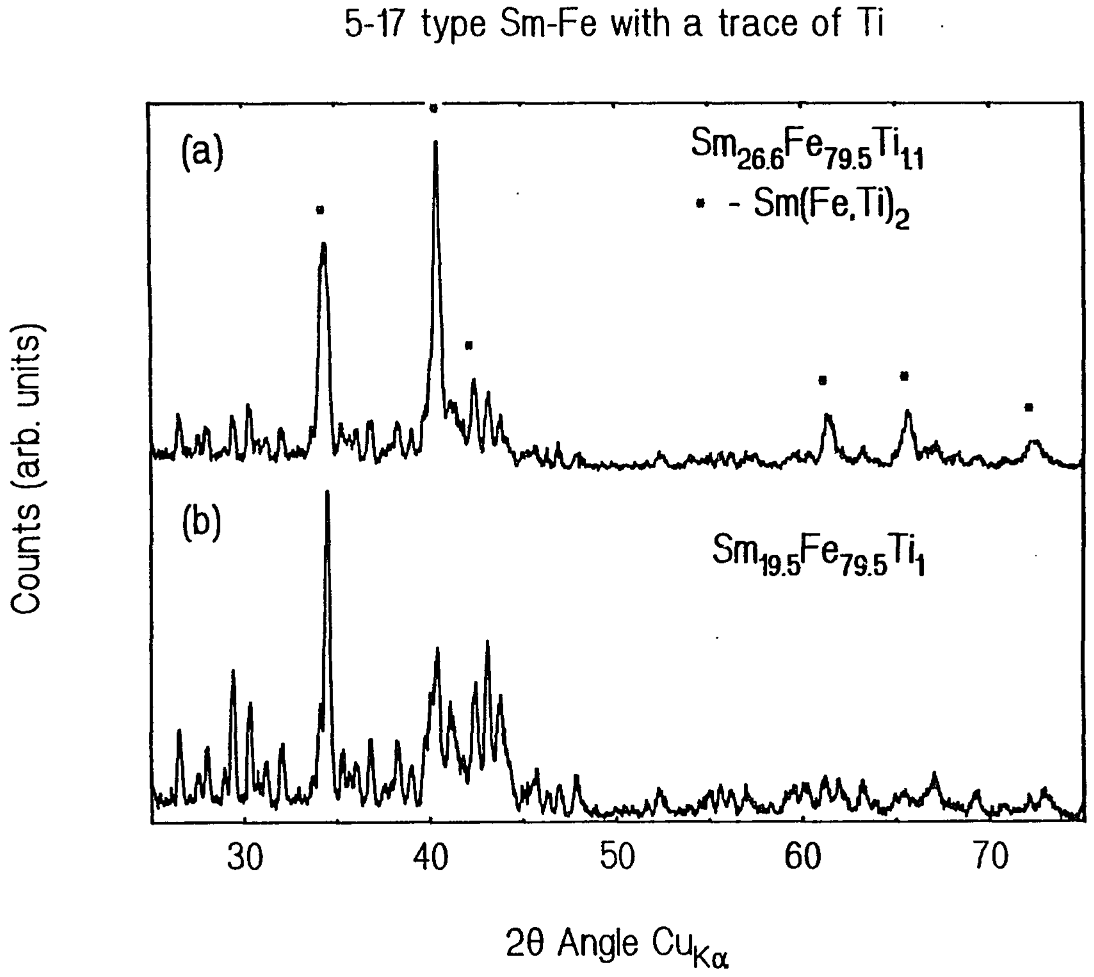
5-17 type Sm-Fe with a trace of Ti
(a)
$Sm_{26.6}Fe_{79.5}Ti_{1.1}$
• - $Sm(Fe,Ti)_2$
(b)
$Sm_{19.5}Fe_{79.5}Ti_1$
Counts (arb. units)
30
40
50
60
70
2θ Angle $Cu_{K\alpha}$

Figure 8.6

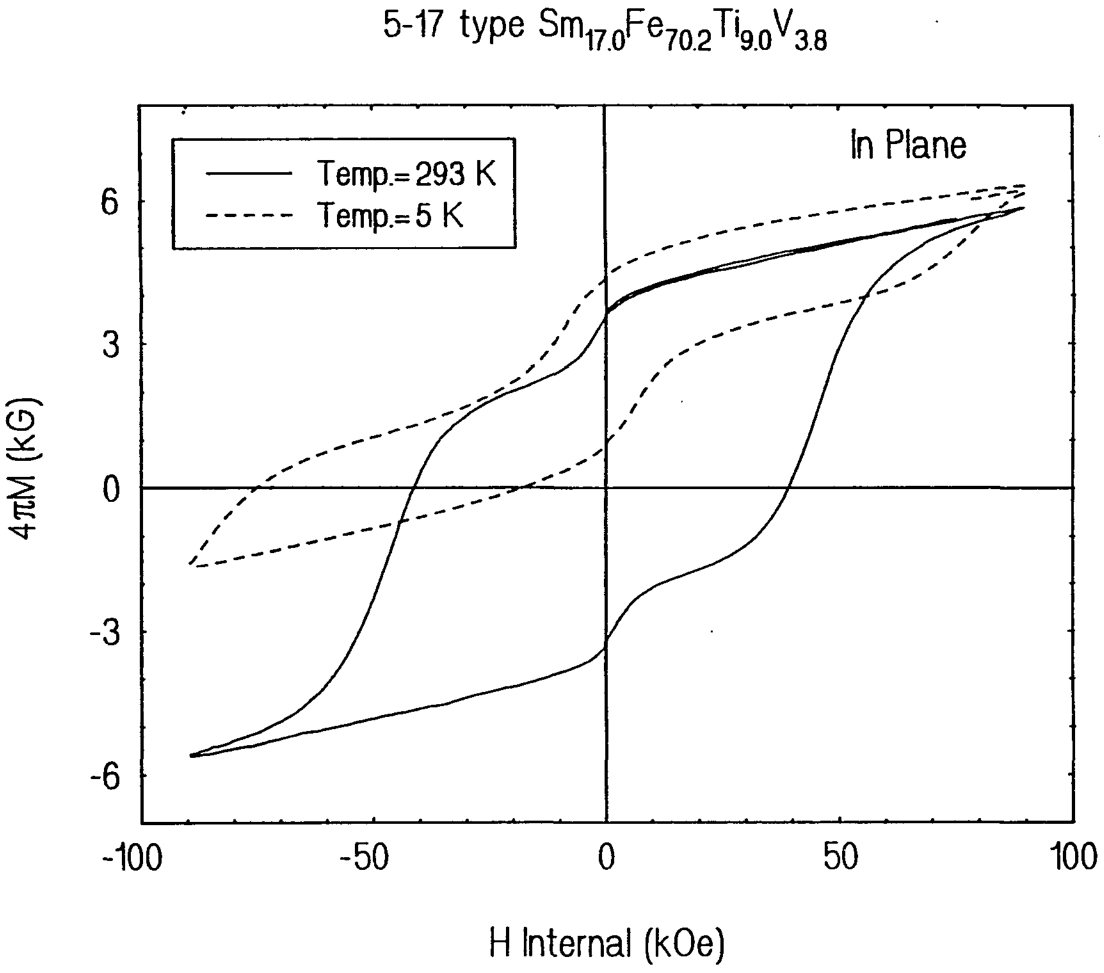
5-17 type $Sm_{17.0}Fe_{70.2}Ti_{9.0}V_{3.8}$
In Plane
Temp.=293 K
Temp.=5 K
6
3
0
-3
-6
4πM (kG)
-100
-50
0
50
100
H Internal (kOe)

Figure 8.7

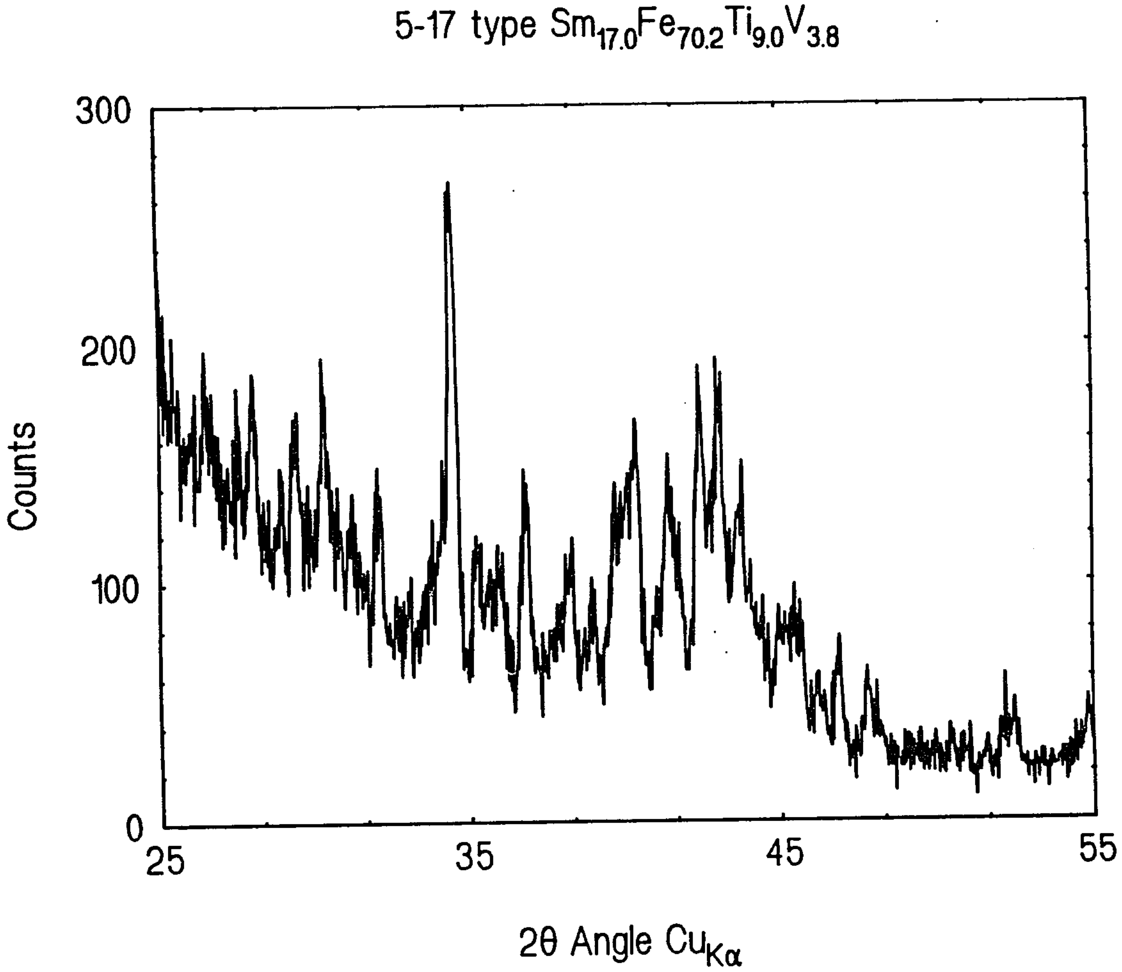
5-17 type $Sm_{17.0}Fe_{70.2}Ti_{9.0}V_{3.8}$
Counts
300
200
100
0
25
35
45
55
2θ Angle $Cu_{K\alpha}$

Figure 8.8

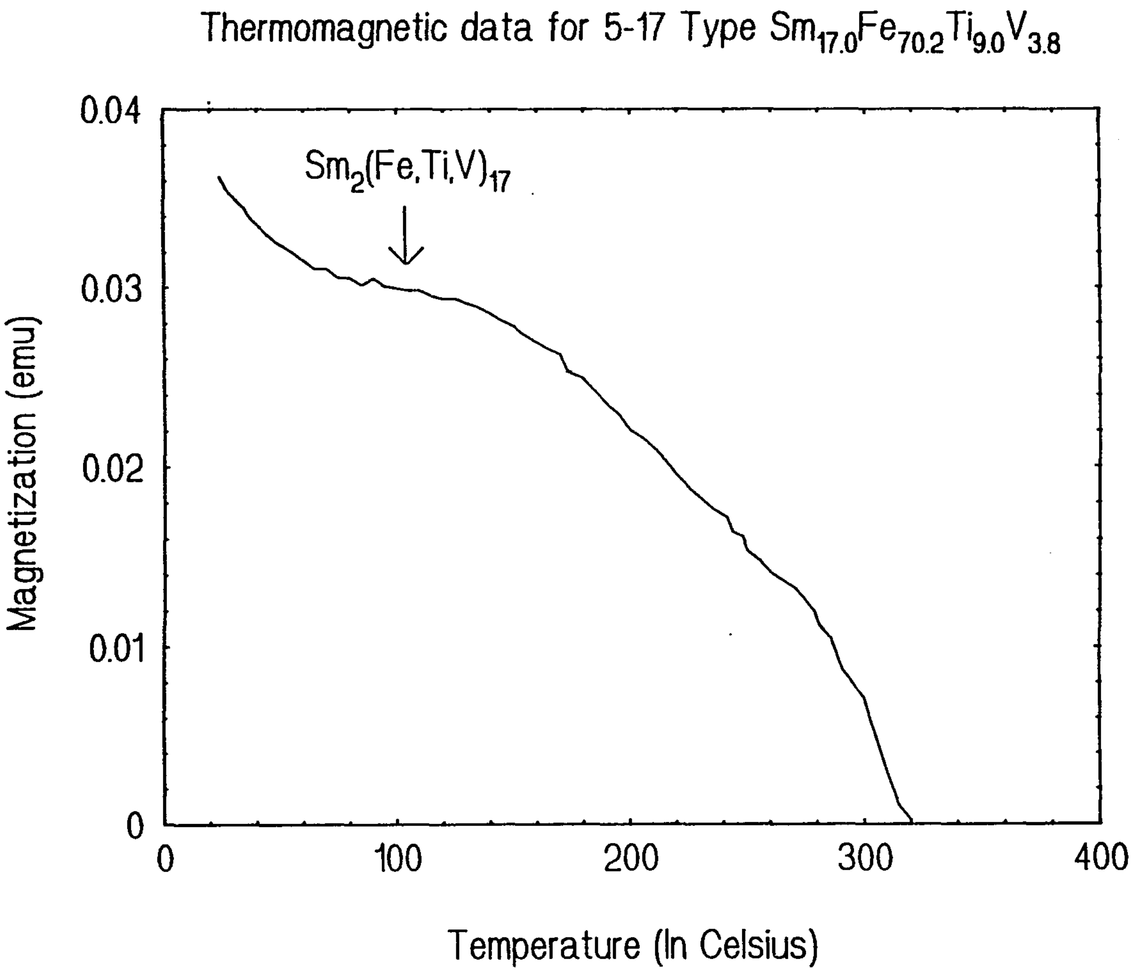

Thermomagnetic data for 5-17 Type $Sm_{17.0}Fe_{70.2}Ti_{9.0}V_{3.8}$

Figure 8.9

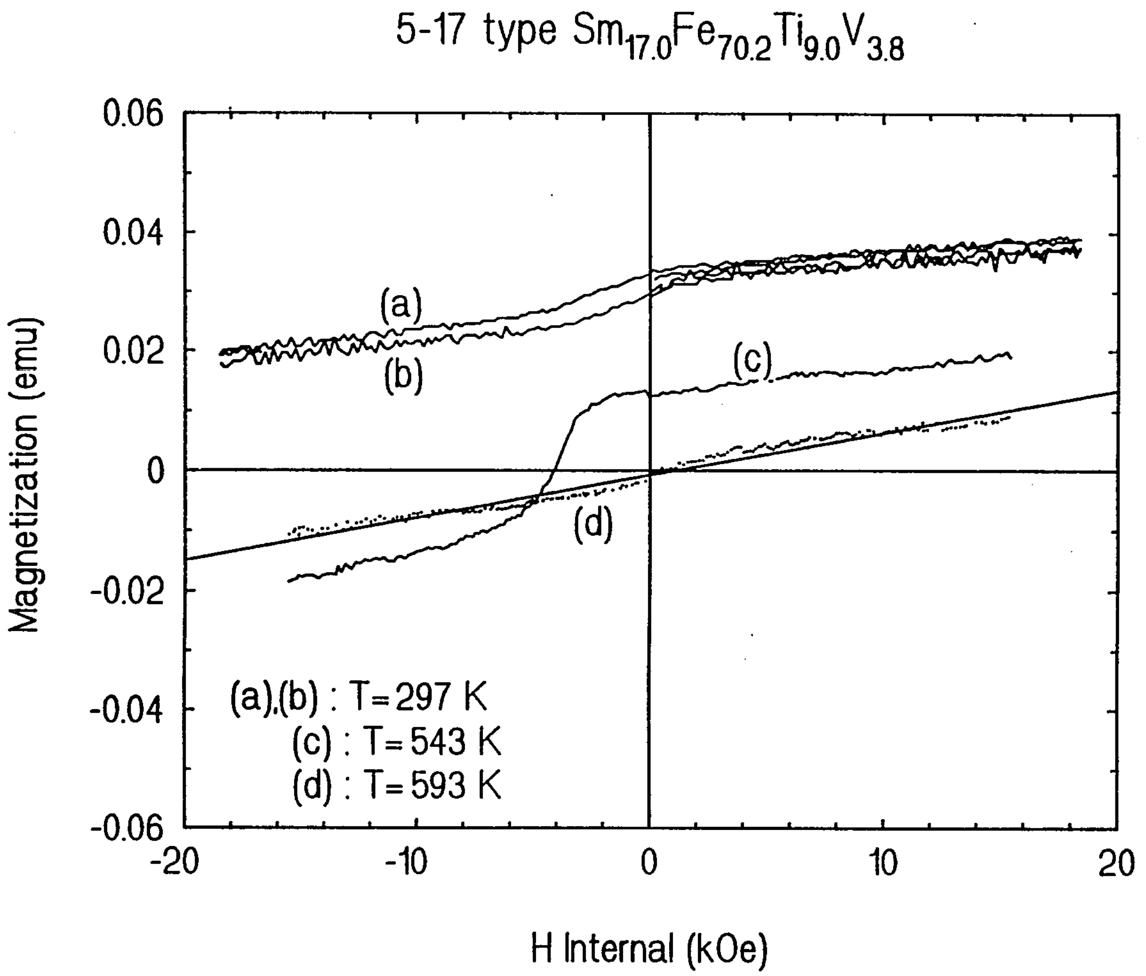
5-17 type $Sm_{17.0}Fe_{70.2}Ti_{9.0}V_{3.8}$
Magnetization (emu)
0.06
0.04
0.02
0
-0.02
-0.04
-0.06
-20
-10
0
10
20
H Internal (kOe)
(a)
(b)
(c)
(d)
(a),(b) : T=297 K
(c) : T=543 K
(d) : T=593 K

Figure 8.10

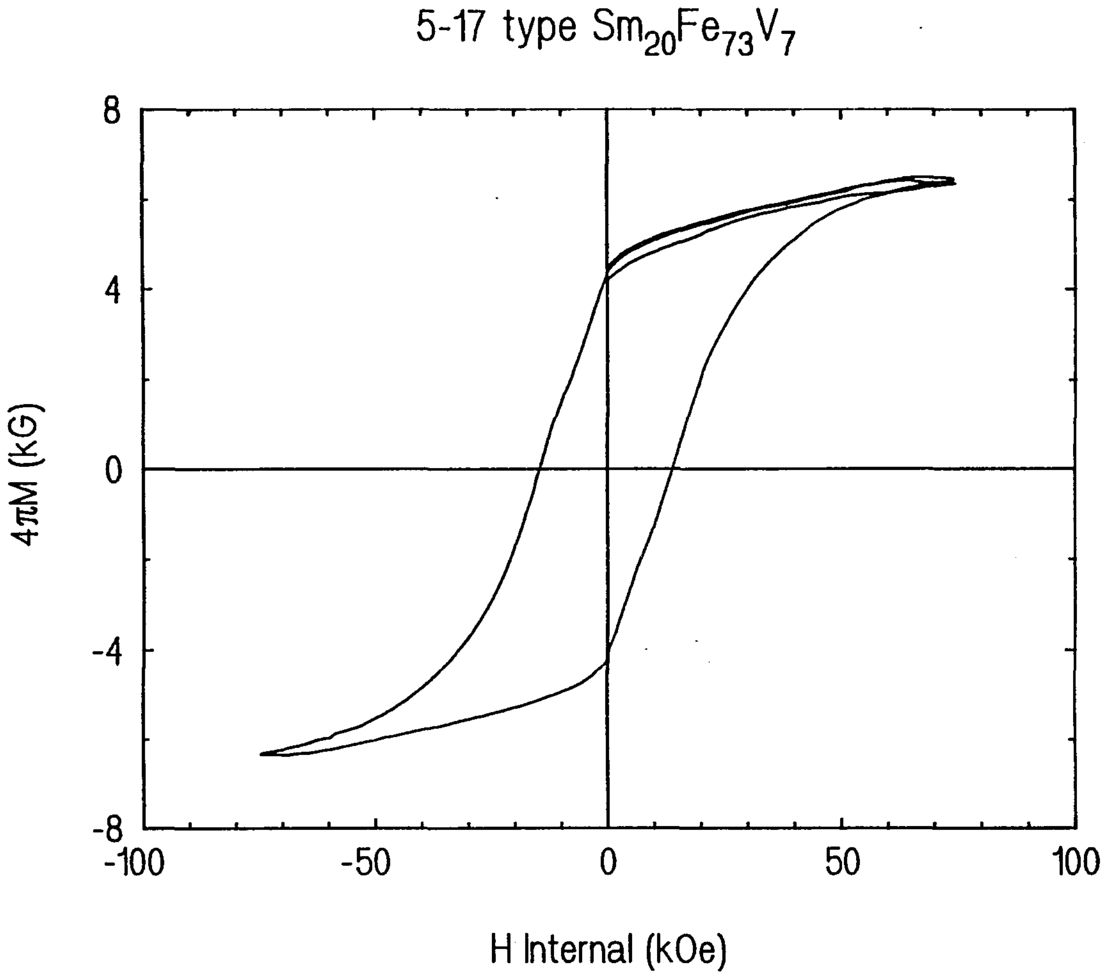
5-17 type $Sm_{20}Fe_{73}V_7$
8
4
0
-4
-8
4πM (kG)
-100
-50
0
50
100
H Internal (kOe)

Figure 8.11

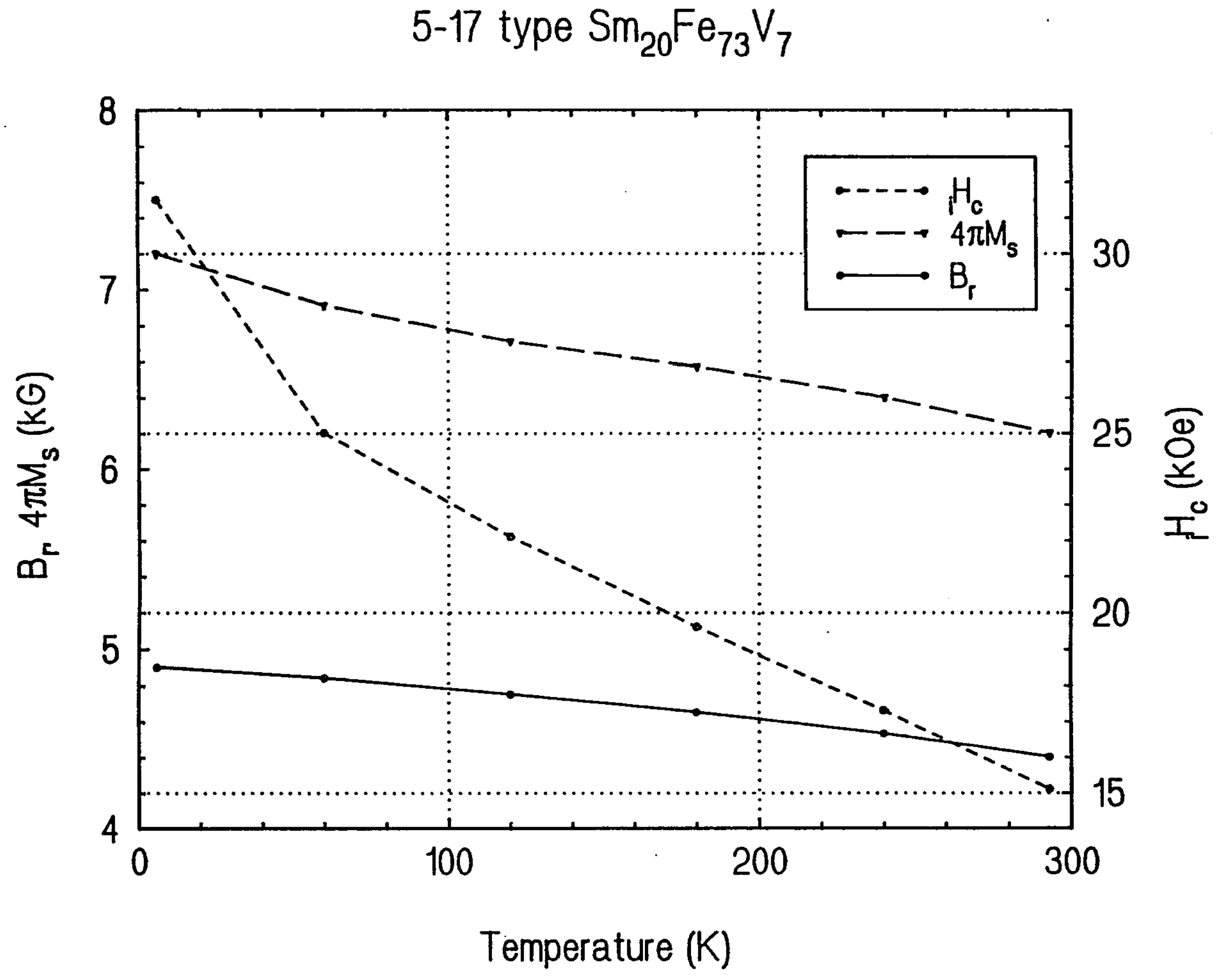

5-17 type $Sm_{20}Fe_{73}V_7$

Figure 8.12

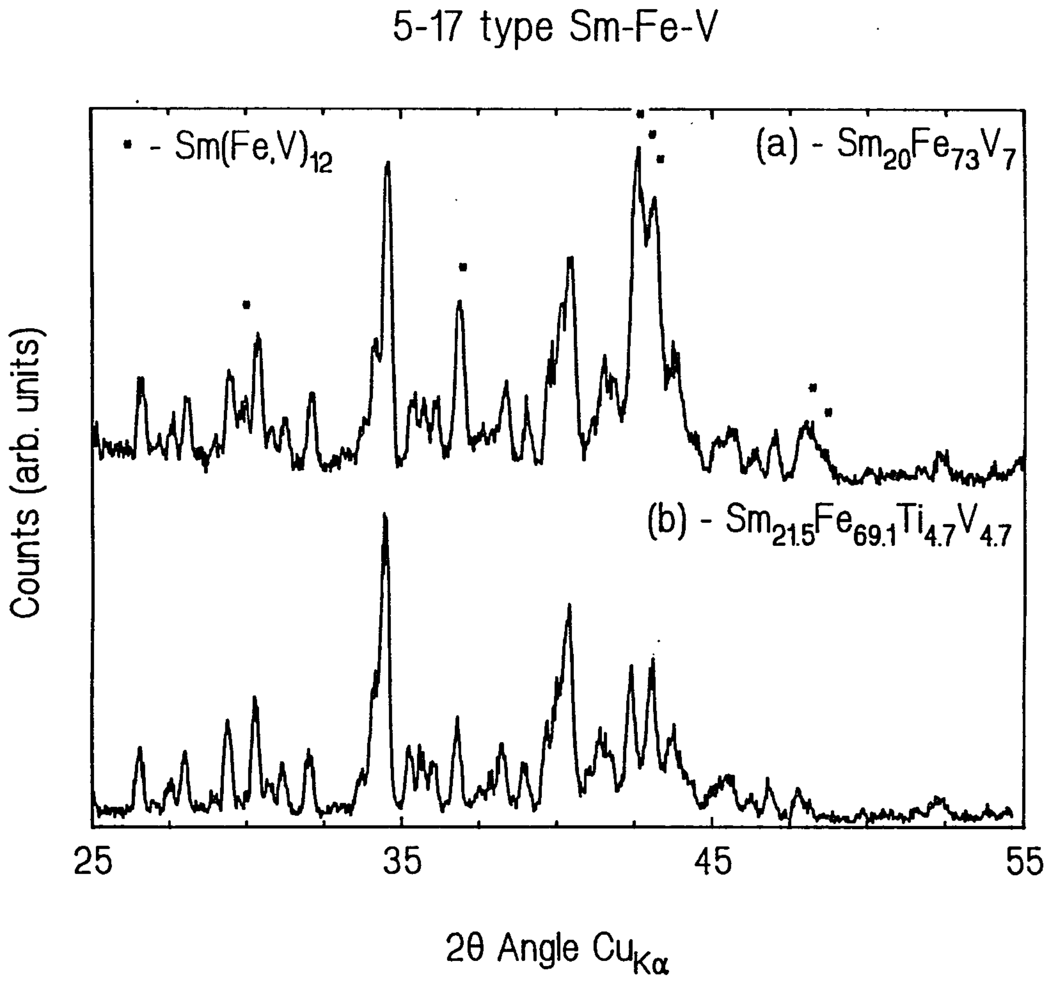
5-17 type Sm-Fe-V
▪ - Sm(Fe,V)$_{12}$
(a) - $Sm_{20}Fe_{73}V_7$
(b) - $Sm_{21.5}Fe_{69.1}Ti_{4.7}V_{4.7}$
Counts (arb. units)
25
35
45
55
2θ Angle $Cu_{K\alpha}$

Figure 8.13

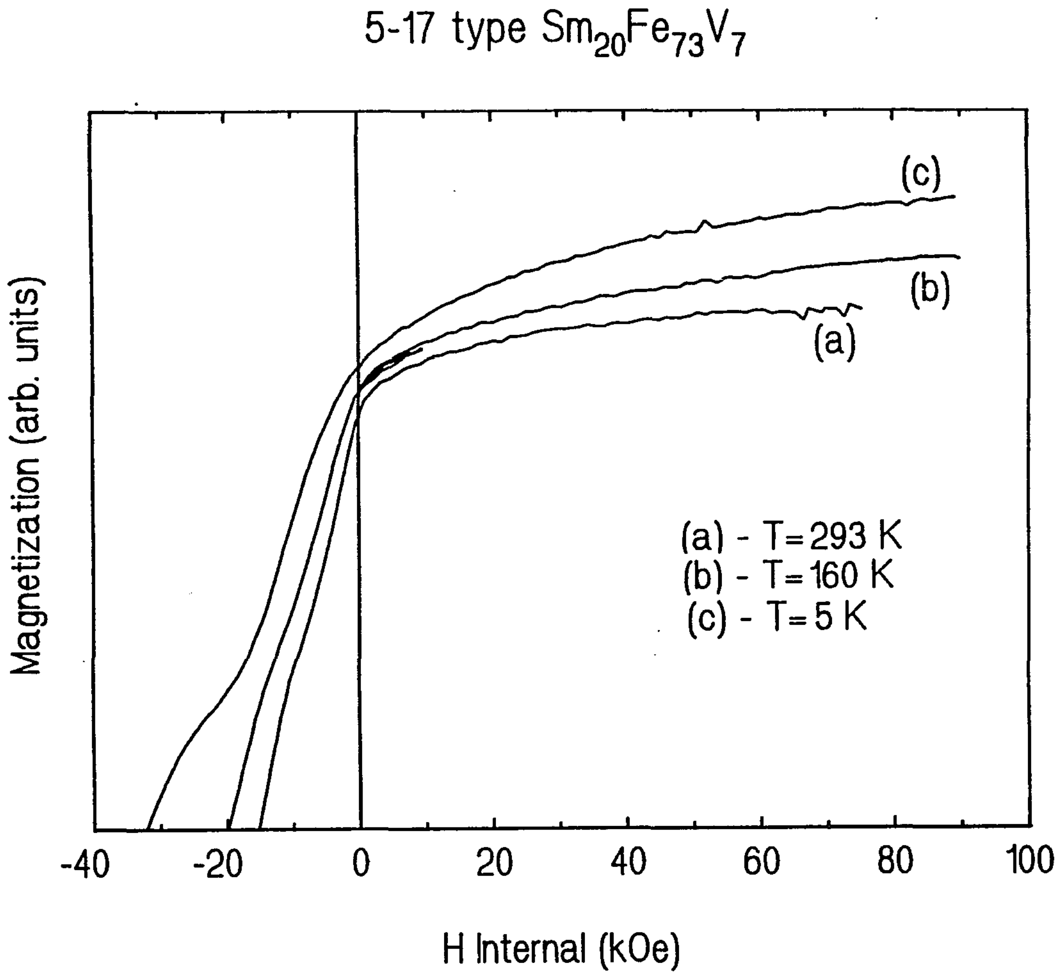
5-17 type $Sm_{20}Fe_{73}V_7$
Magnetization (arb. units)
H Internal (kOe)
-40
-20
0
20
40
60
80
100
(a)
(b)
(c)
(a) - T=293 K
(b) - T=160 K
(c) - T=5 K

Figure 8.14

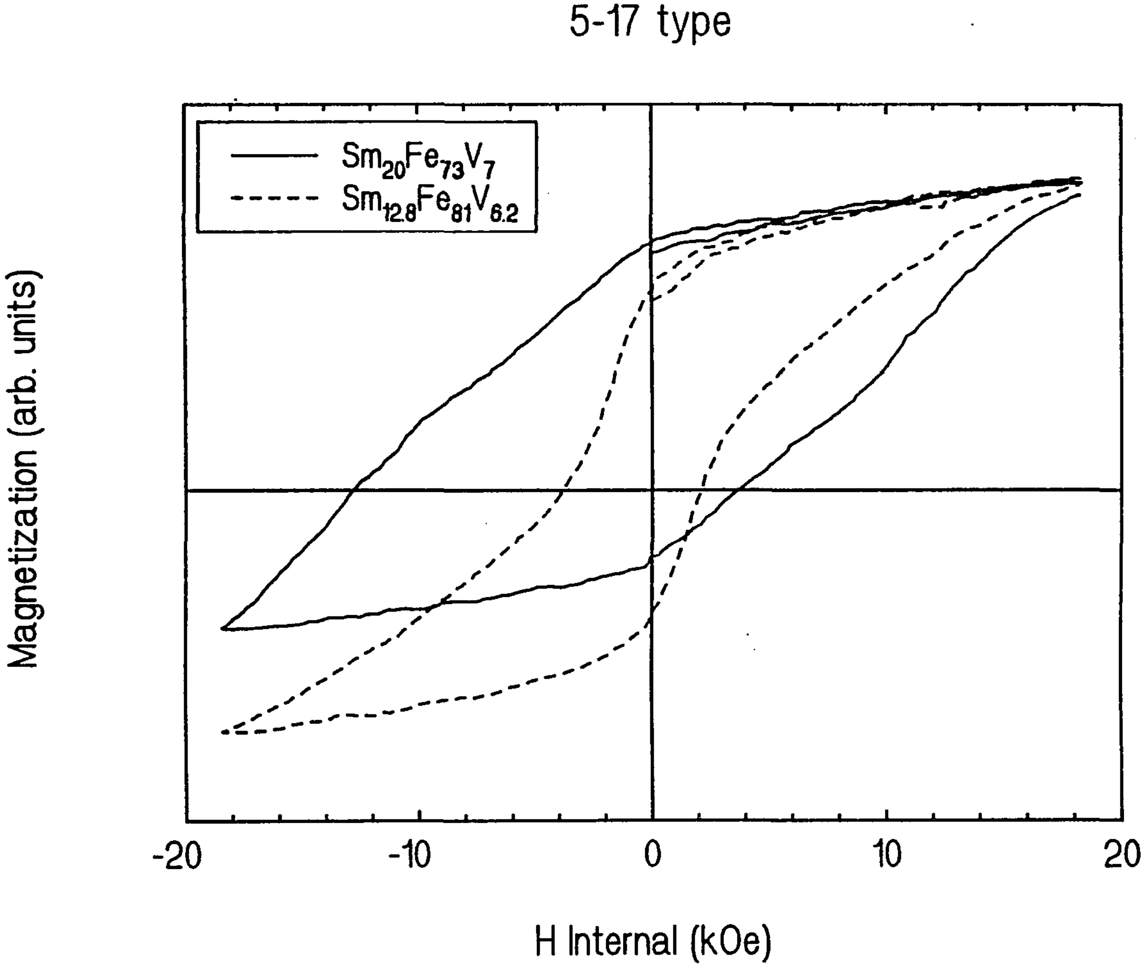
5-17 type
$Sm_{20}Fe_{73}V_7$
$Sm_{12.8}Fe_{81}V_{6.2}$
Magnetization (arb. units)
-20
-10
0
10
20
H Internal (kOe)

Figure 8.15

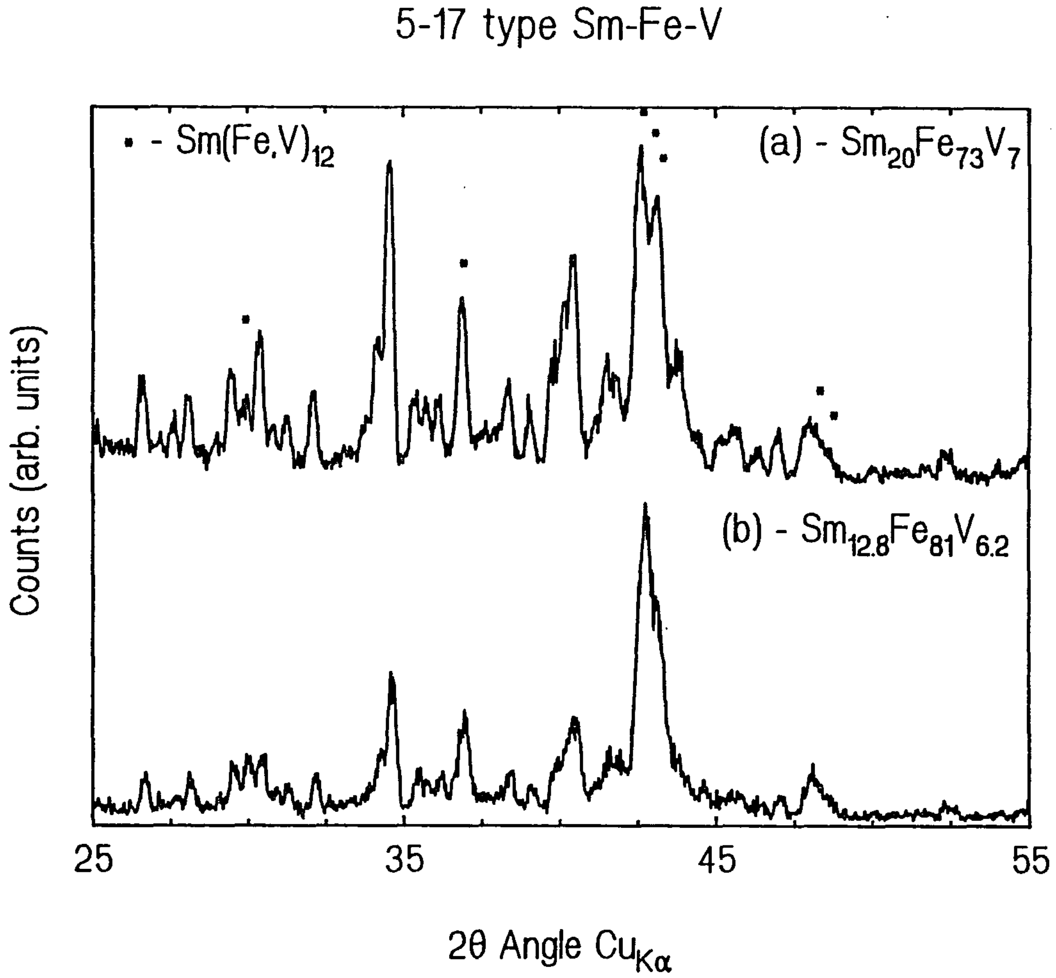
5-17 type Sm-Fe-V
▪ - Sm(Fe,V)12
(a) - Sm20Fe73V7
(b) - Sm12.8Fe81V6.2
Counts (arb. units)
25
35
45
55
2θ Angle CuKα

Figure 8.16

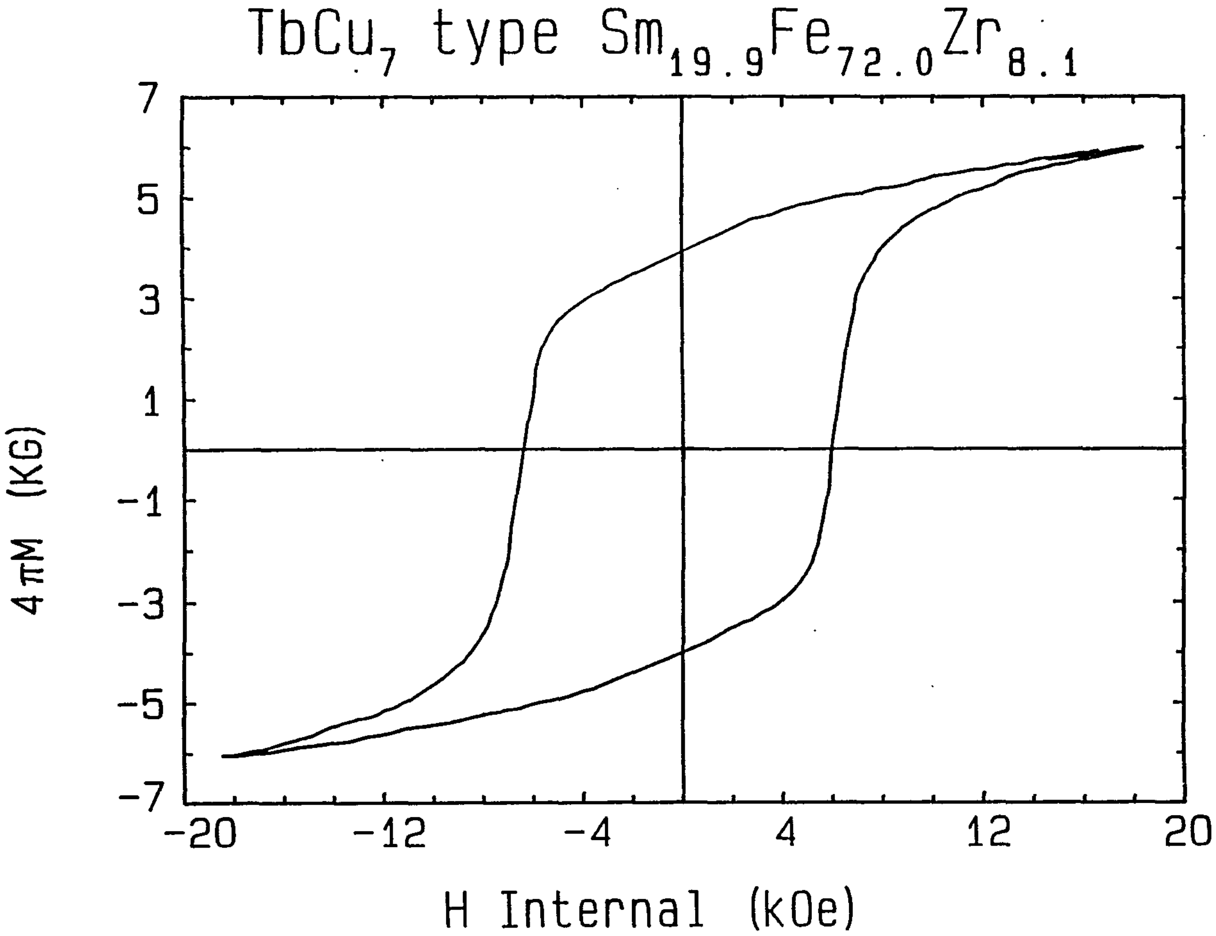
$TbCu_7$ type $Sm_{19.9}Fe_{72.0}Zr_{8.1}$
4πM (KG)
7
5
3
1
-1
-3
-5
-7
-20
-12
-4
4
12
20
H Internal (kOe)

Figure 8.17

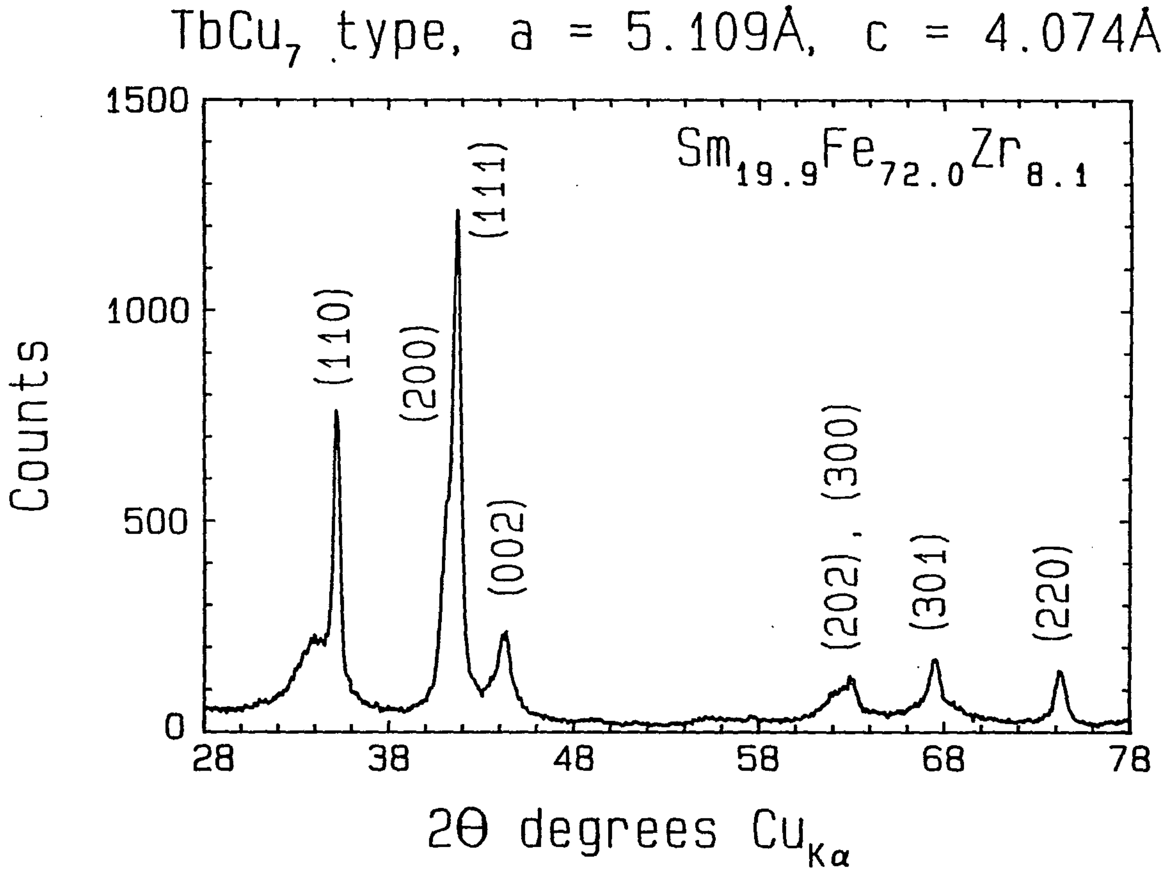
TbCu$_7$ type, a = 5.109Å, c = 4.074Å

Figure 8.18

REFERENCES

1. F.J. Cadieu, Thin Film Physics(Academic press Inc, San Diego, 1992), Vol. 16.

2. K. E. Johnson, J. Appl. Phys. 63, R13(1988).

3. F.J. Cadieu, H. Hegde, E. Schloemann, and H. J. Van Hook, J. Appl. Phys. 76, 6059(1994).

4. F.J. Cadieu, T. D. Cheung, L. Wickramasekara, and S. H. Aly, J. Appl. Phys. 55, 2611(1984).

5. K.H.J. Buschow, J. Appl. Phys. 63, 3130(1988).

6. J.M.D. Coey, J. Magn. Magn. Mat. 80, 9(1989).

7. F.J. Cadieu, H. Hegde, A. Navarathna, R. Rani, and K. Chen, Appl. Phys. Letters 59, 875(1991).

8. A. Navarathna, H. Hegde, R. Rani, S. U. Jen, and F. J. Cadieu, IEEE Trans. on Magnetics 28, 2838(1992).

9. F.J. Cadieu, A. Navarathna, R. Rani, H. Hegde, N.A. Bojarczuk and R.J. Gambino, J. Appl. Phys. 73, 6124(1993).

10 J.M.D. Coey and Hong Sun, J. Mag. Magn. Mat. 87, L251(1990).

11. Ying-chang Yang, Xiao-dong Zhang, Lin-shu Kong, Qi Pan and Sen-lin Ge, Solid State Commun. 78, 317(1991).

12. A. Navarathna, H.Hegde, R. Rani, and F. J. Cadieu, J. Appl. Phys. 73, 6242(1993)

13. Wei Gong and G.C. Hadjipanayis, IEEE Trans. on Magnetics 28, 2563(1992).

14. A. Navarathna, H. Hegde, R. Rani, K. Chen, and F. J. Cadieu, IEEE Trans. on Magnetics 29, 2812(1993).

15. A. Navarathna, H. Hegde, R. Rani, K. Chen, and F.J. Cadieu, J Appl. Phys. 75, 6009(1994).

16. T.D. Cheung, L. Wickramasekara, and F.J. Cadieu, J. Magn. Magn. Materials 54-57, 1641(1986).

17. N. Kamprath, N.C. Liu, H. Hegde, and F.J. Cadieu, J. Appl. Phys. 64, 5720(1988).

18. N. Kamprath, X.R. Quian, H. Hegde, and F.J. Cadieu, J. Appl. Phys. 67, 4948(1990).

19. H.H. Stadelmaier, G. Schneider, E-Th. Henig and M. Ellner, Mat. Lett. 10, 303(1991).

20. F. J. Cadieu, N. Kamprath, H. Hegde, A. Navarathna, and R. Rani, pp. 463-476, Sixth International Symposium on Magnetic Anisotropy and Coercivity in Rare Earth-Transition Metal Alloys, ed. S. G. Sankar, Carnegie Mellon University Press, Pittsburgh, Pennsylvania, 25 Oct., 1990.

21. F. J. Cadieu, N. Kamprath, H. Hegde, K. Chen, A. Navarathna, and R. Rani., J. Appl. Phys. 69, 5608(1991).

22. R. Rani, H. Hegde, A. Navarathna, K. Chen, and F. J. Cadieu, IEEE Trans. on Magnetics 28, 2835(1992).

23. F. J. Cadieu, H. Hegde, R. Rani, A. Navarathna, and K. Chen, Mat. Letters, 11(number 8,9), 284(1991).

24. B.D. cullity, Introduction to Magnetic Materials (Addison Wesley, New York, 1972).

25. I.A. Campbell, J. Phys. F, Metal Physics 2, L47(1972).

26. J. Alameda, D. Givord, R. Lemaire and Q. Lu, J. Appl. Phys. 52, 2079(1981).

27. B. Chapman,"Glow Discharge Processes."John Wiley and Sons, Inc., Wiley-Interscience, 1980.

28. J.L. Vossen and W Kern, eds., "Thin Film Processes." Academic Press, New York, 1978.

29. H.H. Stadelmaier, F.J. Cadieu, and N.C. Liu, Matl. Letters 6, 80(1987).

30. M. Okada, A. Kojima, K. Yamagishi, and M. Homa, IEEE Trans on Magnetics 26, 1376(1990).

31. F.E. Pinkerton and D.J. Van Wingerden, IEEE Trans. on Magnetics 25, 3306(1989).

32. J. Strzeszewski, Y.Z. Yang, E.W. Singleton, and G.C. Hadjipanayis, IEEE Trans. on Magnetics 25, 3309(1989).

33. L. Shultz, K. Schnitzke, and J. Wecker, Appl. Phys. Letters 56, 868(1990).

34. F.J. Cadieu, H. Hegde, and K. Chen, J. Appl. Phys. 67, 4969(1990).

35. H. Hegde, K. Chen, and F.J. Cadieu, J. Appl. Phys. 69, 5850(1991).

36. L. Pareti, F Bolzoni, and O. Moze, Phys. Rev. B, 32, 7604(1985).

37. G. Asti, F. Bolzoni, F Leccabue, R. Panizzieri, L. Pareti, and S. Rinaldi, J Magn. Magn. Mater., 15-18, 561(1980).

38. A van der Drift, Phillips Res. Repts. 22, 267(1967).

39. John A. Thornton, J Vac. Sci. Technol 11, 666(1974).

40. K.L. Chopra, Thin Film Phenomena(McGraw-Hill, New York, 1969), p. 220.

41. Richard J. Gambino, MRS Bulletin/April 1990, page 20.

42. N.C. Koon, M. Abe, E. Callen, B.N. Das, S.H. Liou, A. Martinez, and R. Segnan, J Magn. Magn. Mater. 54-57, 593(1986).

43. R.W. Grant,"Mössbauer Spectroscopy in Magnetism: Characterization of Magnetically-Ordered Compounds", Chap. 3 of Mössbauer Spectroscopy Edited by U. Gonser, Springer-Verlag New York Heidelberg Berlin, 1975.

44. K.H.J. Buschow, Ferromagnetic materials, edited by E.P. Wohlfarth and K.H.J. Buschow (North-Holland, New York, 1988), Vol. 4.

45. G.S. Krinchik and V.A. Artem'ev, Sov. Phys. JETP 26, 1080(1968).

46. D. Elbaz, D. Givord, S. Hirosawa, F.P. Missell, M.F. Rossignol, and V. Villas-Boas, J. Appl. Phys. 69, 5492(1991).

47. Ying-Chang Yang, Hong Sun, Lin-Shu Kong, Ji-Lian Yang, Yong-fan Ding, Bei-sheng Zhang, Chun-tang Ye, Lan Jin, and Hui-ming Zhou, J Appl. Phys. 64,5968(1988).

48. D. Givord and R. Lemaire, IEEE Trans. Magn. MAG-10,109(1974).

49. L.Y. Zhang, E.B. Boltich, V.K. Sinha, and W.E. Wallace, IEEE Trans. on Magnetics 25, 3303(1989).

50. R. Rani, H. Hegde, A. Navarathna, and F.J. Cadieu, J. Appl. Phys. 75, 6006(1994).

51. R. Skomski, M.D. Kuz'min, and J.M.D. Coey, J. Appl. Phys. 73, 6934(1993).

52. M. Sagawa, S. Fujimura, N. Togawa, H. Yamamoto, and Y. Matsuura, J. Appl. Phys. 55, 2083(1984).

53. Y. Otani, D.P.F. Hurley, Hong Sun, and J.M.D. Coey, J. Appl. Phys. 69, 5584(1991).

54. K. Schnitzke, L Schultz, J Wecker, and M. Katter, Appl Phys. Lett. 56, 587(1990)

55. A. Hütten and G. Thomas, pp. 110-126, Proceedings of 11th intl. Symposium on Anisotropy and Coercivity in Rare Earth-Transition metal alloys, ed. S.G. Sankar, Carnegie Mellon Univ. Press, Pittsburgh, Oct. 1990.